SUPERCONDUCTING QUANTUM INTERFERENCE DEVICES FOR THE DETECTION OF MAGNETIC FLUX AND APPLICATION TO AIRBORNE HIGH FREQUENCY DIRECTION FINDING

THESIS

Travis Abeita, Captain, USAF

AFIT-ENG-MS-15-M-052

DEPARTMENT OF THE AIR FORCE
AIR UNIVERSITY

AIR FORCE INSTITUTE OF TECHNOLOGY

Wright-Patterson Air Force Base, Ohio

The views expressed in this thesis are those of the author and do not reflect the official policy or position of the United States Air Force, the Department of Defense, or the United States Government.

AFIT-ENG-MS-15-M-052

SUPERCONDUCTING QUANTUM INTERFERENCE DEVICES FOR THE DETECTION OF MAGNETIC FLUX AND APPLICATION TO AIRBORNE HIGH FREQUENCY DIRECTION FINDING

THESIS

Presented to the Faculty

Department of Electrical and Computer Engineering

Graduate School of Engineering and Management

Air Force Institute of Technology

Air University

Air Education and Training Command

in Partial Fulfillment of the Requirements for the

Degree of Master of Science in Electrical Engineering

Travis Abeita, B.S.E.E.

Captain, USAF

March 2015

AFIT-ENG-MS-15-M-052

SUPERCONDUCTING QUANTUM INTERFERENCE DEVICES FOR THE DETECTION OF MAGNETIC FLUX AND APPLICATION TO AIRBORNE HIGH FREQUENCY DIRECTION FINDING

THESIS

Travis Abeita, B.S.E.E.
Captain, USAF

Committee Membership:

Lt Col Jeremy Stringer, PhD
Chair

Maj Michael Seal, PhD
Member

Maj Derrick Langley, PhD
Member

AFIT-ENG-MS-15-M-052

Abstract

Electrically small antennas trade reception performance for physical size reduction. The SQUID maximizes the reception performance; still achieving a physically small size leading to satisfying the demanding antenna requirements of an airborne high frequency direction finding antenna system. High frequency electromagnetic reception for a direct current (DC) superconducting quantum interference device (SQUID) is simulated using the resistor-capacitor-shunted-junction (RCSJ) electronic circuit model, producing a set of two-dimensional ordinary differential equations to describe the electrical operating characteristics for the DC SQUID. A time-varying magnetic flux, consisting of frequencies from the HF band, is applied to characterize the voltage response of the DC SQUID. An instantaneous voltage develops across the DC SQUID, although a fast time-average must be computed to produce usable voltage samples. These voltage samples are shown to be representative samples of the applied time-varying signal containing a voltage bias. The waveform produced from these voltage samples is periodic, while preserving the phase of the incident signal. The HF reception characteristics of a single DC SQUID is shown, including an examination for expanding the loop area, simulating a DC SQUID array. Additionally, the DC SQUID is compared to the MGL-S8A BDOT sensor using by optical responsitivity.

Acknowledgments

I would like to thank my research advisor, Lt Col Jeremy Stringer, for keeping me on track and focused throughout the research process. I appreciate all of the help and guidance that you provided during the research process and the technical writing phase. Your guidance was invaluable for the completion of this research, and I hope that I have meet and exceeded your expectations. I will benefit from the wisdom I have acquired for years to come.

I would like to thank my committee members, Maj Michael Seal and Maj Derrick Langley, for your help with this research. Our technical discussions helped improve this research effort and help me to better understand the research process. Additionally, I would like to thank my research sponsors Dr. Charles Cerny and Mr. Leroy Willemsen of Air Force Research Laboratory (AFRL) Radio Frequency Systems Branch (RYMR) for providing research funding and placing me in contact with SQUID research groups.

Lastly, I would like to thank my beautiful wife and our loving children. You always provided the support I needed for working through the long nights and weekends; always giving me the extra motivation to keep going. Without you, I would not have been able to finish in one piece because you were always there to relieve the stress, provide relief, and keep me going. Thank you.

Travis Abeita

Table of Contents

Page

Page

List of Figures

List of Tables

List of Acronyms

Acronym	Definition
AOA	angle of arrival
AFRL	Air Force Research Laboratory
AFIT	Air Force Institute of Technology
AWGN	additive white Gaussian noise
BCS	Bardeen-Cooper-Schreiffer
DC	direct current
DF	direction finding
DFT	discrete Fourier Transform
DOA	direction of arrival
EM	electromagnetic
ESA	electrically small antenna
GPS	Global Positioning System
HF	high frequency
ISR	Intelligence, Surveillance, and Reconnaissance
I-V	current-voltage
IVP	initial value problem
L-C	inductor-capacitor
MATLAB	Matrix Laboratory
MHz	megahertz
MRI	magnetic resonance imaging
NDE	non-destructive examination
ODE	ordinary differential equation
PDE	partial differential equation

Acronym	Definition
PEC	perfect electric conductor
RCSJ	Resistor Capacitor Shunted Junction
RKF	Runge-Kutta-Fehlberg
RF	radio frequency
RYMR	Radio Frequency Systems Branch
SI	structurally integrated
SNR	signal to noise ratio
SQUID	superconducting quantum interference device
SQUIF	superconducting quantum interference filter
UAV	unmanned aerial vehicle
U.S.	United States
YBCO	yttrium barium copper oxide

SUPERCONDUCTING QUANTUM INTERFERENCE DEVICES FOR THE DETECTION OF MAGNETIC FLUX AND APPLICATION TO AIRBORNE HIGH FREQUENCY DIRECTION FINDING

I. Problem Statement

AIRBORNE direction finding (DF) in the high frequency (HF) band of the electromagnetic (EM) spectrum provides potential for practical military applications. Examples of military application include using an airborne HF DF system for electronic Intelligence, Surveillance, and Reconnaissance (ISR) and airborne navigation. Airborne HF DF will expand military counterinsurgency operations into the HF band of the EM spectrum, allowing for the radio-localization of enemy HF communication systems. Airborne HF DF will also provide a capability enhancement for airborne navigation by providing the ability to navigate using known HF emitter locations, such as the Standard Time and Frequency signals broadcast throughout the globe.

An airborne HF DF system has several theoretical problems arising from the use of a spatially limited platform to host a DF antenna system, and with the use of electrically small antenna (ESA)s for the reception of HF signals. Conventional DF is performed using an antenna array spanning multiple wavelengths of the operating frequency to produce a detectable phase difference at each individual antenna element. HF wavelengths spatially extend from 10 to 100 meters and the host airframe measures 41 meters in length with a wingspan of 39 meters [1]. At the low frequency portion of the HF band, the airframe limits the physical size of the antenna array to be less than half of a wavelength, causing degraded DF performance. This problem is further complicated with the use of ESAs to receive HF signals. ESAs trade reception performance for the reduction of physical size [22]. The poor

radiation efficiency of ESAs require additional amplifiers to achieve the minimum signal to noise ratio (SNR) required for DF. The aforementioned theoretical issues have been the focus of several research efforts.

AFRL contracted the Berrie-Hill Corporation to evaluate the feasibility of conducting DF operations on-board a RC-135 airframe [42], shown in Figure 1.1. The Berrie-Hill corporation used the "Theory of Characteristic Modes for Conducting Bodies" developed by Roger Harrington to determine the optimum antenna locations for this airframe [42]. The Theory of Characteristic Modes states that the radiation properties of an electrically small conducting surface can be characterized using only a few modes [24]. The radiation properties of the airframe were found using this theory and the optimum antenna locations for HF EM reception were found by numerical computation. The Berrie-Hill research continued with a DF performance analysis for the computed antenna locations. Their results show that DF is possible with the RC-135 airframe using structurally integrated (SI) antennas.

Airborne HF DF research continued at the Air Force Institute of Technology (AFIT) with Captain Clair Corbin [18]. Captain Corbin evaluated alternative direction of arrival (DOA) estimation techniques to improve azimuthal resolution and found azimuthal resolution of $< 1^o$ with a SNR of 10 dB [18]. The size of the Berrie-Hill SI antenna design was not compatible with flight, so Captain Ryan Hardin and Captain Michael Archer investigated using small MGL-S8A magnetic field sensors for HF EM detection [9, 23]. Their research found that the sensitivity of the MGL-S8A sensors did not exceed or match the reception characteristics of the Berrie-Hill SI antenna design. The recent advancements in the field of superconductivity have enabled the possibility of a superconducting ESA. This thesis examines the detection of HF EM energy using an ESA based on superconductors and quantum mechanical principles for application to airborne HF DF.

Figure 1.1: RC-135 airframe considered for an airborne high frequency direction finding antenna system. [1]

1.1 Introduction

The HF spectrum offers improved long-range communication performance due to the propagation characteristics of HF EM waves. The HF range is internationally and domestically defined to encompass the range 3-30 megahertz (MHz) [2–4, 6]. The uses of the HF spectrum include [5, 6, 20],

- Voice and/or data communication with remote locations
- Voice and/or data communication with ground, maritime, and aeronautical platforms
- International distress
- International broadcast and communication
- International time and frequency signal emissions

An airborne DF system operating within the HF spectrum provides numerous military applications. An airborne HF DF system will provide an alternate means of aeronautical

navigation using known HF source emitters, such as the Standard Time and Frequency emissions or international broadcasting stations. This system contains potential to reduce the United States (U.S.) military reliance on Global Positioning System (GPS) based navigation systems by providing an alternate aeronautical navigation capability. In addition to navigation, the airborne HF DF system provides a mobile airborne ISR capability to intercept and analyze HF communications and waveforms at a considerable standoff distance.

1.2 Research Goals

The goal of this research effort is to determine the feasibility of HF EM reception using a superconducting ESA for application to an airborne DF system. Previously, Captain David Archer evaluated the MGL-S8A B-DOT magnetic field sensor for airborne HF DF [9]. Captain Archer concluded the MGL-S8A did not possess the required sensitivity for airborne HF DF in a comparison with the Berrie-Hill SI antennas [9], and proposed the use of superconducting quantum interference device (SQUID) technology as a viable alternative for the detection of HF EM enegy. This research begins with an examination of the current state of superconducting technology and research. A device capable for the detection of HF EM energy is selected and modeled. The model is verified with an examination of computer simulations and with a comparison to completed research within the superconducting field. AFIT does not possess SQUID sensors for laboratory superconducting research, thus results will be limited to computer generated solutions. The goals of this research are outlined below,

- Examine superconducting technology to determine the state of superconducting research
- Identify applicable superconducting technology and implement models for HF sensor characterization

- Simulate HF reception using the superconducting sensor model
- Examine the HF reception characteristics to determine EM sensitivity

1.2.1 Scope.

The scope of this research will be limited to numerical evaluation. The HF superconducting sensor design is characterized using the electrical operating characteristics, the produced waveform, and the expected sensitivity achieved with superconducting technology. This research is completed using mathematical models and computer simulations. A hardware evaluation of SQUID technology is not performed. The atmospheric propagation characteristics in the HF environment, such as sky-waves and ionosphere skip are not considered. The environmental design considerations for an airborne environment are not considered.

1.2.2 Assumptions.

The general assumptions made during the completion of this research effort include:

- Electromagnetic propagation is in free, unbounded space
- Sensors are illuminated by plane waves in the farfield region
- Thermal noise is modeled as additive white Gaussian noise (AWGN)
- Physical device construction is perfectly symmetric to exclude asymmetrical effects impacting SQUID performance

1.3 Resource Requirements

The resources required to successfully complete this research effort include:

- Matrix Laboratory (MATLAB)

1.4 Document Overview

This thesis presents the reception of HF EM energy using superconducting technology and the application to airborne HF DF. Chapter 2 presents the theoretical foundation of superconductivity and applicable superconducting technology for airborne HF DF. Chapter 3 presents the methodology for evaluating a superconducting based antenna element design. Chapter 4 presents the results of numerical simulations and experiments. Chapter 5 presents the conclusions and future work for the continuation of this research project.

II. Background

CHAPTER II provides an introduction to superconducting theory, superconducting magnetic flux sensing, and the application of superconducting quantum interference technology to airborne HF EM detection.

2.1 Previous Research

Airborne HF DF research began at AFIT with the evaluation of DF capability on board the unmanned aerial vehicle (UAV) by Dixon and Akers [7, 19]. A research effort was also performed by AFRL using a large airborne platform. AFRL contracted the Berrie-Hill Research Corporation to determine airborne DF feasibility using the RC-135 [42]. The research performed by the Berrie-Hill Corporation found airborne HF DF is achievable with strategically placed SI antennas. Captain Michael Corbin furthered airborne HF DF research by evaluating DF algorithms for improved angle of arrival (AOA) estimation and found azimuthal resolution of less than 1 degree is achievable with a minimum SNR level of 10 dB. Next, Captain Ryan Hardin evaluated the performance of two BDOT magnetic field sensors, and down-selected the best sensor for the HF band. Captain Michael Archer continued Captain Hardin's research with the down-selected BDOT magnetic sensor to conduct HF EM simulations on a generic airframe built to the RC-135 dimensions. Captain Archer concluded that the magnetic field sensor did not possess the required level of sensitivity necessary for airborne HF DF and proposed the SQUID as a candidate for airborne HF DF.

2.2 Superconductivity

The state of superconductivity was discovered by Dutch physicist Heike Onnes in 1911 [12]. Onnes discovered that the mercury sample he was experimenting with exhibited zero electrical resistance when cooled to 4 Kelvin. Onnes's discovery opened the field of

superconductivity and spurred superconducting research. Superconducting research started with the goals of:

- Finding and characterizing other superconducting materials
- Explaining the state of superconductivity

Early superconducting research focused on finding or creating new superconducting materials. It wasn't long before new superconducting materials were discovered, with each material having a unique critical temperature. The critical temperature is the temperature at which the material enters the superconducting state [12]. An effort to find higher critical temperatures soon developed with the goal of discovering a room temperature superconducting material. The room temperature superconductor will revolutionize the electronics field by allowing the development of near loss-less power distribution systems, enabling the creation of ultra low noise amplifiers, and generally enhancing the electronics field entirely.

Superconductors are classified into multiple categories that are divided by the theory of operation (Type I and Type II superconductors), by critical temperature (high and low temperature superconductors), or by the material itself. The constituent material parameters that contribute to the superconducting state still remain unknown and, as a result, the discovery of new superconducting materials has been reduced to the process of trial and error [12]. High temperature superconducting research is focused on critical temperatures above 77 K, with the primary material being $YBa_2Cu_3O_{7-x}$ or yttrium barium copper oxide (YBCO), having a critical temperature of 93 K. The primary cooling refrigerant used for high temperature superconductivity is liquid Nitrogen with a cooling temperature of 77 Kelvin. Low temperature superconducting research is focused on critical temperatures below 77 K. There are several material types that are used for this temperature range with Niobium as the most commonly used material. The primary cooling refrigerant used is liquid Helium, allowing for a cooling temperature of 4.7 K.

2.2.1 Superconducting State.

The superconducting state is characterized by zero electrical resistance and the expulsion of magnetic fields from within the material, known as the Meissner Effect. The superconducting state is entered when the material is cooled below the critical temperature, T_C. The critical temperature is different for each superconducting material. Multiple theories have been developed to explain the state of superconductivity but the only theory found to provide an adequate description is the Bardeen-Cooper-Schreiffer (BCS) theory. The BCS theory describes superconductivity as the interaction between the formation of Cooper electron pairs and the crystal lattice formed by the material's protons. The BCS theory has been shown to be valid only for low temperature superconductivity. High temperature superconductivity is not well explained by the BCS theory description. This leads to the division between Type 1 and Type II superconductors. Type I superconductivity is explained by BCS theory. Type II superconductivity is not well explained using BCS theory. The superconducting description for Type II materials is an active area of research in the field of quantum physics.

2.2.2 Quantum Mechanics.

Quantum mechanics attempts to provide a mathematical description for the physical processes in the universe. This math description starts with finding the wave function of an elementary particle $\Psi(x,t)$. The wave function describes a quantum object for all future time, given suitable initial conditions, and is found by solving the time independent Schrödinger equation [21],

$$j\bar{h}\frac{\partial\Psi}{\partial t} = -\frac{h^2}{2m}\frac{\partial^2\Psi}{\partial x^2} + V\Psi \tag{2.1}$$

with j equal to $\sqrt{-1}$, Plancks constant h, the particle mass m, and the particle location x. The wave function can be represented as a series of linearly separable wave solutions taking the form [21],

$$\Psi(x,t) = \sum_{n=1}^{\infty} c_n \Psi_n(x,t) \tag{2.2}$$

where c_n is the set of wave function constants. The wave function has a statistical interpretation with the probability for finding the quantum particle's location by taking the integral of the magnitude squared of the wave function over the given region [21].

$$P(a \leq x \leq b | t = t_0) = \int_a^b |\Psi(x,t)|^2 dx \tag{2.3}$$

A solution for the wave function takes the form [16],

$$\Psi(x,t) = |\psi(x,t)| \exp j\delta(x,t) \tag{2.4}$$

with magnitude ψ and phase δ that is a function of the particle's location at a given time.

2.2.3 Magnetic Flux Quantization.

The magnetic flux threading a superconducting ring was predicted to be quantized in the units of the magnetic flux quantum. This result arises from requirement for the macroscopic wave function being single valued inside a superconducting ring. The phase $\delta(x,t)$ has a unique solution for each x location along the superconducting ring when no current or magnetic fields are applied to the ring. When the ring is threaded by a magnetic flux, the phase around the loop will change by $2\pi n$, where n is the number of enclosed magnetic flux quanta. The magnetic flux quantum is defined as,

$$\Phi_0 = \frac{\bar{h}}{2\mathrm{e}} \tag{2.5}$$

Where Planck's constant is $\bar{h} = 6.66x10^{-34} Joule - second$ and e is the electron charge. The value of the flux quantum is $\Phi_0 = 2.07x10^{-15}$ Wb.

2.2.4 The Josephson Effect.

The Josephson Effect is the tunneling of supercurrent through a barrier that physically separates two superconducting electrodes. The voltage potential across the junction remains at zero until the supercurrent exceeds a current threshold, termed the critical current, I_C. The Josephson Effect is observed in a junction constructed by placing a barrier in-between two superconducting electrodes. The barrier can be constructed as

a thin insulating layer, a narrow constriction of the conductor path, or with a thin layer of different superconducting materials. This junction is named after Brian D. Josephson, whom in 1962 mathematically predicted the occurrence of tunneling supercurrent through the superconducting junction design [26]. The junction design describes a capacitor in normal electromagnetic theory with conventional materials. A physical depiction of the Josephson junction is shown in Figure 2.1. The defining parameters of the junction are the

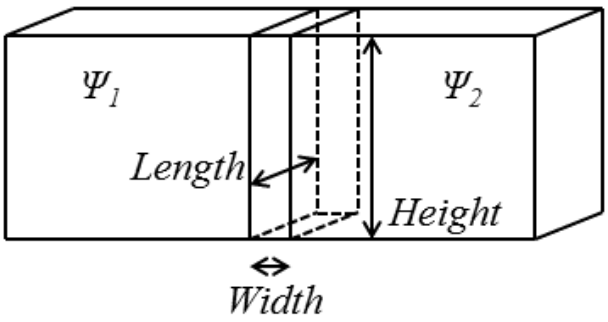

Figure 2.1: Physical depiction of a Josephson junction

length, width, and height of the barrier, and the superconducting and barrier materials used for construction. The super current, I_S, flowing through the Josephson junction is given by [25],

$$I_S = I_C sin\delta \tag{2.6}$$

where I_C is the critical current and δ is the phase difference between the macroscopic superconducting wave functions at each superconducting electrode, $\delta = \Psi_1 - \Psi_2$. The critical current, I_C, is a function of junction materials and physical dimensions. Josephson postulated that a voltage develops across the junction when a time-varying phase difference is present. The voltage and phase relationship is given by,

$$\dot{\delta} \equiv \frac{\partial \delta}{\partial t} = \frac{2eU}{\bar{h}} = \frac{2\pi U}{\Phi_0} \tag{2.7}$$

where δ is the phase difference between the wave functions Ψ_1 and Ψ_2, $\dot{\delta}$ is the time derivative of δ, U is the instantaneous voltage across the junction, e is the charge of one electron e $= 1.602x10^{-19}$ Coulombs, Plank's constant $\bar{h} = 6.66x10^{-34} Joule - second$, and the magnetic flux quantum $\Phi_0 = 2.0678x10^{-15}$ Webers. Equations 2.6 and 2.7 mathematically define the operating characteristics of the junction, and are commonly known as the Josephson relations.

The supercurrent flowing through the junction is described as the tunneling of Cooper electron pairs traveling through the barrier. The current flow is termed supercurrent to distinguish this type of current flow from the conventional depiction of current flow. The Josephson effect was experimentally observed by P. Anderson and J. Rowell in 1963 using a thin tin oxide barrier between the superconducting metals Tin (Sn) and Lead (Pb) [8].

2.2.5 Modeling.

The superconducting state was initially thought of as the perfect electric conductor (PEC). The PEC and the superconductor share the zero electrical resistance trait, however the PEC description was discovered to be inadequate because this description does not account for the superconductor expelling all magnetic flux from within the superconductor, known as the Meissner effect [13]. While both the PEC and the superconductor do not allow the formation of a time-varying magnetic fields within the conductor itself, the PEC will allow for a static magnetic field to exist inside the conductor. The superconductor differs because all magnetic flux is expelled from within the superconductor.

EM simulation software currently available has limited support for superconductor modeling and EM simulation of the Josephson junction is currently nonexistent. The junctions mathematical description is the only method available for simulating the electrical performance of the junction.

A circuit representation is used to mathematically model the electrical characteristic of the Josephson junction. There are three circuit representations for the Josephson junction [29].

- The Resistively-Shunted-Junction (RSJ) Model
- The Tunnel-Junction-Microscopic (TJM) Model
- The Nonlinear-Resistive (RSJN) Model

These circuit representations describe the junction using a parallel configuration of a resistor, noise current source, and a junction element. The representations differ with the implementation of the super current, I_S, flowing through the junction element. The RSJ model uses a linear I_S equation, the TJM model uses a piece-wise continuous I_S equation, and the RSJN model uses a nonlinear I_S equation. The most commonly used model is the RSJ model, however a capacitor circuit element is added to better model the junction electrical characteristics [16], and is named the Resistor Capacitor Shunted Junction (RCSJ) model. The RCSJ model is shown in Figure 2.2.

The electrical operating characteristic of the Josephson junction is described by the I-V characteristic curve, and shows the relationship between the junction current and junction time-averaged voltage. Figure 2.3 shows an example I-V curve depicting the general relationship between current and time-averaged voltage by showing that zero junction voltage develops for current values less than the critical current I_C, and non-zero voltage for when the junction critical current is exceeded. A hysteresis loop develops for under damped junctions and is described by a double valued curve in the I-V characteristic curve. One curve is produced when the current is increased and the other when the current is decreased. An example of hysteresis is shown in Figure 2.4. The amount of hysteresis is proportional to the junction resistance and is reduced by decreasing the junction capacitance, C.

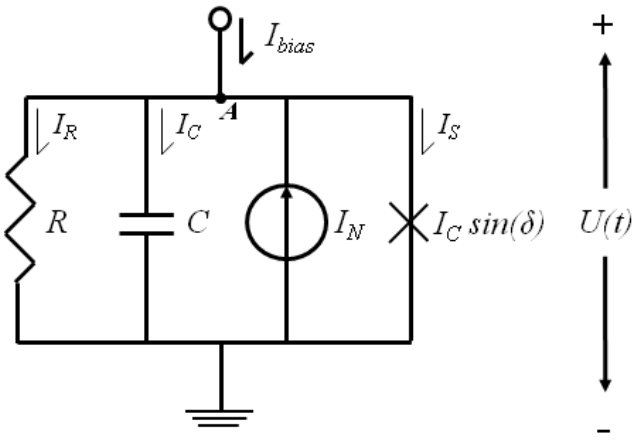

Figure 2.2: Resistor-Capacitor-Shunted-Junction electrical schematic

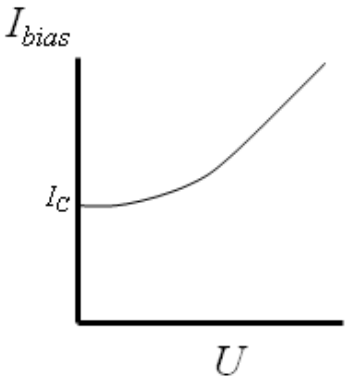

Figure 2.3: Example Josephson junction I-V electrical characteristic curve

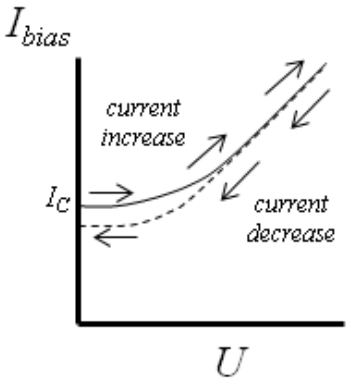

Figure 2.4: Example Josephson junction I-V electrical characteristic curve showing a hysteresis loop

The RCSJ model has been experimentally shown to accurately describe the electrical behavior of the junction at low superconducting temperatures, however the model is less accurate for high superconducting temperatures [16].

The instantaneous junction voltage $U(t)$ is found using Kirchoff's current law on the RCSJ circuit representation to write the nodal current equation at node A, shown

as $I_{bias} + I_N = I_R + I_C + I_S$. The current equations for the resistor current $I_R = U(t)/R$, capacitor current $I_C = C\partial U(t)/\partial t$, and junction current $I_S = I_C \sin(\delta)$ are substituted into the nodal current equation to produce an equation for the junction voltage $U(t)$, expressed as

$$I_{bias} + I_N = \frac{U(t)}{R} + C\frac{\partial U(t)}{\partial t} + I_C \sin(\delta) \tag{2.8}$$

where I_{bias} is the junction bias current, I_N is the thermal noise current in the junction, R is the junction resistance, C is the junction capacitance, I_C is the junction critical current, δ is the phase difference of superconducting wave function across the junction, and $U(t)$ is the instantaneous junction voltage. By taking the time-derivative of the Josephson phase relation, $\dot{\delta} = \frac{2\pi}{\phi_0}U$, a second order relationship between $\partial U(t)/\partial t$ and phase δ is produced.

$$\frac{\partial \dot{\delta}}{\partial t} = \frac{\phi_0}{2\pi}\ddot{\delta} = \frac{\partial U(t)}{\partial t} \tag{2.9}$$

The second order phase relationship given by Equation 2.9, and the Josephson phase relation given by Equation 2.7, are used to write the nodal current equation from Equation 2.8, as [16],

$$I_{bias} + I_N = \frac{1}{R}\frac{\phi_0}{2\pi}\dot{\delta} + C\frac{\phi_0}{2\pi}\ddot{\delta} + I_C sin(\delta) \tag{2.10}$$

The phase δ quantities from Equation 2.10 are separated from the current quantities to produce,

$$C\frac{\phi_0}{2\pi}\ddot{\delta} + \frac{1}{R}\frac{\phi_0}{2\pi}\dot{\delta} = I_{bias} - I_C sin(\delta) + I_N \tag{2.11}$$

The junction's critical current I_C is used to normalize Equation 2.11, leading to the development and introduction of two critical junction parameters, the Stewart-McCumber parameter and the characteristic frequency.

$$\frac{C}{I_C}\frac{\phi_0}{2\pi}\ddot{\delta} + \frac{1}{I_C R}\frac{\phi_0}{2\pi}\dot{\delta} = \frac{I_{bias}}{I_C} - sin(\delta) + \frac{I_N}{I_C} \tag{2.12}$$

The constant terms are manipulated and arranged to allow the introduction of the Stewart-McCumber parameter β_C and junction's characteristic frequency ω_C. The equation is

manipulated into the form,

$$\frac{2\pi I_C R^2 C}{\Phi_0}\frac{(\Phi_0)^2}{(2\pi R I_C)^2}\ddot{\delta} + \frac{\Phi_0\dot{\delta}}{2\pi I_C R} = \frac{I}{I_C} - \sin(\delta) + \frac{I_N}{I_C} \tag{2.13}$$

The Stewart-McCumber parameter β_C is used to quantify the level of damping in the junction and indicates the amount of hysteresis observed in the I-V characteristic curve, and is defined as,

$$\beta_C \equiv \frac{2\pi}{\Phi_0} I_c R^2 C \tag{2.14}$$

The characteristic frequency ω_C represents the resonant frequency of the junction and is defined as,

$$\omega_C \equiv \frac{2\pi}{\Phi_0} I_C R \tag{2.15}$$

The Stewart-McCumber parameter and the characteristic frequency are substituted into Equation 2.13 to produce,

$$\beta_C \frac{\ddot{\delta}}{\omega_C^2} + \frac{\dot{\delta}}{\omega_C} = \frac{I_{bias}}{I_C} - \sin(\delta) + \frac{I_N}{I_C} \tag{2.16}$$

Equation 2.16 is a second order ordinary differential equation (ODE) that defines the electrical operating dynamics for the Josephson junction for normal time. The instantaneous junction voltage is found using the Josephson phase relationship, $\dot{\delta} = \frac{2\pi}{\phi_0} U(t)$.

The numerical precision of the solution relies on the numerical precision of the numbers involved. Equation 2.16 is normalized by introducing the time relationship, $\tau = \omega_C^{-1}$, to allow computer analysis of the junction response to remain with the numerical precision of floating point representation, specifically with using the small values Φ_0, ω_C^{-1}, and I_C. The normalized time relationship is given by [16],

$$\tau = \omega_C^{-1} = \frac{\Phi_0}{2\pi I_C R} \tag{2.17}$$

with the magnetic flux quantum Φ_0, critical current I_C, and resistance R. The relationships for the first and second derivatives with respect to normalized time are given by,

$$\dot{\delta} = \frac{\partial \delta}{\partial \tau} = \frac{\partial \delta}{\partial \tau}\frac{\partial \tau}{\partial t} \tag{2.18}$$

$$\ddot{\delta} = \frac{\partial^2 \delta}{\partial t^2} = \frac{\partial^2 \delta}{\partial \tau^2}\frac{\partial \tau^2}{\partial t^2} \tag{2.19}$$

with $\frac{\partial \tau}{\partial t} = \tau = \omega_C^{-1}$ and $\frac{\partial \tau^2}{\partial t^2} = \tau^2 = \omega_C^{-2}$. The time normalization produces the model equation,

$$\beta_C \ddot{\delta} + \dot{\delta} = \frac{I_{bias}}{I_C} - I_C \sin(\delta) + \frac{I_N}{I_C} \tag{2.20}$$

Equation 2.20 is a second order ODE that defines the electrical operating dynamics for the Josephson junction in normalized time. Equation 2.20 reduces to the resistively shunted junction (RSJ) model equation when the condition $\beta_C \ll 1$ is used [16].

The Josephson junction I-V characteristic curve is analytically expressed with the equation [16],

$$V = R(I_{bias}^2 - I_C^2)^{1/2} \tag{2.21}$$

for the condition $I_{bias} \geq I_C$ with the time-averaged junction voltage V, resistance R, bias current I_{bias}, and critical current I_C. Equation 2.21 analytically defines the Josephson junction I-V electrical characteristic curve, but excludes the thermal noise current I_N. The thermal noise current, I_N, in the junction has a spectral density of [16],

$$S_I(f) = \frac{4k_B T}{R} \tag{2.22}$$

where, k_B is Boltzmann's constant, T is the operating temperature, and R is the resistance. The thermal noise current is modeled in the RCSJ circuit representation as an additional current source and is accurately predicted for low superconducting temperatures, however the current is off by an order of magnitude for high superconducting temperatures [16].

2.2.6 Superconducting Quantum Interference Device.

The SQUID is a device used to transduce magnetic flux into voltage. The SQUID operates on the Josephson Effect and magnetic flux quantization phenomena for the

ability to transduce magnetic flux to voltage, allowing for sensitive measurements of magnetic flux. The SQUID remains the most sensitive magnetic flux measurement device available due to its low thermal noise characteristics and high magnetic flux sensitivity [15]. The SQUID is constructed using a combination of Josephson junction placed inside a superconducting ring. There are three configurations of the SQUID: the radio frequency (RF) SQUID, direct current (DC) SQUID, and the BI-SQUID.

2.2.6.1 Radio Frequency SQUID.

The RF SQUID consists of one Josephson junction placed in a superconducting ring with the geometry shown in Figure 2.5. The electrical operating dynamics are defined by

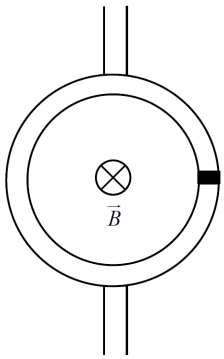

Figure 2.5: RF SQUID geometry

one Josephson junction and the principle of flux quantization to produce [16],

$$C\frac{\partial^2\delta}{\partial t^2} + \frac{1}{R}\frac{\partial\delta}{\partial t} + \left(\frac{2\pi}{\Phi_0}\right)^2 \frac{\partial U(t)}{\partial\delta} = I_N\frac{2\pi}{\Phi_0} \tag{2.23}$$

with capacitance C, phase difference δ, resistance R, instantaneous junction voltage $U(t)$, and noise current I_N. The RF SQUID voltage output is measured using an inductively coupled resonant circuit, thus the voltage is not directly read from the RF SQUID itself. The superconducting loop forms an inductance that is mutually coupled with the inductance of an parallel inductor-capacitor (L-C) resonant circuit. The L-C component values are chosen to allow a RF resonance to develop, with typical resonance frequencies ranging

from 20 MHz to 10 GHz. The amplitude of the RF voltage is periodic with the applied flux, containing a period of Φ_0 [16].

The energy sensitivity of the RF SQUID is compared with the energy sensitivity of the direct current SQUID by T. Ryhanen and H. Seppa [35]. They show the RF SQUID typically contains an energy sensitivity of $2k_BT_A/(\omega_C\beta_Lk^2Q_T)$ with T_A being the amplifier temperature, k being a inductance coupling coefficient, and Q_T being the resonant circuit Q-value. The DC SQUID typically contains an energy sensitivity of $8k_BT/(\omega_C)$. Using their design parameters for SQUID inductance 0.2 nH, resonant circuit inductance of 10 nH, SQUID shunt resistance of 1.3 Ω, the energy sensitivity for the RF SQUID is $2\times10^{-27}J/Hz$ and $7\times10^{-32}J/Hz$ for the DC SQUID. The RF SQUID is less sensitive than the DC SQUID, but it was the preferred SQUID for early research because it only contained one Josephson junction. The ability to fabricate reliable junctions proves to be difficult, especially with high temperature superconductivity [28].

2.2.6.2 Direct Current SQUID.

The DC SQUID consists of two Josephson junctions arranged symmetrically around a superconducting ring using the geometry shown in Figure 2.6. The RCSJ circuit representation for the DC SQUID is shown in Figure 2.7. The superconducting ring forms an inductance L and is incorporated into the circuit representation. The magnetic flux passing through the superconducting ring is converted to a voltage that it oscillatory with a period of Φ_0 [16].

The electrical operating dynamics are defined by two Josephson junctions and the relationship between the phase differences for each junction is given by the principle of flux quantization. The DC SQUID electrical dynamics are modeled using the equations

[16],

$$\frac{I_{bias}}{2} + J = I_{C,1} sin(\delta_1) + \frac{\Phi_0}{2\pi R_1}\dot{\delta} + \frac{\Phi_0}{2\pi} C_1 \ddot{\delta} + I_{N,1} \tag{2.24}$$

$$\frac{I_{bias}}{2} - J = I_{C,2} sin(\delta_2) + \frac{\Phi_0}{2\pi R_2}\dot{\delta} + \frac{\Phi_0}{2\pi} C_2 \ddot{\delta} + I_{N,2} \tag{2.25}$$

$$\delta_2 - \delta_1 = \frac{2\pi}{\Phi_0}(\Phi_A + LJ) \tag{2.26}$$

where Φ_A is the applied flux, L is the inductance of the superconducting ring, and J is the screening supercurrent circulating around the ring, δ_1 and δ_2 are the phase differences across Josephson junction 1 and 2, respectively, capacitance C_1 for junction 1 and C_2 for junction 2, resistance R_1 for junction 1 and R_2 for junction 2, critical current $I_{C,1}$ for junction 1 and $I_{C,2}$ for junction 2, and thermal noise current $I_{N,1}$ for junction 1 and $I_{N,2}$ for junction 2. The superconducting ring is assumed to be perfectly symmetric, excluding

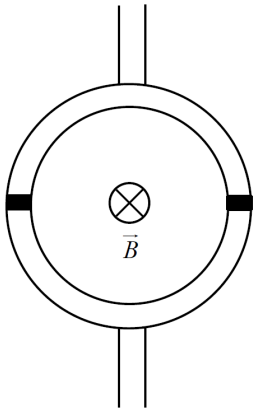

Figure 2.6: DC SQUID Geometry

any effects resulting from asymmetry. The two Josephson junctions are assumed to be perfectly identical, allowing for the two Josephson junctions to be model as one. The

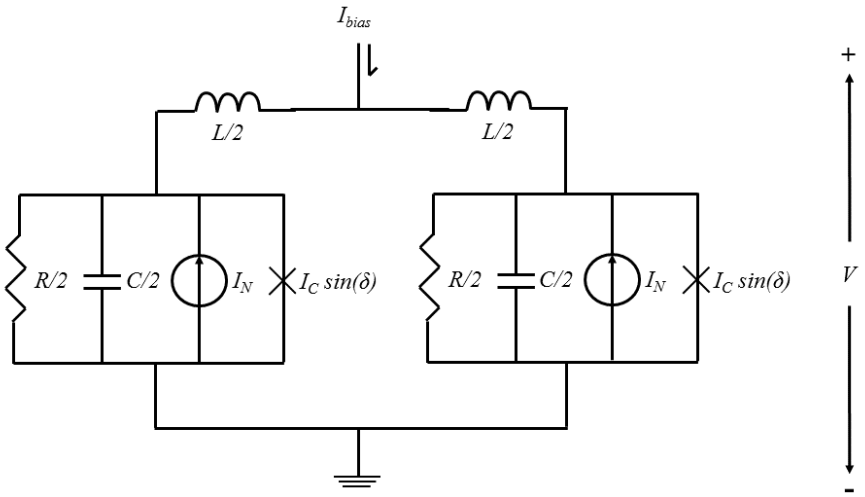

Figure 2.7: DC SQUID electrical schematic

identical junctions result in the combination of the electrical parameters as,

$$R = 2\frac{R_1 R_2}{R_1 + R_2}$$
$$C = \frac{C_1 + C_2}{2}$$
$$I_C = \frac{I_{C,1} + I_{C,2}}{2}$$

The constant terms are manipulated and the Stewart-McCumber damping parameter β_C and junction characteristic frequency ω_C are used to reduce Equations 2.24, 2.25, and 2.26 into,

$$\frac{I_{bias}}{2} + J = I_C sin(\delta_1) + \frac{\dot{\delta_1}}{\omega_C} + \beta_C \frac{\ddot{\delta_1}}{\omega_C^2} + I_N \tag{2.27}$$

$$\frac{I_{bias}}{2} - J = I_C sin(\delta_2) + \frac{\dot{\delta_2}}{\omega_C} + \beta_C \frac{\ddot{\delta_2}}{\omega_C^2} + I_N \tag{2.28}$$

$$\delta_2 - \delta_1 = \frac{2\pi}{\Phi_0}(\Phi_A + LJ) \tag{2.29}$$

Equations 2.27, 2.28 and 2.29 are normalized into dimensionless form using the junction critical current I_C, time normalization $\tau = \omega_C^{-1}$, and the phase derivative relationships from Equation 2.18 and 2.19. The normalized variables $i_{bias} = I_{bias}/I_C$, $j = J/I_C$, and $i_n = I_N/I_C$,

and normalized phase derivatives $\dot{\delta}$ and $\ddot{\delta}$ are used to produce the equation set,

$$\frac{i_{bias}}{2} + j = sin(\delta_1) + \dot{\delta_1} + \beta_C \ddot{\delta_1} + i_n \tag{2.30}$$

$$\frac{i_{bias}}{2} - j = sin(\delta_2) + \dot{\delta_2} + \beta_C \ddot{\delta_2} + i_n \tag{2.31}$$

$$\delta_2 - \delta_1 = \frac{2\pi}{\Phi_0}(\Phi_A + LJ) \tag{2.32}$$

The normalization allows the computed solution to remain within the numerical precision of floating point representation. The modulation parameter β_L is used to reduce the phase relationship and is defined as,

$$\beta_L = \frac{2LI_C}{\Phi_0} \tag{2.33}$$

The final expression for the DC SQUID equations are,

$$\frac{i_{bias}}{2} + j = sin(\delta_1) + \dot{\delta_1} + \beta_C \ddot{\delta_1} + i_n \tag{2.34}$$

$$\frac{i_{bias}}{2} - j = sin(\delta_2) + \dot{\delta_2} + \beta_C \ddot{\delta_2} + i_n \tag{2.35}$$

$$\delta_2 - \delta_1 = 2\pi(\phi_a + \frac{1}{2}\beta_L j) \tag{2.36}$$

where ϕ_a is the normalized applied flux $\phi_a = \frac{\Phi_A}{\Phi_0}$, j is the normalized circulating current $j = \frac{J}{I_C}$, i_{bias} is the normalized bias current $i_{bias} = \frac{I_{bias}}{I_C}$, i_n is the normalized junction thermal noise $i_n = \frac{I_N}{I_C}$, and δ_1 and δ_2 are the phase differences across Josephson junction 1 and 2, respectively.

The DC SQUID is most often operated with a flux locked loop circuit to linearize the response of the SQUID [16]. The flux feedback modifies the flux state inside the ring so that the flux is opposed and canceled. The result is the output voltage exhibits a linear response to the input flux.

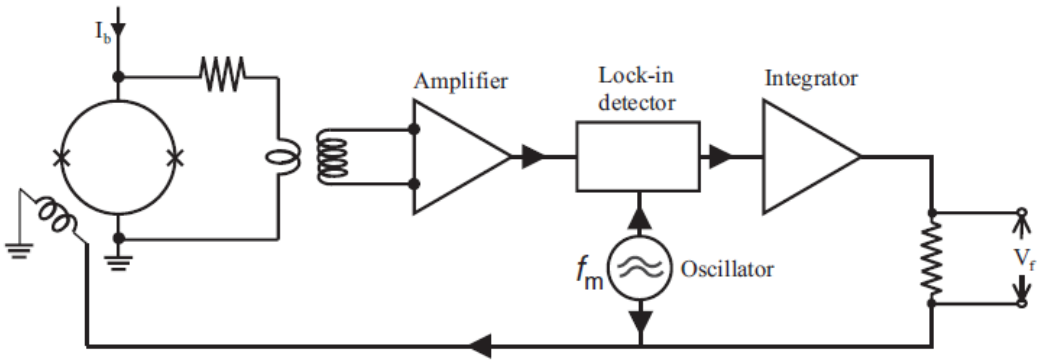

Figure 2.8: Flux lock loop circuit for a DC SQUID [16].

2.2.7 Current Research.

The development of superconducting research has been primarily focused in the field of medical research. The high magnetic sensitivity of these devices matches well with magnetic resonance imaging (MRI), thus they are the primary sensing element of several MRI systems around the world. Although SQUIDs are sensitive, they have seen limited antenna design development due to the limited dynamic range of the support electronics used in the SQUID designs. The breakthrough came with the development of the superconducting quantum interference filter (SQUIF) in 2000 [33]. This new configuration allows for the linearization of the voltage transfer function and opened up the possibility of these devices to be used as antenna elements however the fabrication of reliable junctions has proven to be challenging. In 2009, a new configuration was discovered that also linearizes the voltage transfer function. This configuration adds an additional junction across the middle of the DC SQUID, and is termed the BI-SQUID [41]. This configuration adds a third junction across the middle of the superconducting loop to achieve a linearized transfer function.

2.2.7.1 BI-SQUID.

The BI-SQUID is a tri-junction device that expands the linear region of the flux to voltage transfer function. The BI-SQUID is based on the DC SQUID design, adding an additional Josephson junction across the superconducting ring. Figure 2.9 shows the geometry of the BI-SQUID device. The electrical operating dynamics of the BI-SQUID

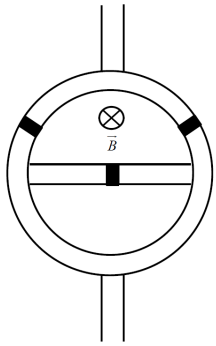

Figure 2.9: BI-SQUID Geometry

are given by the equations,

$$\dot{\delta_1} = \frac{i_{bias}}{2} - \frac{1}{3L}(\delta_1 - \delta_2 - \delta_3) + \frac{1}{3} i_{C3} \sin(\delta_2 - \delta_1) - \frac{2}{3}\sin(\delta_1) - \frac{1}{3}\sin(\delta_2) \tag{2.37}$$

$$\dot{\delta_2} = \frac{i_{bias}}{2} + \frac{1}{3L}(\delta_1 - \delta_2 - \delta_3) - \frac{1}{3} i_{C3} \sin(\delta_2 - \delta_1) - \frac{1}{3}\sin(\delta_1) - \frac{2}{3}\sin(\delta_2) \tag{2.38}$$

where, i_{C3} is the critical current of the third junction, L is the SQUID inductance, $\delta_{1,2,3}$ is the phase across the 1st, 2nd, and 3rd junctions, respectively, and i_{bias} is the normalized bias current for the BI-SQUID.

2.2.7.2 Superconducting Quantum Interference Filter.

The SQUIF is composed of a parallel configuration of DC SQUIDs with a uniform distribution placed on the area contained by each superconducting ring. The SQUIF is designed to linearize the flux to voltage transfer function. The uniformly distributed areas allow for the coherent addition of detected magnetic flux.

2.3 Signal Power Transmission

The Poynting vector is the quantity used to describe the power associated with propagating EM radiation [10, 11]. This quantity relates the power of the EM wave to the field intensity of the electric and magnetic fields. The Poynting vector is defined as

$$\vec{\mathcal{P}} = \vec{\mathcal{E}} \times \vec{\mathcal{H}} \tag{2.39}$$

where $\vec{\mathcal{P}}$ is the instantaneous Poynting vector given in power density (W/m^2), $\vec{\mathcal{E}}$ is the instantaneous electric field intensity (V/m), and $\vec{\mathcal{H}}$ is the instantaneous magnetic field intensity (A/m). The Poynting vector can be used with the power density equation to determine the magnetic field intensity at a distance R. The power density of an isotropic antenna is given by [30, 36]

$$P_r = \frac{P_t}{4\pi R^2} \tag{2.40}$$

where P_r is the received power density (W/m), P_t is the transmit power density (W/m), and R is the distance from the transmitter to the receiver (m). The power density is used to describe the 1 way relationship between the transmitted power to the power density at a distance R and is used to provides the quantitative relationship between the transmitted power of a transmission site, and the power received at the given range R.

III. Methodology

SQUID sensors are used for extremely sensitive magnetic field measurements for various purposes, such as MRI, non-destructive examination (NDE), and material characterization [17]. The physical size of these sensors is limited by lithographic processes but typically range from nanometer to micrometer size SQUIDs [16, 34]. The magnetic sensitivity and small footprint of SQUID sensors are applicable as the primary magnetic sensing element for an airborne antenna system. The use of SQUID sensors in an airborne antenna array can potentially increase HF signal interception range. This research explores the use of SQUID sensors for this purpose.

3.1 Research Outline

This research effort is focused on the theoretical examination of SQUID technology with application to airborne HF DF. The SQUID sensor is studied to determine suitability as the primary magnetic field sensing element for an HF DF antenna array. The HF sensitivity of the device is determined and a performance evaluation is conducted. The following outline is used to complete this effort.

- Select a SQUID sensor for examination
- Study the theoretical performance characteristics of the selected sensor
- Characterize the magnetic field sensitivity performance of the selected sensor
- Simulate HF reception and expected range of the sensor

3.2 SQUID Selection

There are four major SQUID configurations: the RF SQUID, DC SQUID, SQUIF, and the BI-SQUID. Each of these sensors are based on a superconducting ring design with each containing a unique number of Josephson junctions, however, the SQUIF is constructed

using a unique arrangement of DC SQUIDs. Each sensor possesses a different magnetic flux resolution ability and thermal noise level. The DC SQUID has been experimentally shown to be the most sensitive magnetic flux detector [16]. This research is focused on maximizing the HF magnetic field reception using these devices, therefore the DC SQUID is the best candidate for this research. If the DC SQUID cannot receive HF EM energy, then by similarity, the other configurations will not be able to receive HF EM energy. The DC SQUID examination begins with computing the electrical operating characteristic for the device .

3.3 Numerical Simulation

The electrical characteristic of the DC SQUID depend on the electrical characteristic for the Josephson junction. The Josephson relations, presented in Chapter 2 section 2.2.4, equations 2.6 and 2.7 are used with the RCSJ circuit representation to produce a second order ODE circuit equation, allowing for a numerical examination of the electrical characteristic for the Josephson junction.

3.3.1 Partial Differential Equation Numerical Solvers.

The advent of digital computing has allowed development of numerical techniques for computing solutions to complex equations. Differential equations often require the assistance of numerical techniques to compute solutions because analytic solutions do not exist [37]. There are several numerical techniques available for solving partial differential equation (PDE) and ODE. The most used numerical solvers for differential equations are,

- Euler Method
- Improved Euler Method
- Runge-Kutta Family of Methods

These methods compute the numerical solution to an initial value problem (IVP) given by the differential equation (DE) along with an initial condition (IC).

$$(IVP)\begin{cases} y'(t) = f(t, y(t)) & \text{(DE)} \\ y(a) = y_0 & \text{(IC).} \end{cases} \tag{3.1}$$

The solution $y(t)$ is computed by incrementally stepping through the equation $f(t, y(t))$ at a specified step size h.

The Runge-Kutta-Fehlberg (RKF)-45 method is member of the Runge-Kutta family of numerical methods. The RKF-45 method is an adaptive and multi-step numerical solver for IVPs. Given an initial step size, h, and a predefined error limit, ε, the solution is computed using a fifth order solution approximation. The following scheme describes the RKF-45 method,

$$t_0 = a, y_0 = y(a), h = \text{initial step size}, \varepsilon = \text{error tolerance}$$

$$k_1 = hf(t_n, y_n) \tag{3.2}$$

$$k_2 = hf(t_n + \frac{h}{4}, y_n + \frac{1}{4}k_1) \tag{3.3}$$

$$k_3 = hf(t_n + \frac{3h}{8}, y_n + \frac{3}{32}k_1 + \frac{9}{32}k_2) \tag{3.4}$$

$$k_4 = hf(t_n + \frac{12h}{13}, y_n + \frac{1932}{2197}k_1 - \frac{7200}{2197}k_2 + \frac{7296}{2197}k_3) \tag{3.5}$$

$$k_5 = hf(t_n + h, y_n + \frac{439}{216}k_1 - 8k_2 + \frac{3680}{513}k_3 - \frac{845}{4104}k_4) \tag{3.6}$$

$$k_6 = hf(t_n + \frac{h}{2}, y_n - \frac{8}{27}k_1 + 2k_2 + \frac{3544}{2565}k_3 + \frac{1859}{4104}k_4 - \frac{11}{40}k_5) \tag{3.7}$$

with the initial condition for time t_0, the initial condition for the function y_0, step size h, error tolerance ε, and solution approximations k_1, k_2, k_3, k_4, k_5, and k_6. The solution approximations are computed in sequential order starting with k_1. The approximations k_{2-6} use the previous approximation within the computation. The final solution is computed by linearly combining the approximations k_{1-6} to produce a fifth and fourth order solution. The step size is adaptive and is dependent on the local truncation error estimate, E, taken

as the magnitude of the difference between the fifth and fourth order solutions.

$$z_{n+1} = y_n + \frac{25}{216}k_1 + \frac{1408}{2565}k_3 + \frac{2197}{4104}k_4 - \frac{1}{5}k_5 \tag{3.8}$$

$$y_{n+1} = y_n + \frac{16}{135}k_1 + \frac{6656}{12825}k_3 + \frac{28561}{56430}k_4 - \frac{9}{50}k_5 + \frac{2}{55}k_6 \tag{3.9}$$

$$\begin{aligned} E &= |y_{n+1} - z_{n+1}| \\ &= \left|\frac{1}{360}k_1 - \frac{128}{4275}k_3 - \frac{2197}{75240}k_4 + \frac{1}{50}k_5 + \frac{2}{55}k_6\right| \end{aligned} \tag{3.10}$$

The step size adapts to the local truncation error estimate using the predefined error tolerance, ε, and is given by the decision scheme,

- If $E > h\varepsilon$ reduce h to $\frac{h}{2}$ and repeat.
- If $E < \frac{h\varepsilon}{4}$ accept solution, but increase step size to $2h$ for the next iteration.
- Otherwise, continue with the step size.

The step size is adjusted to reduce the local truncation error to provide an accurate solution, however the step size is fixed for the numerical computations performed in this thesis. Sampling theory must be applied in order to perform a frequency analysis using the discrete Fourier Transform (DFT), but a fixed step size is required.

3.3.2 Josephson Junction Numerical Simulation.

The evaluation of DC SQUID technology begins with the examination of the Josephson junction. The Josephson junction is a basic element of the SQUID sensors and enable the unique electrical operating characteristic. The electrical operating characteristic for the junction is defined by the Josephson relations, presented in Chapter 2 section 2.2.4, Equations 2.6 and 2.7. The Josephson relations are used in combination with the RCSJ circuit representation to produce a circuit model equation, allowing for a numerical examination of the electrical characteristic for the junction. The model equation is expressed as a second order ODE given by equation 2.20, and is reproduced for

convenience.

$$\beta_C \ddot{\delta} + \dot{\delta} = \frac{I_{bias}}{I_C} - \sin(\delta) + \frac{I_N}{I_C}$$

Stewart performed an examination of this circuit equation at various β_C damping values [39]. Stewart's results indicate that the damping level does not significantly alter the computed solution. Tesche and Clark use Stewart's result in their examination and optimization of the DC SQUID [40]. Tesche and Clark explain that typical fabricated junctions operate at $\beta_C \approx 1$ [40], however since Stewart's damping result shows minimal difference between $\beta_C \approx 1$ and $\beta_C = 0$, Tesche and Clark proceed to omit β_C from their calculations by setting $\beta_C = 0$. In addition to numerical reduction, the damping parameter β_C is used to quantify the amount of hysteresis seen in the I-V characteristic curve. The amount of hysteresis contained in the I-V characteristic curve is minimized as much as possible by reducing the junction's capacitance. The junction capacitance is determined by the junction's cross sectional area, and is designed to be as small as possible, leading to the negligible capacitance assumption. In practice, a satisfactory damping parameter is $\beta_C < 0.7$ to avoid I-V hysteresis loops in the junction I-V electrical characteristic.

The simulations conducted in this research assume a negligible junction capacitance, and use $\beta_C = 0$ for the numerical evaluations. The circuit model equation is reduced to a first order ODE given by,

$$\dot{\delta} = i_{bias} - \sin(\delta) + i_n \tag{3.11}$$

where δ is the junction phase difference, $\dot{\delta}$ is the normalized time derivative of δ, $U(t)$ is the instantaneous junction voltage, i_{bias} is the normalized bias current $i_{bias} = \frac{I_{bias}}{I_C}$, and i_n is the normalized noise current $i_n = \frac{I_N}{I_C}$.

3.3.2.1 Noise-free Simulation.

The RKF-45 ODE numerical solver is used to compute the voltage solution for the Josephson junction IVP model equation for the noise-free case, $i_n = 0$. The thermal noise current is set to zero to exclude noise effects form the computed voltage solution. The

noise-free IVP for the Josephson junction is given by,

$$(IVP)\begin{cases} \delta' = \frac{I_{bias}}{I_C} - \sin\delta & \text{(DE)} \\ \delta(t_0) = 0 & \text{(IC)} \\ t_0 = 0 & \text{(IC)} \end{cases} \tag{3.12}$$

The RKF-45 solver is implemented to produce a solution for δ'. The instantaneous junction voltage is found using the second Josephson relationship $\frac{\phi_0}{2\pi}\dot{\delta} = U(t)$ to produce,

$$\frac{U(t)}{I_C R} = i_{bias} - \sin\delta \tag{3.13}$$

with the normalized bias current $i_{bias} = \frac{I_{bias}}{I_C}$, critical current I_C, resistance R, and phase difference δ. The instantaneous voltage $U(t)$ is kept in dimensionless form by solving for $\frac{U(t)}{I_C R}$ instead of $U(t)$ directly. $\frac{1}{I_C R}$ is a scaling factor dependent on the critical current of the junction and resistance.

A series of normalized bias current values i_{bias} are used to check the proper electrical response of the junction. First, the junction is known to develop a voltage for the case when the bias current exceeds the critical current. Second, the junction does not develop a voltage for the case when the bias current does not exceed the critical current. The two voltage response regions to be checked are: $I_{bias} < I_C$ for zero voltage development and $I_{bias} > I_C$ for non-zero voltage development. In the normalized sense, these regions are: $\frac{I_{bias}}{I_C} < 1$ for zero voltage development and $\frac{I_{bias}}{I_C} > 1$ for non-zero voltage development. First, the zero voltage case is checked for appropriate response. The bias current is set as $\frac{I_{bias}}{I_C} = 0.5$ to satisfy the $\frac{I_{bias}}{I_C} < 1$ condition. Figure 3.1 shows the instantaneous junction voltage $U(t)$ versus simulation time τ and Figure 3.2 shows the corresponding error estimate for $U(t)$.

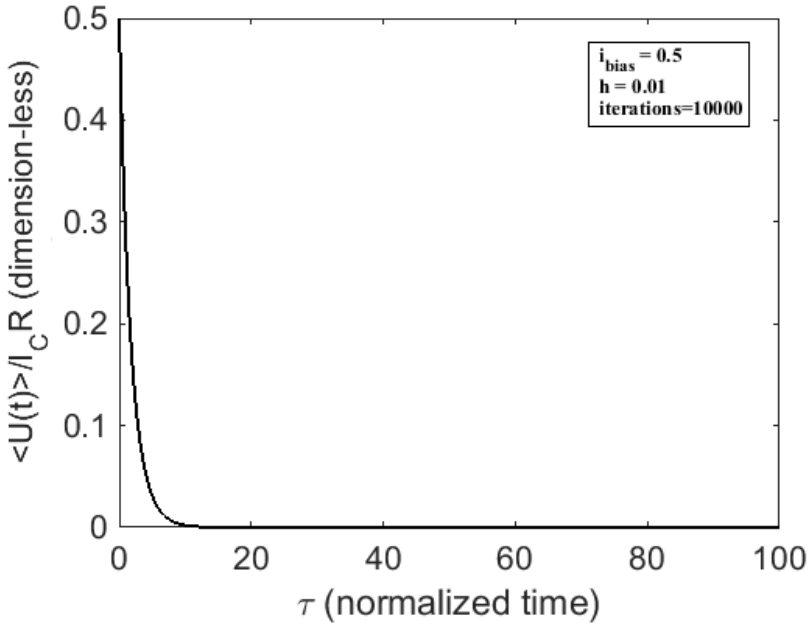

Figure 3.1: Josephson junction voltage response for $I_{bias} = 0.5I_C$

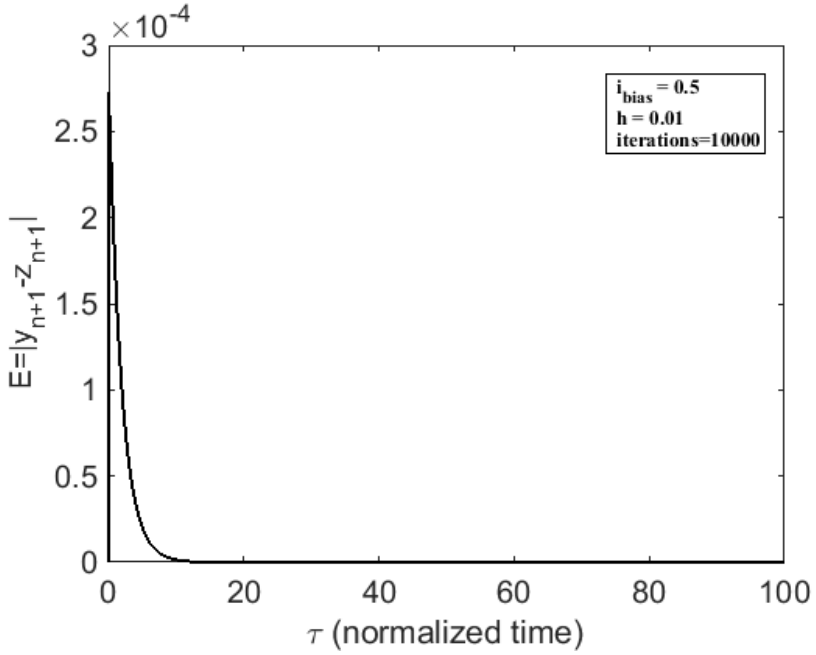

Figure 3.2: Error estimate for the voltage response with $I_{bias} = 0.5I_C$

For Figure 3.1, the instantaneous junction voltage $U(t)$ starts at 0.5, but sharply decreases to zero as the solution progresses, indicating the proper junction response by showing zero voltage development across the junction.

Next, the bias current is chosen to exceed the critical current, and the junction voltage response is observed. A sinusoidal instantaneous voltage waveform is expected because the solution for the phase will take the form $\delta = A\omega_C t$ with A a constant. The instantaneous voltage solution will then take the form $\sin(A\omega_C t)$. The frequency of the instantaneous voltage solution will increase as the constant A increases. The bias current used for this simulation is $\frac{I_{bias}}{I_C} = 2$. Figure 3.3 shows the instantaneous junction voltage $U(t)$ versus simulation time τ and Figure 3.4 shows the corresponding error estimate.

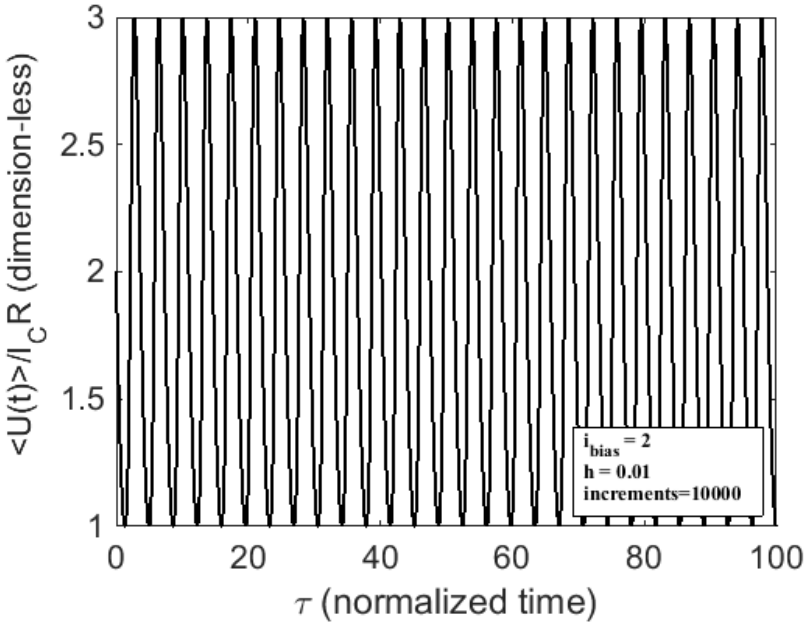

Figure 3.3: Josephson junction voltage response for $I_{bias} = 2I_C$

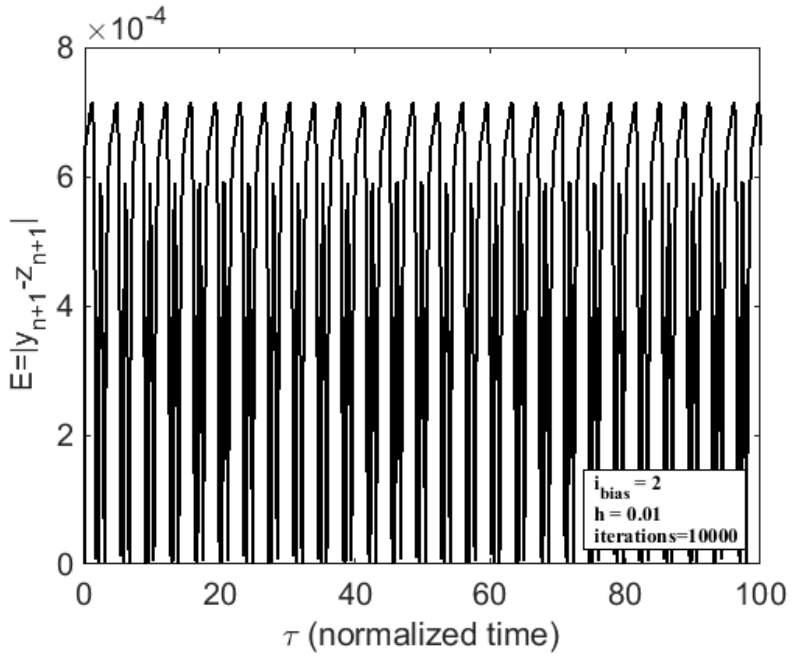

Figure 3.4: Error estimate for the voltage response with $I_{bias} = 2$

Figure 3.3 shows the development of a sinusoidal voltage across the junction when the bias current exceeds the critical current. The time average of the instantaneous junction voltage is $\langle U(t) \rangle = 1.855$.

The time-average will be effected by the time duration over which it is computed. The duration will need to be sufficiently long to achieve an accurate time-average solution. The time duration used to compute the time-average is varied to determine minimum duration length required for an accurate time-average, since the time-averaged voltage will be used to compute the I-V characteristic curve. A bias current of $\frac{I_{bias}}{I_C} = 2$ is used to complete the duration length analysis. Figure 3.5 shows time-averaged junction voltage as a function of the time-averaging interval. The time-average solution converges to the voltage mean at approximately 6000 τ time units and represents the minimum simulation length required for computing the time-average.

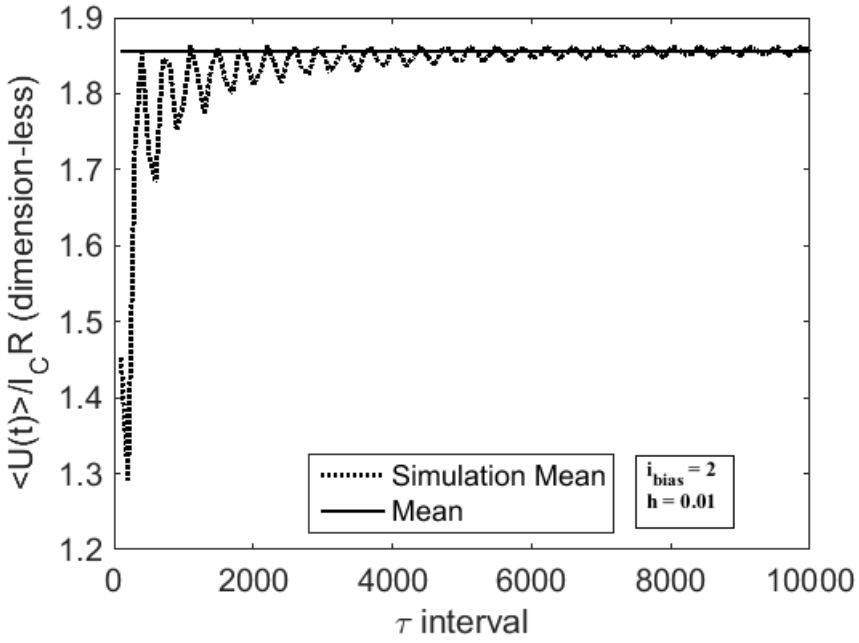

Figure 3.5: Convergence of the simulation mean to the voltage mean with $I_{bias} = 2$

The electrical operating characteristic of the Josephson junction is defined by the I-V characteristic curve. The I-V characteristic curve depicts the electrical relationship between the time-averaged instantaneous junction voltage with the junction bias current. The simulations are completed using normalized current and voltage values since specific resistance, capacitance, and inductance values are not yet simulated. The normalized bias currents spanning the numerical set $[0 \ldots 3]$ are chosen to complete this simulation so the voltage response for the junction can be checked. The instantaneous junction voltage is computed for each bias current and a time-averaged voltage is produced for the I-V characteristic curve. Figure 3.6 shows the resulting I-V characteristic curve for the Josephson junction. The I-V characteristic curve demonstrates the expected electrical behavior of the Josephson junction by showing a non-zero voltage for bias current values exceeding the critical current and zero-voltage values for when the bias current does not exceed the critical current.

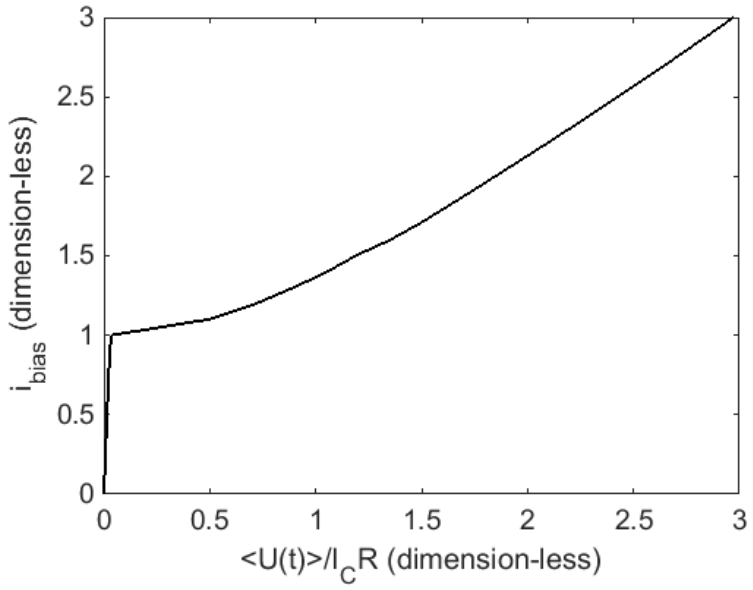

Figure 3.6: Noisefree I-V characteristics of the Josephson junction

The RKF-45 implementation is verified using a comparison between the computed solutions with the analytical solutions for instantaneous voltage and the I-V characteristic curve. The instantaneous voltage across the junction is analytically expressed as [16],

$$u(t) = \frac{i_{bias}^2 - 1}{i_{bias} + \cos \omega t} \tag{3.14}$$

for $i_{bias} = \frac{I_{bias}}{I_C} > 1$ and with $\omega = \omega_C (i_{bias}^2 - 1)^{\frac{1}{2}}$. The time-averaged voltage $\langle v \rangle$ that develops across the junction is given by the expression [16],

$$\langle v \rangle = \sqrt{i_{bias}^2 - 1} \tag{3.15}$$

for $i_{bias} > 1$, with the normalized bias current i_{bias}, and the time-averaged voltage $\langle v \rangle$. The instantaneous junction voltage is computed for the bias currents $i_{bias} = \{1.1, 2, 5, 8\}$ to perform a comparison between the computed voltage and the analytical voltage. The comparison shows that the two solutions are similar but not exact.

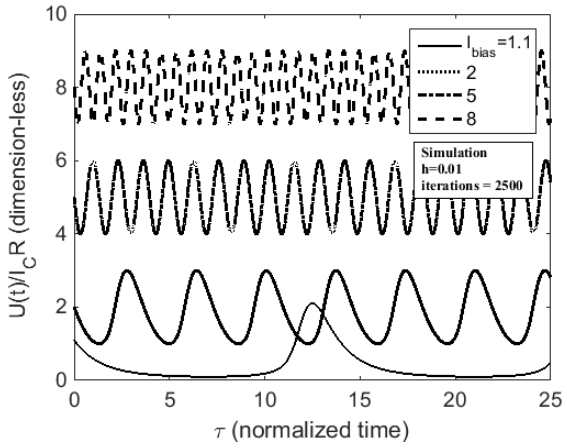

Figure 3.7: Numerically computed Josephson junction voltage solution using bias current values 1.1, 2, 5, and 8

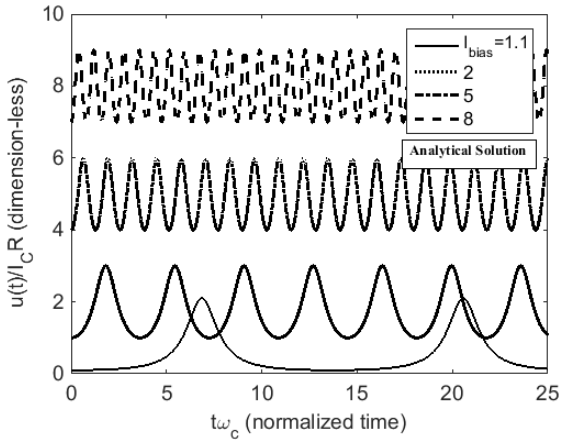

Figure 3.8: Analytically computed Josephson junction voltage solution using bias current values 1.1, 2, 5, and 8

Figure 3.7 presents the RKF-45 computed instantaneous junction voltage and Figure 3.8 presents the analytical instantaneous junction voltage. There are slight variations between the two solution sets. The phase of the RKF-45 voltage solution is distorted and contains a phase offset of 20 degrees compared to the analytical voltage solution. These artifacts may be attributed to the RKF-45 numerical technique; but these differences do not significantly affect the final time-averaged junction voltage computed for the I-V curve, shown in Figure 3.9. The I-V characteristic curve is computed using a bias current range $i_{bias} \in \{0 \ldots 5\}$ to show the amount of error between the RKF-45 numerical solution and the analytical solution over a large range.

Figure 3.9 shows the comparison between the voltage simulation of the I-V curve with the analytical expression given by 3.15. The slight differences between the two solutions can be attributed to the computational variation in the RKF-45 numerical solution. The differences seen do not significantly influence the accuracy of the computed solutions with a maximum error between the two data sets being 0.14, indicating the RKF-45 numerical

technique is successful for numerically computing junction voltage solutions. The error between these two data sets is shown in Figure 3.10. Next, the RKF-45 method is used to examine the effects of thermal noise in the Josephson junction.

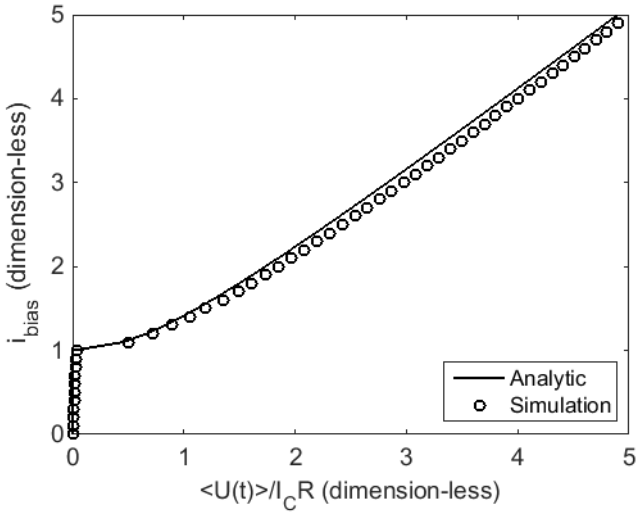

Figure 3.9: Josephson junction I-V characteristic computed using the RKF-45 solver and the analytical equation

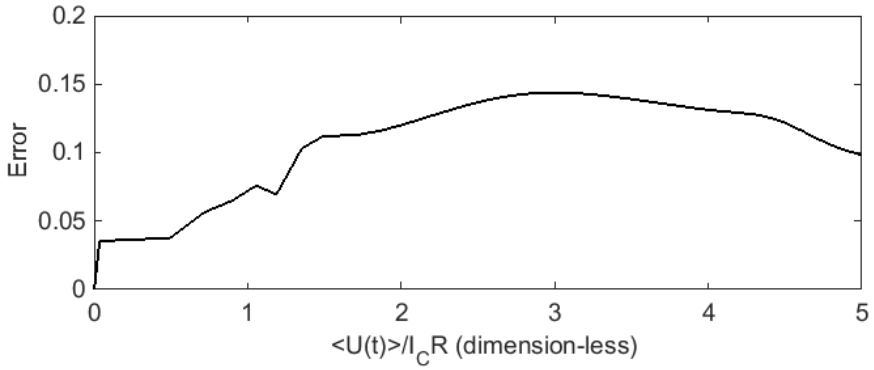

Figure 3.10: Difference between the RKF-45 I-V solution and the analytical voltage solution shown in the I-V characteristic curve

3.3.2.2 Thermal Noise Simulation.

The Josephson junction operates at thermal temperatures ranging from 4.7 to 77 Kelvin, however, thermal fluctuations are still present at these temperatures. The thermal fluctuations contribute toward a noise current flowing through the junction. The spectral

density of the thermal noise current through a Josephson junction is given by [16],

$$S_I(\omega) = \frac{2k_BT}{\pi R} \tag{3.16}$$

$$S_I(f) = \frac{2k_BT}{R} \tag{3.17}$$

where k_B is Boltzmann's constant, T is the operating temperature (K), R is the junction resistance (Ω). The Wiener-Khintchine-Einstein Theorem relates to the noise spectral density as a time-domain statistical process. For a non-stationary process, the theorem is written as [32]

$$S_{XX}(f) = \int_{-\infty}^{\infty} \langle R_{XX}(t, t+\tau)\rangle e^{-j2\pi f\tau} d\tau \tag{3.18}$$

with the spectral density $S_{XX}(f)$, and auto correlation sequence R_{XX}. The time-average is denoted by $\langle\rangle$, The junction spectral density is normalized into dimensionless units so that it may be included into the junction model equation.

The normalization starts with computing the time-average auto correlation sequence using the normalized noise current.

$$S_i(\omega) = \int_{-\infty}^{\infty} \langle \frac{I_N}{I_C}(t)\frac{I_N}{I_C}(t+\tau)\rangle e^{-j2\pi f\tau} d\tau = \frac{2k_BT}{\pi R I_C^2} \tag{3.19}$$

Additional parameters ϕ_0 and 2π are introduced to produce,

$$S_i(\omega) = \frac{2\pi}{2\pi}\frac{\phi_0}{\phi_0}\frac{2k_BT}{\pi R I_C^2} = \frac{2}{\pi}\frac{2\pi k_BT}{\phi_0 I_C}\frac{\phi_0}{2\pi I_C R} \tag{3.20}$$

A noise normalization parameter, Γ, is introduced and defined as $\Gamma = (2\pi k_BT)/(\phi_0 I_C)$ [16]. Γ and the junction frequency ω_C are used to reduce the expression into

$$S_i(\omega) = 2\frac{2\pi k_BT}{\phi_0 I_C}\frac{\phi_0}{2\pi I_C R} = \frac{2\Gamma}{\pi\omega_C} \tag{3.21}$$

The noise current is modeled in the time-domain as variable with a Gaussian distribution having the statistical properties [16],

$$\langle i_n(t)\rangle = 0 \tag{3.22}$$

$$\langle i_n(t), i_n(t+\tau)\rangle = \frac{2\Gamma}{\omega_c}\delta(\tau) \tag{3.23}$$

where δ is the Dirac delta function. Equation 3.11 is numerically solved using the RKF-45 technique to compute the junction's instantaneous voltage. The noise current, i_n is implemented as a Gaussian distributed random variable with zero mean and variance $2\Gamma/\omega_C$. A set of Γ values spanning from 0 to 1 are used to compute the I-V electrical characteristic. Figure 3.11 shows the numerically computed I-V characteristics for the Josephson junction with various Γ thermal noise values. The introduction of the thermal noise current tapers the bottom end of the I-V characteristic curve.

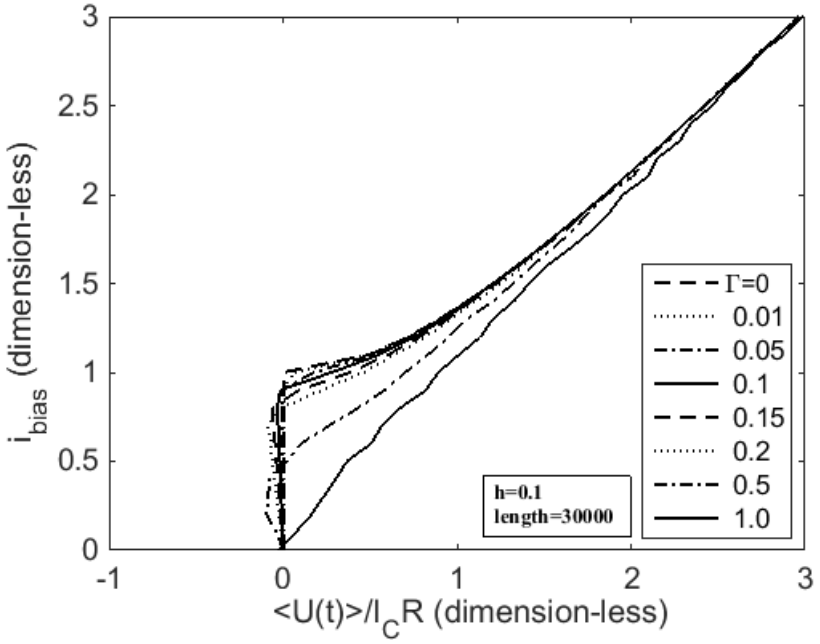

Figure 3.11: I-V electrical characteristic for a Josephson junction with a Gaussian distributed noise current i_n

3.3.3 Direct Current SQUID Numerical Simulation.

The DC SQUID is constructed using two Josephson junctions oriented symmetrically about a superconducting ring. The RCSJ model is used to develop a circuit representation for the numerical examination of the DC SQUID electrical operating characteristics. The results are compared to the data figures from [16, 40]. A successful recreation of data figures verifies the correct implementation of the numerical technique.

The normalized equations that define the operating characteristics of the DC SQUID are reproduced from Chapter 2, section 2.2.6.2, for convenience.

$$\frac{i_{bias}}{2} + j = \beta_C \ddot{\delta_1} + \dot{\delta_1} + sin(\delta_1) + i_n$$
$$\frac{i_{bias}}{2} - j = \beta_C \ddot{\delta_2} + \dot{\delta_2} + sin(\delta_2) + i_n$$
$$\delta_2 - \delta_1 = 2\pi(\phi_a + \frac{1}{2}\beta_L j)$$

The Josephson junctions are assumed to have negligible capacitance, $\beta_C = 0$, reducing the equation describing the electrical operating characteristics for the DC SQUID to a first order ODE, given by the IVP,

$$(IVP)\begin{cases} \frac{i_{bias}}{2} + j = \dot{\delta_1} + sin(\delta_1) + i_n & \text{(DE)} \\ \frac{i_{bias}}{2} - j = \dot{\delta_2} + sin(\delta_2) + i_n & \text{(DE)} \\ \delta_2 - \delta_1 = 2\pi(\phi_a + \frac{1}{2}\beta_L j) & \text{(Phase Relation)} \\ t_0 = 0 & \text{(IC)} \\ d_0 = 0 & \text{(IC)} \end{cases} \tag{3.24}$$

The IVP for the DC SQUID is a two dimensional ODE consisting of the two variable parameters δ_1 and δ_2. The value of the modulation parameter β_L determines whether the dimensionality of the DC SQUID IVP can be reduced or remain as a two-dimensional ODE.

3.3.3.1 Dimensionality Reduction with $\beta_L = 0$.

The condition $\beta_L = 0$ reduces the DC SQUID IVP given in Equation 3.24 as a one-dimensional ODE. The DC SQUID phase relationship for $\beta_L = 0$ is reduced into,

$$\delta_2 - \delta_1 = 2\pi\phi_a \tag{3.25}$$

The phase difference for the second Josephson junction, δ_2, is solved for and given by,

$$\delta_2 = \delta_1 + 2\pi\phi_a \tag{3.26}$$

The circulating current passing through the second Josephson junction is solved for as,

$$j = \frac{i_{bias}}{2} - \dot{\delta_2} - \sin\delta_2 + i_n \tag{3.27}$$

Equation 3.26 is substituted into Equation 3.27 to produce,

$$j = \frac{i_{bias}}{2} - \dot{\delta_1} - \sin\delta_1 + 2\pi\phi_a + i_n \tag{3.28}$$

A relationship between δ_1 and δ_2 is found by taking the time-derivative of Equation 3.26 to produce $\dot{\delta_1} = \dot{\delta_2}$, and is applied to Equation 3.28 to produce,

$$j = \frac{i_{bias}}{2} - \dot{\delta_1} - \sin\delta_1 + 2\pi\phi_a + i_n \tag{3.29}$$

Equation 3.29 is substituted into equation 3.24 to produce,

$$i_{bias} - \dot{\delta_1} - \sin\delta_1 + 2\pi\phi_a + i_n = \dot{\delta_1} + \sin\delta_1 + i_n \tag{3.30}$$

Equation 3.30 is reduced to the form,

$$2\dot{\delta_1} = i_{bias} - 2\sin\delta_1 + 2i_n \tag{3.31}$$

Equation 3.31 is divided by 2 to formulate the final expression, given as

$$\dot{\delta_1} = \frac{i_{bias}}{2} - \sin\delta_1 + i_n \tag{3.32}$$

Equation 3.32 is a one dimensional ODE equation that describes the electrical characteristic of the DC SQUID for $\beta_L = 0$. The RKF-45 method is used to produce a solution for Equation 3.32 for the noise-free case $i_n = 0$.

3.3.3.2 Noise-free Numerical Simulation with $\beta_L = 0$.

The noise-free condition is simulated by setting the noise current to zero, $i_n = 0$. The solution to the one dimensional ODE given by Equation 3.32 is computed using the RKF-45 ODE solver. The I-V electrical operating characteristics are produced with a set of bias current values ranging from -3 to 3 for comparison with the data figures presented in [16]

at the end of this section. Figure 3.12 shows the I-V electrical operating characteristic for the DC SQUID over the range of applied magnetic flux values 0, 0.1, 0.2, 0.3, 0.4, and 0.5.

The transfer function shows the time-averaged voltage as a function of the applied magnetic flux and is shown in Figure 3.13. The transfer function is computed using normalized bias currents 1.9, 2.0, and 2.1 to show the time-averaged voltage for the bias currents of 1.9, 2.0, and 2.1. A small zero time-averaged voltage region is shown at a bias current of 1.9. This zero voltage region spans $0.1\phi_a$ and does not provide information for applied magnetic flux values within the 0 to 0.1 range. The bias current of 2.0 and 2.1 provides a time-averaged voltage response for all values of the applied magnetic flux. The transfer function for the bias current of 2.0 and 2.1 have different slopes in the flux range 0 to 0.5. The slope of the transfer function is a measurable figure of merit for the DC SQUID, and contributes to the magnetic sensitivity of the entire device [16]. The magnetic sensitivity is maximized by maximizing the transfer function slope. The bias current of 2.0 provides the greatest amount of slope with a voltage response for all applied magnetic flux values.

A three dimensional surface plot of the transfer function is shown in Figure 3.14 and visually shows the relationship between the transfer function, normalized bias current, and the normalized applied magnetic flux. The flat regions depict a zero time-averaged voltage across the DC SQUID. The zero voltage response is avoided because no information is provided for an applied magnetic flux. A numerical derivative of the transfer function is computed with respect to applied magnetic flux and is shown in Figure 3.15 as a surface plot. Maximum slope occurs at a bias current of 1.5, however this bias current value is un-useable because it contains zero-voltage response. The bias current of 2.0 provides the greatest amount of slope and has a voltage response for all applied magnetic flux values, thus this value is the minimum bias current value to be used for the DC SQUID.

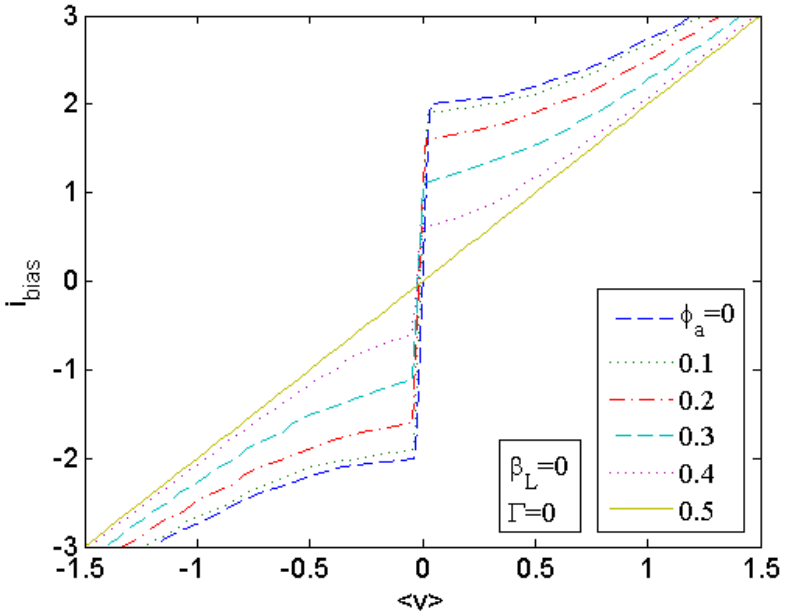

Figure 3.12: DC SQUID noise-free I-V electrical characteristic with the modulation parameter $\beta_L = 0$ at applied flux values 0, 0.1, 0.2, 0.3, 0.4, and 0.5

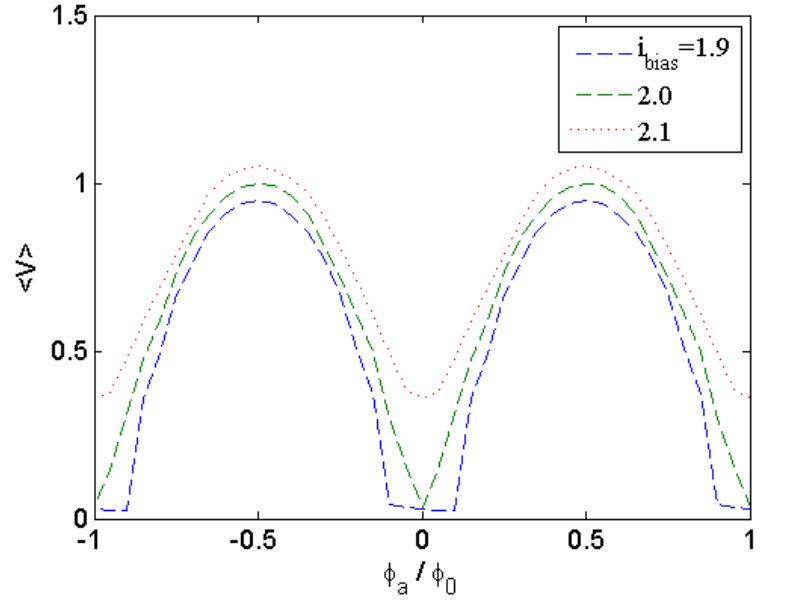

Figure 3.13: DC SQUID noise-free transfer function at bias currents 1.9, 2.0, and 2.1 over a span of applied flux values spanning -1 to 1 with the modulation parameter $\beta_L = 0$. There is a null voltage region for a 1.9 bias current, maximum slope and peak-to-peak voltage for a 2.0 bias current, and reduced slope and peak-to-peak voltage for a 2.1 bias current.

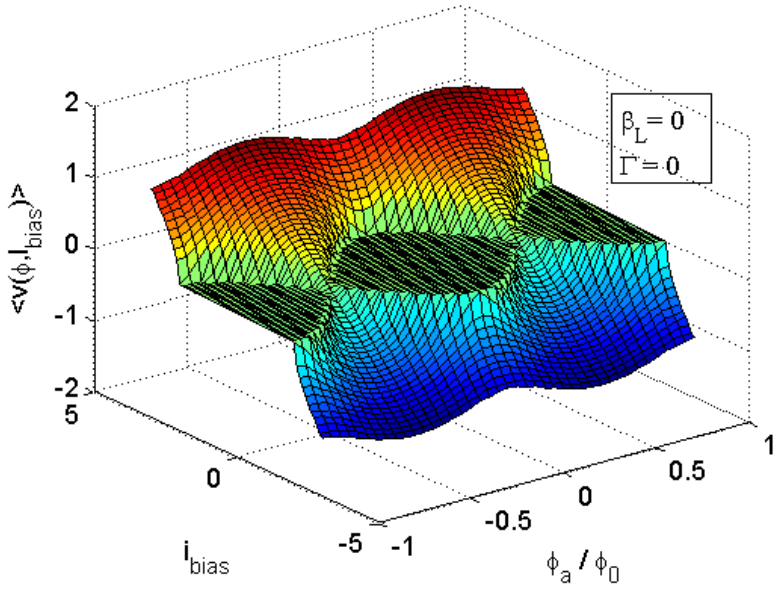

Figure 3.14: Surface plot of the DC SQUID noise-free transfer function with the modulation parameter $\beta_L = 0$. The flat regions depict zero voltage development across the DC SQUID and are avoided for operation.

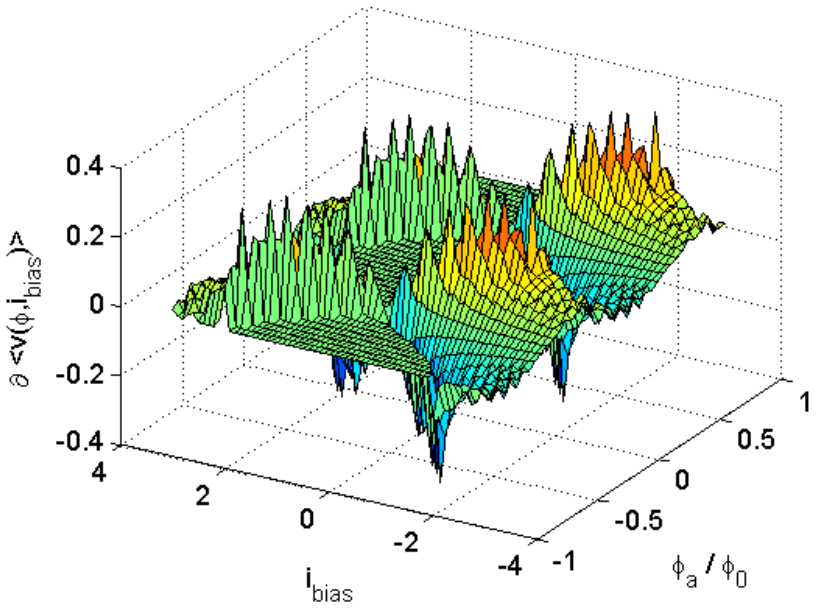

Figure 3.15: Surface plot of the transfer function derivative $\partial\langle v\rangle$ showing the regions of maximum slope with the modulation parameter $\beta_L = 0$. The maximum slope occurs around a bias current value of 1.5 however this bias current value is un-usable because it contains a null voltage region.

3.3.3.3 Noise-free Numerical Simulation with $\beta_L > 0$.

Non-zero values of the modulation parameter β_L requires a different numerical approach. The numerical computation for the two dimensional ODE model equation requires all of the unknown parameters δ_1, δ_2, and j to be stepped through sequentially during the solution computation. The I-V electrical operating characteristic is produced with a set of bias current values ranging from -3 to 3 for comparison with the data figures presented in [16] at the end of this section. Figure 3.16 shows the I-V electrical operating characteristic for the DC SQUID over the range of applied magnetic flux values 0, 0.1, 0.2, 0.3, 0.4, and 0.5.

Figure 3.17 shows the transfer function for $\beta_L = 1$. The transfer function is computed using normalized bias currents 1.9, 2.0, and 2.1 to show the time-averaged voltage at the 1.9, 2.0, and 2.1 bias current values. A small zero time-averaged voltage region is shown at a bias current of 1.9. This zero voltage region spans $0.1\phi_a$ and is does not provide information for applied magnetic flux values within the 0 to 0.1 range. The bias current of 2.0 and 2.1 provide a time-averaged voltage response for all values of applied magnetic flux. The bias currents for 2.0 and 2.1 produce transfer functions with different slope levels, with the bias current of 2.0 providing the largest slope level. The magnetic sensitivity of the DC SQUID is maximized by maximizing the transfer function slope.

Figure 3.18 shows the transfer function as a three dimensional surface plot. The flat regions depict a zero time-averaged voltage across the DC SQUID and are avoided because no information is provided for an applied magnetic flux. The modulation parameter $\beta_L = 1$ increases the amount of zero voltage response as seen from the expansion of the flat regions found in the $\beta = 0$ transfer function surface plot, Figure 3.14. A numerical derivative of the transfer function is computed with respect to the applied magnetic flux and is shown in Figure 3.19. Maximum slope occurs for a bias current of 1.5, however this bias current value is un-useable because it contains zero-voltage response. The bias current of 2.0

provides the greatest amount of slope and has a voltage response for all applied magnetic flux values.

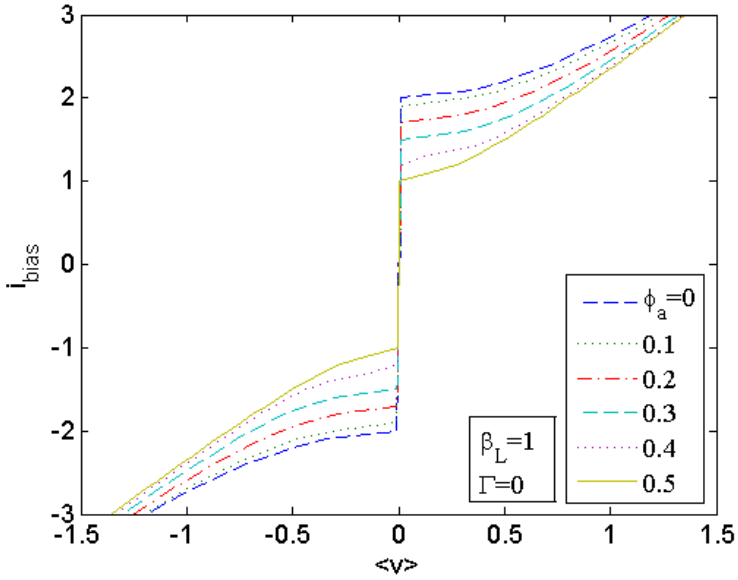

Figure 3.16: DC SQUID noise-free I-V electrical characteristic with the modulation parameter $\beta_L = 1$ at applied flux values 0, 0.1, 0.2, 0.3, 0.4, and 0.5

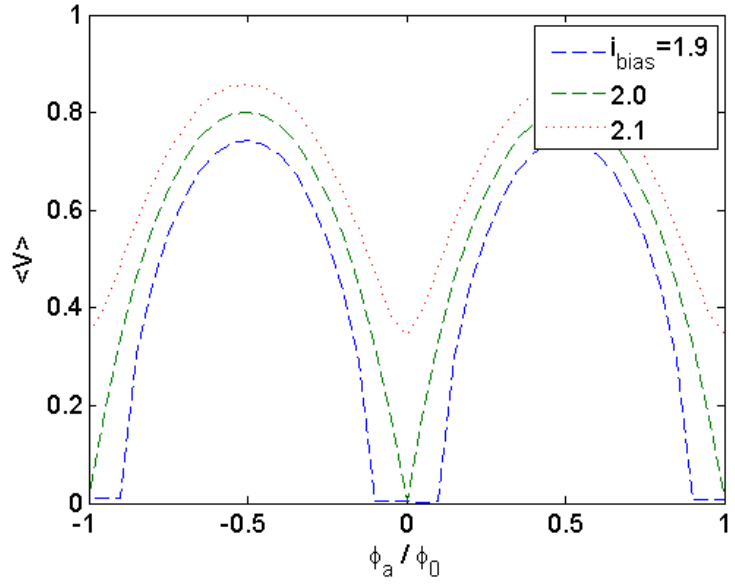

Figure 3.17: DC SQUID noise-free transfer function at bias currents 1.9, 2.0, and 2.1 over a span of applied flux values spanning -1 to 1 with the modulation parameter $\beta_L = 1$. There is a null voltage region for a 1.9 bias current, maximum slope and peak-to-peak voltage for a 2.0 bias current, and reduced slope and peak-to-peak voltage for a 2.1 bias current.

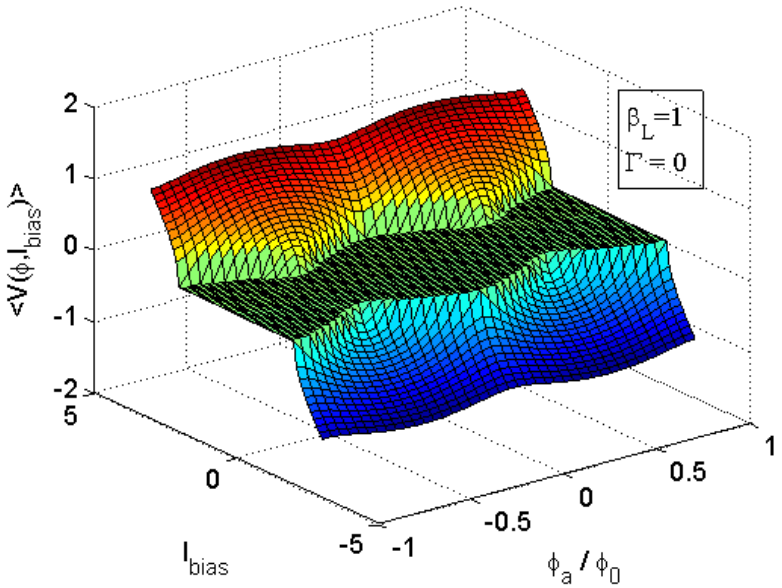

Figure 3.18: Surface plot of the DC SQUID noise-free transfer function with the modulation parameter $\beta_L = 1$. The flat regions depict zero voltage development across the DC SQUID and are avoided for operation.

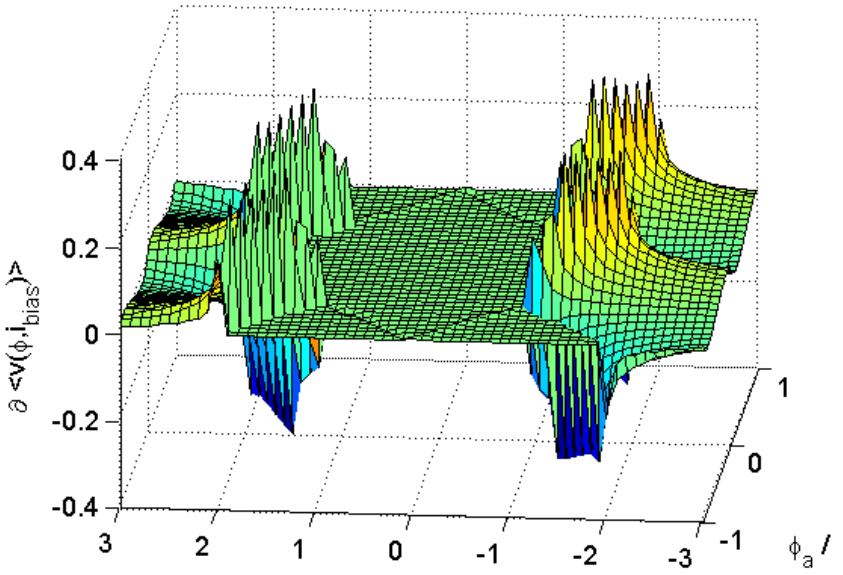

Figure 3.19: Surface plot of the transfer function derivative $\partial\langle v\rangle$ showing the regions of maximum slope with the modulation parameter $\beta_L = 1$. The maximum slope occurs around a bias current value of 1.5 however this bias current value is un-usable because it contains a null voltage region.

3.3.3.4 Thermal Noise Introduction.

The thermal noise current flowing in the junction is modeled as a current source with a noise spectral density of $S_i = 2\Gamma$. The thermal noise was seen to round the I-V characteristic curve for the Josephson junction and a similar result is expected for the DC SQUID. The I-V characteristics for the DC SQUID in the presence of thermal noise are shown in Figure 3.20. The I-V characteristic is computed with a noise power $\Gamma = 0.05$ over a range of bias currents and applied flux values to match the simulation conditions from [16] so that a comparison can be performed, shown at the end of the section.

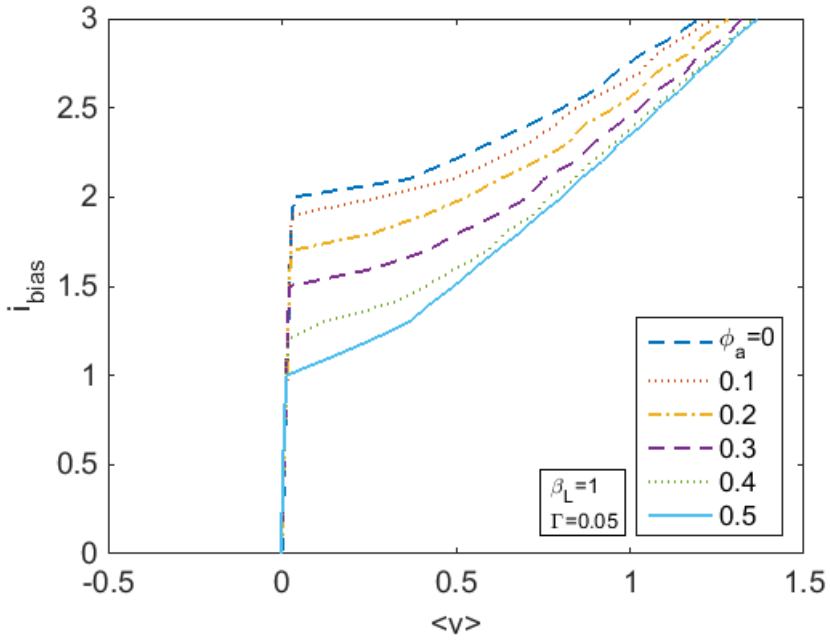

Figure 3.20: DC SQUID I-V electrical characteristics with thermal noise $\Gamma = 0.05$ using a modulation parameter of $\beta_L = 1$ at applied flux values 0, 0.1, 0.2, 0.3, 0.4, and 0.5.

The thermal noise slightly rounds the I-V characteristic at voltage values less than 0.25, in a result similar for the Josephson junction thermal noise simulations. Figure 3.21 shows the computed transfer function for the DC SQUID in the presence of thermal noise with a noise power $\Gamma = 0.05$. The transfer function is computed using a range of bias

current $\in \{1.5 \ldots 2.9\}$ to match the simulation conditions from [16] so that a comparison can be performed, shown at the end of the section.

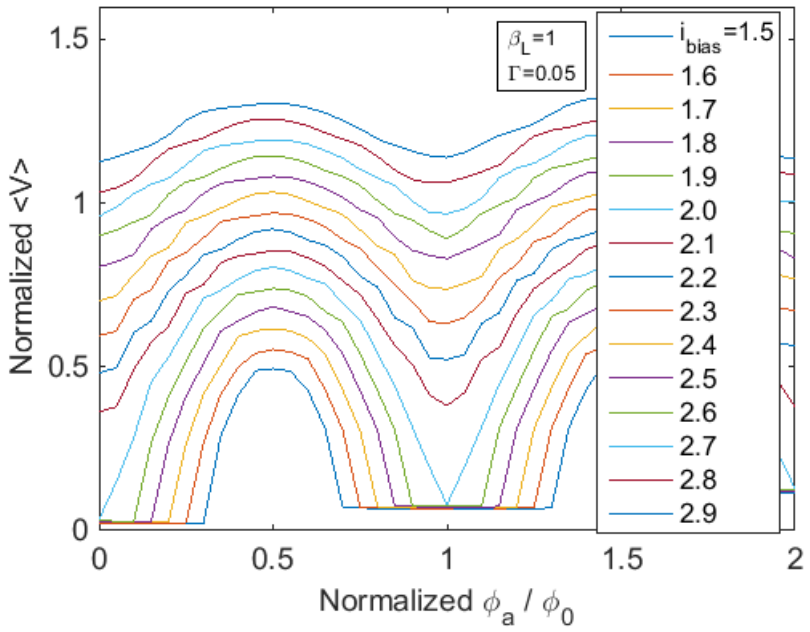

Figure 3.21: DC SQUID transfer function with thermal noise $\Gamma = 0.05$ using a modulation parameter of $\beta_L = 1$.

Figure 3.22 shows the surface plot of the transfer function, providing a visual representation showing the relationship of the transfer function with the bias current and applied magnetic flux values. Voltage fluctuations seen in the transfer function are caused by the addition of a thermal noise current. These voltage fluctuations are small in comparison to the peak to peak transfer function voltage response, as seen by the similar surface plot shapes for the transfer function contained in Figures 3.22 and 3.18.

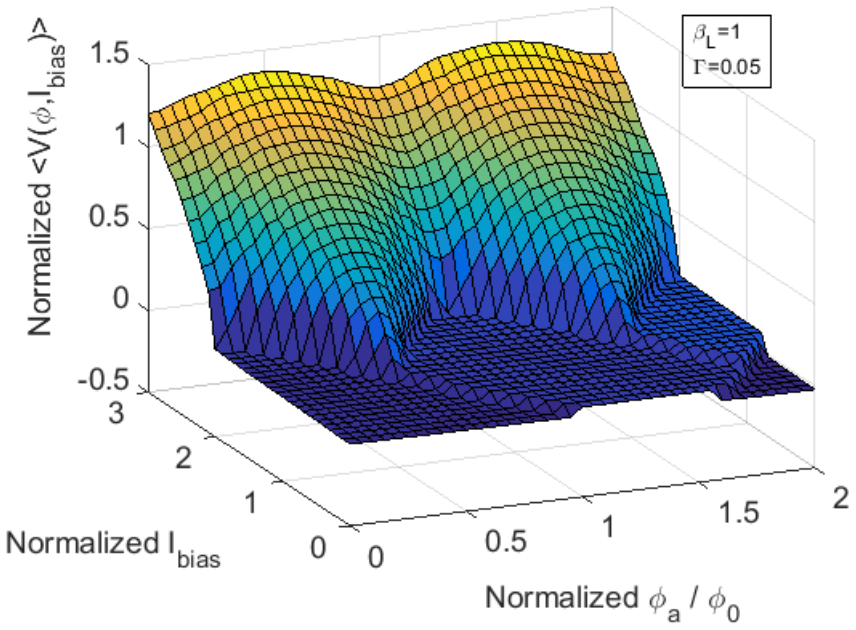

Figure 3.22: Surface plot of the DC SQUID transfer function with thermal noise Γ = 0.05. The flat regions depict zero voltage development across the DC SQUID.

3.3.4 Resistor-Capacitor-Shunted-Junction Model Implementation.

The screening parameter β_L contributes to two separate modeling equations for the DC SQUID, one for the case ($\beta_L = 0$) and the other for the case ($\beta_L > 0$). The value 0.04 is discovered to be the threshold driving which equation set is used for computing the numerical solution. β_L values less than 0.04 use the ($\beta_L = 0$) equation set, and values greater than 0.04 use the ($\beta_L > 0$) equation set. Solutions computed using the ($\beta_L = 0$) equation set with a β_L greater than 0.04 are inaccurate and unusable; also solutions computed using the ($\beta_L > 0$) equation set with a β_L less than 0.04 are inaccurate and unusable

3.3.5 Resistor-Capacitor-Shunted-Junction Model Verification.

The RKF-45 numerical solutions are compared to the data from [16] to check the computed solutions using the RKF-45 numerical method.

The comparison between the numerically computed noise-free I-V characteristics shown in Figure 3.24 and Figure 3.25 visually matche well with the noise-free I-V characteristic shown in Figure 3.23, taken from the data source [16]. The numerically computed noise-free transfer function shown in Figure 3.27 is compared with the noise-free transfer function from [16], shown as Figure 3.26, with the comparison showing the data matches, however a difference of 0.2 is seen between the noise-free transfer function data sets. This error is relatively small and is seen to scale all values of the transfer function, so it can be compensated with a scaling factor of 1.2. The thermal noise I-V characteristic is compared between the numerically produced data, shown in Figure 3.30 and the data from the source [16], shown as Figure 3.28. The thermal noise I-V characteristic data matches well for voltage values greater than 0.25, although the data sets differ for voltage values less than 0.25. Figure 3.28 shows that the data source I-V curve is rounded for voltage values less than 0.25, but this curvature is not well shown in the numerically produced thermal noise I-V characteristic in Figure 3.30. The thermal noise transfer function for numerically produced data in Figure 3.31 is compared with the data source transfer function in Figure 3.29, and the data values match well, however the waveform curvatures are slightly different. The transfer function in Figure 3.29 shows a smooth and curved transfer function produced by thermal noise. The transfer function for Figure 3.31 does not show the smoothly curved transfer function, but instead exhibits sharp voltage transitions. The transfer function data produced using RKF-45 numerical computation is still usable and the differences seen in comparison with the data source figures are minor. In conclusion, the RKF-45 produced solutions match the data figures contained in the data source [16], showing the RKF-45 method provides acceptable solutions.

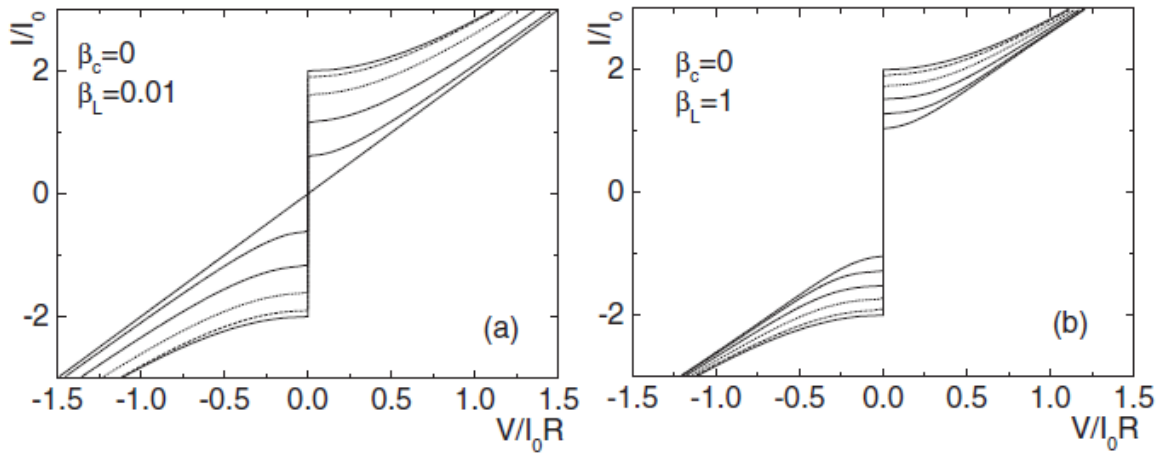

Figure 3.23: Fig. 2.8a and Fig. 2.8b taken from [16] for comparison with RKF-45 numerically produced I-V characteristic curves. Current voltage characteristics of the dc SQUIDs for β_L=0.01, 1. Applied flux is increased from 0 (solid line) to $\Phi_0/2$ (short dashed line) in steps of $0.1\Phi_0$.

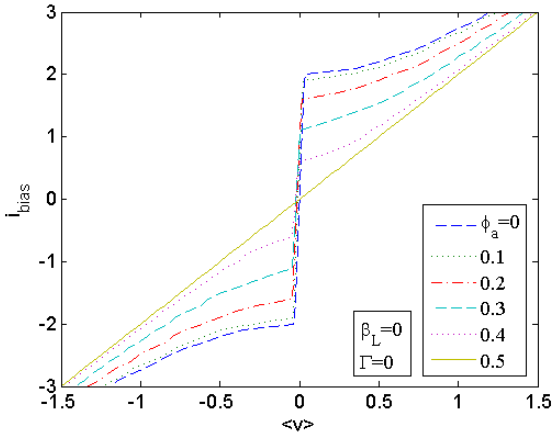

Figure 3.24: RKF-45 produced current voltage characteristics of the dc SQUID for β_L=0. The applied flux is increased from 0 to $\Phi_0/2$ in steps of $0.1\Phi_0$. The I-V characteristic visually matches the data presented in Figure 3.23

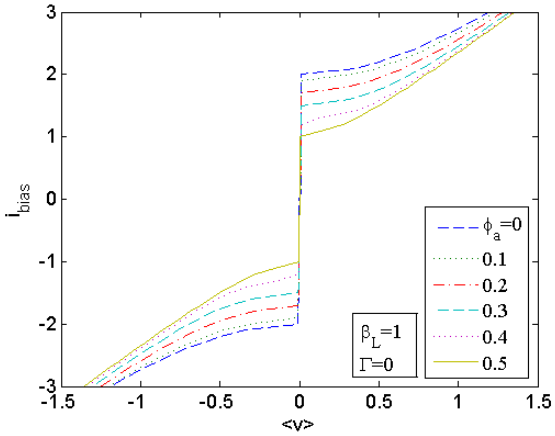

Figure 3.25: RKF-45 produced current voltage characteristics of the dc SQUID for β_L=1. The applied flux is increased from 0 to $\Phi_0/2$ in steps of $0.1\Phi_0$. The I-V characteristic visually matches the data presented in Figure 3.23

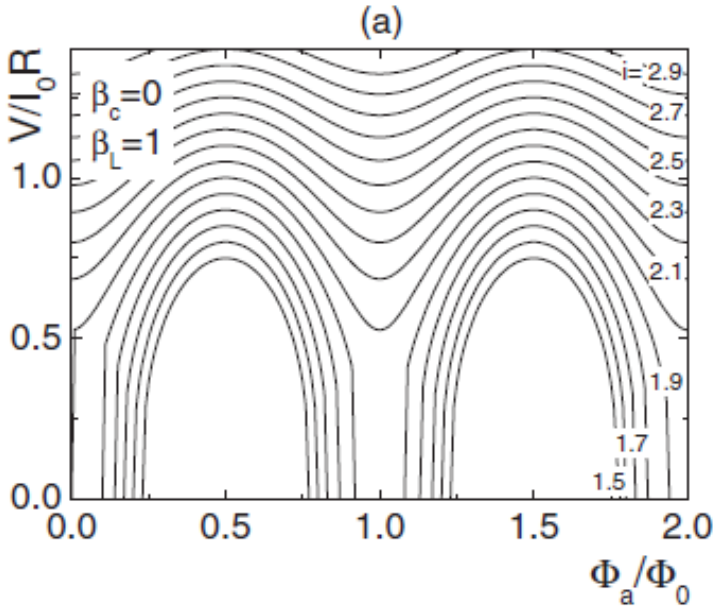

Figure 3.26: Fig. 2.9 taken from [16] for comparison with RKF-45 numerically produced transfer function. dc SQUID modulation $V(\Phi_a)$ for several values of normalized bias current i from 1.5 to 1.9 calculated for strongly overdamped junctions.

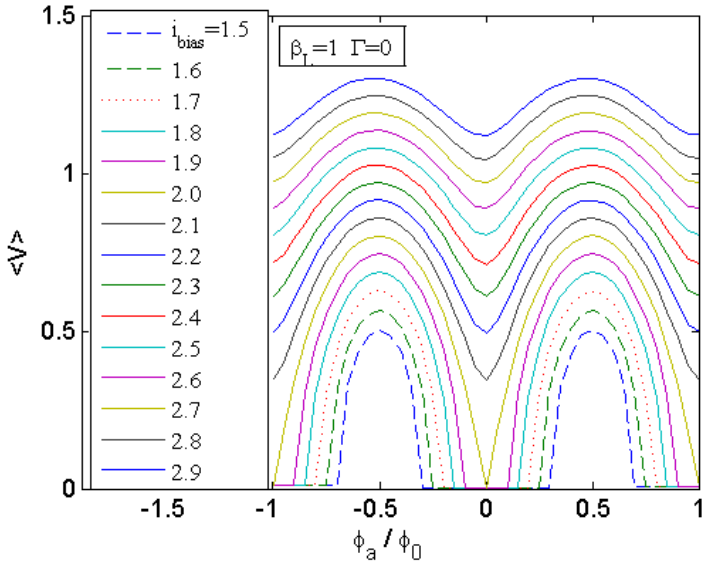

Figure 3.27: RKF-45 produced transfer function $\langle U(\Phi_a)\rangle$ for normalized bias current values from 1.5 to 1.9 with $\beta_L = 1$. The transfer function visually matches the data presented in Figure 3.26 although there is a slight discrepancy with the numerical values not matching, exhibiting an error of $\tilde{0}.2$.

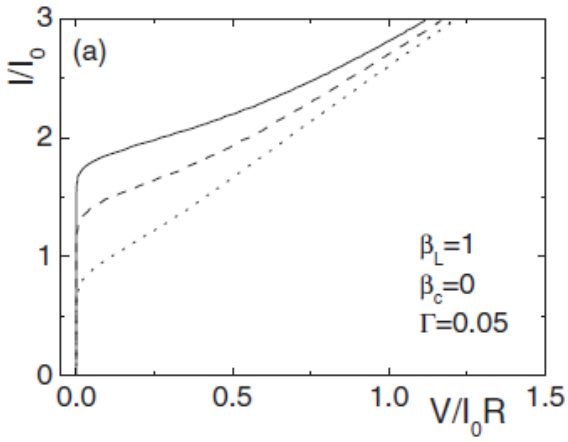

Figure 3.28: Fig. 2.13 taken from [16] for comparison with RKF-45 produced I-V characteristic with thermal noise. Current-voltage characteristics of dc SQUID with strongly overdamped junctions in the presence of thermal noise ($\Gamma = 0.05$).

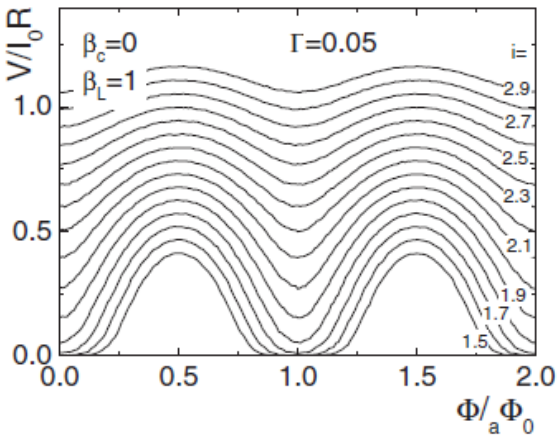

Figure 3.29: Fig. 2.14 taken from [16] for comparison with RKF-45 produced transfer function with thermal noise. Voltage modulation $V(\Phi_a)$ of dc SQUID for strongly dmaped junctions, in the presence of thermal noise for several values of bias current from 1.5 to 2.9.

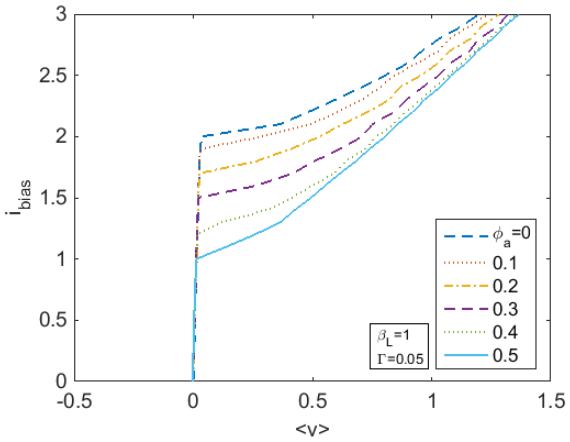

Figure 3.30: RKF-45 produced I-V characteristic curve with the presence of thermal noise $\Gamma = 0.05$ for $\beta_L = 1$. The I-V curve visually matches the data presented in Figure 3.28 for voltage values greater than 0.25. The I-V curve closely match for voltage values less than 0.25, however Figure 3.28 shows that noise rounds this portion of the I-V curve.

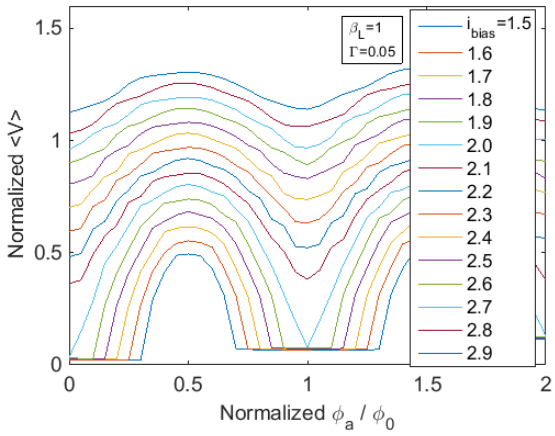

Figure 3.31: RKF-45 produced transfer function with the presence of themal noise $\Gamma = 0.05$ for $\beta_L = 1$. The transfer function closely matches the data presented in Figure 3.29, exhibiting an error ≤ 0.1. The edges of the transfer function from 3.29 are smoothed compared with the RKF-45 produced transfer function.

IV. Results

CHAPTER IV presents HF numerical simulations using the DC SQUID circuit model. A HF magnetic flux signal is applied to the DC SQUID circuit model to produce a DC SQUID voltage response. The DC SQUID develops a voltage in response to the applied HF magnetic flux signal, but it is necessary to compute a fast time-average to produce the final voltage waveform. The voltage samples produced with fast time-averaging shows a relationship with the Nyquist-Shannon sampling theorem. Simulations are performed for noise-free, junction thermal noise, and AWGN conditions to characterize the response of the DC SQUID for noise-free and noisy conditions. The HF sensitivity of the DC SQUID is examined using the Friis transmission equation and optical responsitivity metrics.

4.1 DC SQUID Electrical Parameters

The electrical parameters defining the DC SQUID are found using the process outlined in Figure 4.1. The DC SQUID inductance is derived from the physical architecture of the superconducting ring, and the capacitance of the Josephson junction is derived from the cross sectional area of the barrier architecture. Lithographic processes limit device

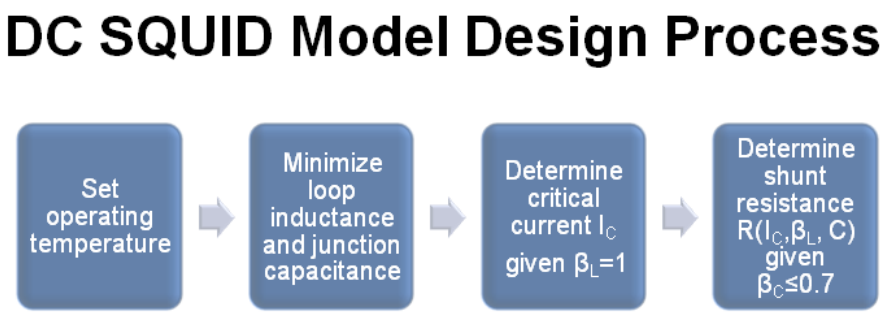

Figure 4.1: Design process for the DC SQUID

fabrication for achieving small loop structures and small Josephson junction barrier cross sectional areas. The inductance and capacitance for the DC SQUID architecture are used to compute the remaining DC SQUID parameters. The critical current I_C is computed using,

$$I_C = \frac{\beta_L \phi_0}{2L}\Big|_{\beta_L=1} = \frac{\phi_0}{2L} \tag{4.1}$$

with the condition $\beta_L = 1$ for maximum energy resolution [40]. The shunt resistance, R, is computed using the parameters I_C, C, with the condition $\beta_C \leq 0.7$ to avoid I-V characteristic hysteresis. The shunt resistance is found using,

$$\beta_C = \frac{2\pi}{\phi_0} I_C R^2 C\Big|_{I_C=\frac{\phi_0}{2L}} \leq 0.7 \tag{4.2}$$

$$R \leq \sqrt{\frac{0.7L}{\pi C}} \tag{4.3}$$

The electrical parameters for a representative low temperature DC SQUID are contained in Table 4.1 using an inductance of 1 nH and a capacitance of 1 pF.

Table 4.1: DC SQUID Design Parameters

Temperature T	Inductance L	Capacitance C	Critical Current I_C	Max Resistance
4.7K	1nH	1pF	1μA	15Ω

The β_C condition is satisfied for resistance values ranging from 0 to 15 Ω, so a resistance will need to be selected. Shunt resistance effects the peak voltage response and the characteristic frequency ω_C of the DC SQUID, and contains the trade space between voltage response and the oscillation frequency of the DC SQUID instantaneous voltage. Maximizing the voltage response will maximize the magnetic flux sensitivity, however this increases the oscillation frequency ω_C; ω_C must be low enough to allow electronic hardware to meet Nyquist sampling requirements. Figure 4.2 shows the surface plot of the voltage transfer function as a function of resistance.

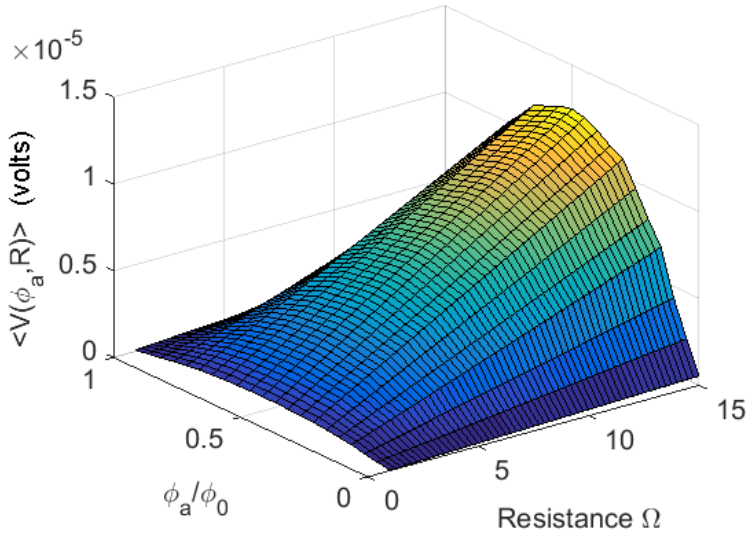

Figure 4.2: Surface plot showing the transfer function for values of resistance from 0 to 15 Ω. Increasing resistance increases the magnitude of the transfer function and corresponding the voltage response, however the oscillation frequency ω_C is also increased.

The transfer function is shown to be maximum at $R = 15\Omega$, although this produces an oscillation frequency of 45.6 GHz and far exceeds the fastest analog to digital converter available. Reducing the resistance to $R = 0.01\Omega$ produces an oscillation frequency of 3 MHz, however this minimizes the transfer function. The resistance is chosen to be $R = 10\Omega$ for this simulation to compromise between voltage response and oscillation frequency. The Stewart-McCumber damping parameter β_C and the characteristic frequency ω_C for $R = 10$ Ω are shown in Table 4.2.

Table 4.2: DC SQUID Circuit Parameters

Inductance L	Capacitance C	Resistance R	β_L	β_C	$\omega_C(\tau)$
1nH	1pF	10 Ω	1	0.3142	31.4 GHz

4.2 Application of a Time-Varying Magnetic Flux Signal

A time-varying magnetic flux signal $\varphi(t)$ of magnitude $|\varphi|$ and frequency f is applied using the DC SQUID circuit model to simulate the reception of HF EM energy. The applied magnetic flux signal is,

$$\varphi(t) = |\varphi| \sin(2\pi f t) \quad \text{webers (Wb)} \tag{4.4}$$

with magnitude $|\varphi|$, frequency f, and time t. The applied magnetic flux signal is normalized using the time relationship $\tau = \omega_C t$ for integration with the normalized DC SQUID model equations. With the τ relationship, the magnetic flux signal becomes

$$\varphi(\tau) = |\varphi| \sin(2\pi f \frac{\tau}{\omega_C}) = |\varphi| \sin(\frac{\omega}{\omega_C}\tau) \tag{4.5}$$

The DC SQUID voltage response is analyzed over the HF band using Equation 4.5.

4.2.1 Noise-free Numerical Simulation.

The DC SQUID voltage response is first analyzed for the noise-free condition for frequencies 3-30 MHz. A magnetic flux signal with amplitude $|\varphi| = 0.25\phi_0$ and a frequency of $f = 3$ MHz in input into the DC SQUID model to produce the DC SQUID voltage response. The magnitude $|\varphi| = 0.25\phi_0$ was chosen to remain inside the useful range for the DC SQUID transfer function $0 - 0.5\phi_0$, so that flux aliasing is avoided. The applied magnetic flux signal is shown in Figure 4.3. An instantaneous voltage $v(t)$ develops across the DC SQUID for the 3 MHz applied signal and is shown in Figure 4.4. The instantaneous DC SQUID voltage $v(t)$ that develops exhibits frequency and amplitude modulation characteristics shown by the frequency oscillations and the amplitude envelope for $v(t)$. Frequency modulation is caused by the amount of magnetic flux sensed by the DC SQUID and the amplitude modulation is caused by the applied signal amplitude envelope.

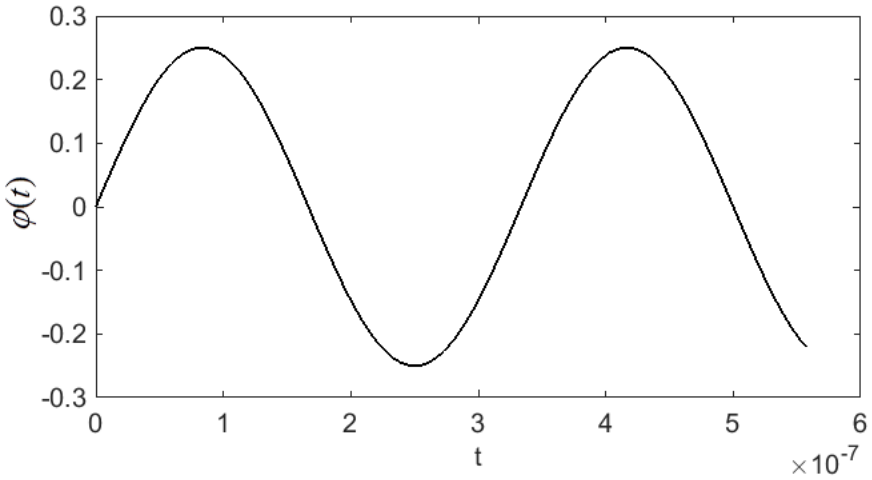

Figure 4.3: Applied magnetic flux signal $\varphi(t)$ with $f = 3$ MHz and $|\varphi| = 0.25\phi_0$ Wb.

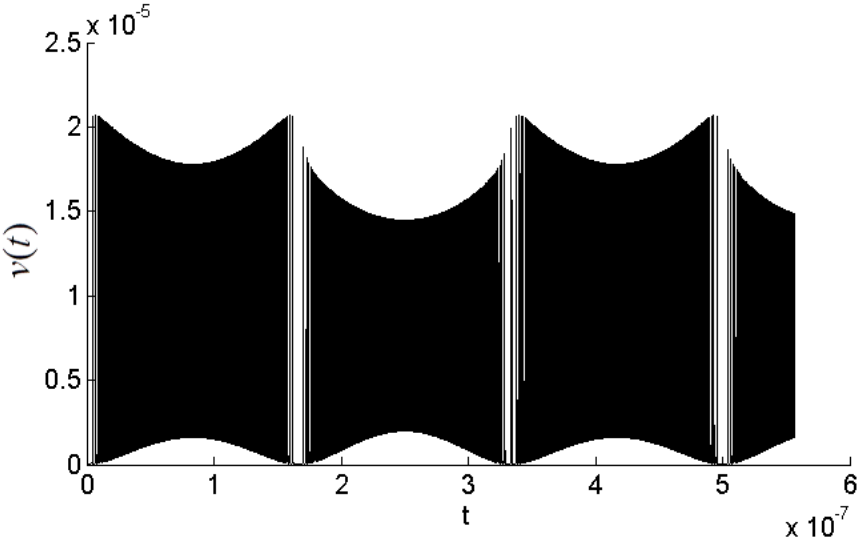

Figure 4.4: DC SQUID instantaneous voltage $v(t)$ for an applied magnetic flux signal with f=3 MHz and $|\varphi| = 0.25\phi_0$ Wb. Frequency modulation characteristics are shown by the frequency oscillations within $v(t)$ caused by the changing applied magnetic flux amplitude. Amplitude modulation characteristics are shown by the amplitude envelop of $v(t)$ and caused by the amplitude envelop of the applied magnetic flux signal $\varphi(t)$.

A fast time-average of the instantaneous DC SQUID voltage is computed with,

$$\langle v \rangle\Big|_{\Delta t} = \frac{1}{\Delta t} \sum_{\Delta t} v(t) \tag{4.6}$$

for instantaneous DC SQUID voltage $v(t)$ over the time interval Δt. The time interval Δt is chosen to meet the minimum Nyquist-Shannon sampling interval such that the sampling time interval must be less than half of the period of one cycle. For 3 MHz, the minimum time interval is $\Delta t = 0.167 \mu S$. The fast time-averaging produces an output voltage waveform with sample points appearing at $4.7 \mu V$ with a spacing of 0.167 μS as shown in Figure 4.5.

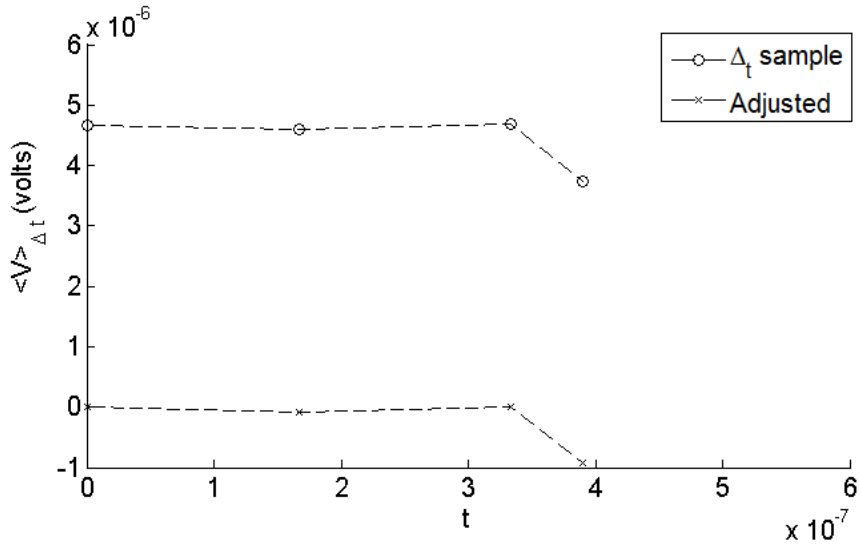

Figure 4.5: Voltage samples produced with a fast time-average of $v(t)$ for a time interval $\Delta t = 0.167 \mu S$, producing 2 sample per cycle. A bias offset of $4.7 \mu V$ is removed to shift the voltage samples to zero, allowing for an accurate sample representation of the 3 MHz magnetic flux signal $\varphi(t)$.

Fast time averaging produces a voltage signal with samples appearing at the time locations corresponding with a sampled $\varphi(t)$ using a $\Delta t = 0.167 \mu S$ sampling period, indicating that fast time averaging produces sample points of the applied magnetic flux signal at a $4.7 \mu V$ bias offset. The bias offset is removed to shift the voltage samples to

zero for an accurate sampling representation of the 3 MHz applied magnetic flux signal. The last data point in the fast time-averaged voltage waveform is an erroneous result of an incomplete time-average over the time interval Δt. The time interval is reduced to 27.8 nS to produce 12 voltage samples per cycle to allow the fast time-averaged waveform to be analyzed, shown in Figure 4.6.

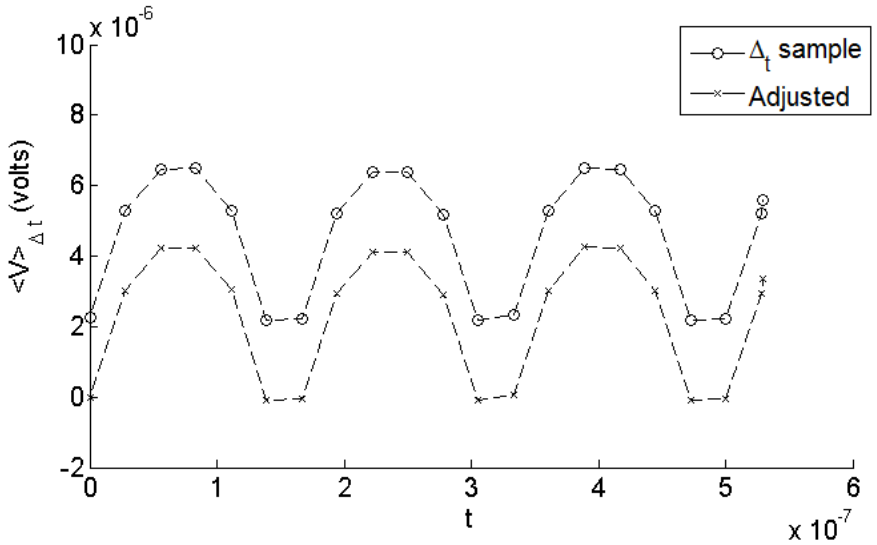

Figure 4.6: Voltage samples produced with a fast time-average of $v(t)$ for a time interval Δt = 27.8 nS, producing 12 voltage samples per cycle. A bias offset of 4.7μV is removed to shift the voltage samples to zero, allowing for an accurate sample representation of the 3 MHz magnetic flux signal $\varphi(t)$. The peak-to-peak voltage is 4.1μV.

The 12 sample per cycle voltage waveform contains a 2.3μV bias that is removed to shift the sample points to zero, allowing for an accurate sampling representation of the 3 MHz applied magnetic flux signal. A periodicity equal to $\frac{1}{2}$ of the applied magnetic flux signal is seen in the fast time averaged voltage waveform. The fast time averaged voltage waveform is seen to not contain negative voltage values, indicating that the DC SQUID operates as a voltage rectifier, since the negative cycles become positive. A peak to peak voltage of 4.1μV is observed, and also a null voltage region develops between each half cycle, however, the periodicity is still maintained.

A magnetic flux signal with $f = 15$ MHz is applied to the DC SQUID model to examine the DC SQUID voltage response. The applied magnetic flux signal is shown in Figure 4.7. The DC SQUID produces a voltage $v(t)$ in response to the $f = 15$ MHz applied magnetic flux signal and is shown in Figure 4.8.

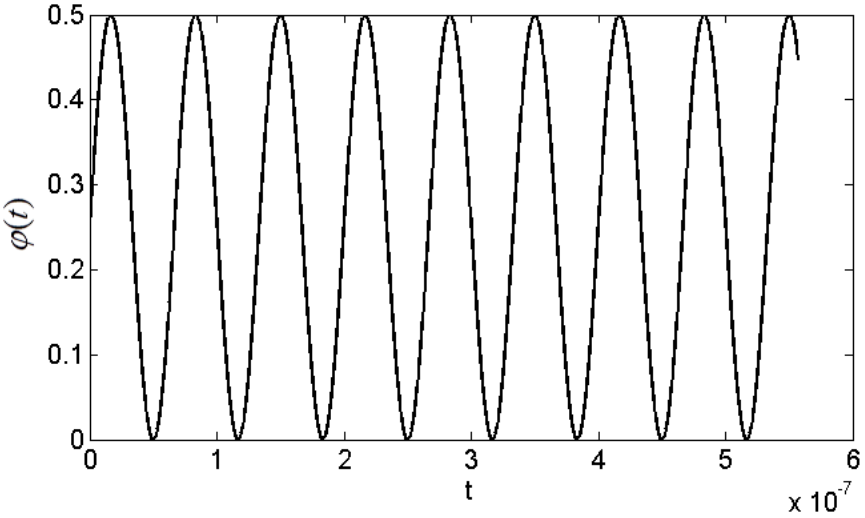

Figure 4.7: Applied magnetic flux signal $\varphi(t)$ with $|\varphi| = 0.25\phi_0$ Wb and $f = 15$ MHz.

An instantaneous voltage $v(t)$ develops across the DC SQUID for the 15 MHz applied magnetic flux signal. The DC SQUID voltage $v(t)$ exhibits the same frequency and amplitude modulation characteristics previous observed for the DC SQUID voltage response with an applied magnetic flux signal at $f = 3$ MHz.

A fast time-average is computed using $\Delta t = 33.3$ nS to produce 2 voltage samples per cycle at 15 MHz. The fast time averaged voltage samples appear at $4.7\mu V$ with a spacing of 33.3 nS as shown in Figure 4.9. The voltage samples appear at the time locations corresponding with a sampled $\varphi(t)$ using a $\Delta t = 33.3$ nS, indicating that fast time averaging produces voltage samples of the 15 MHz applied magnetic flux signal, with a $4.7\mu V$ bias offset.

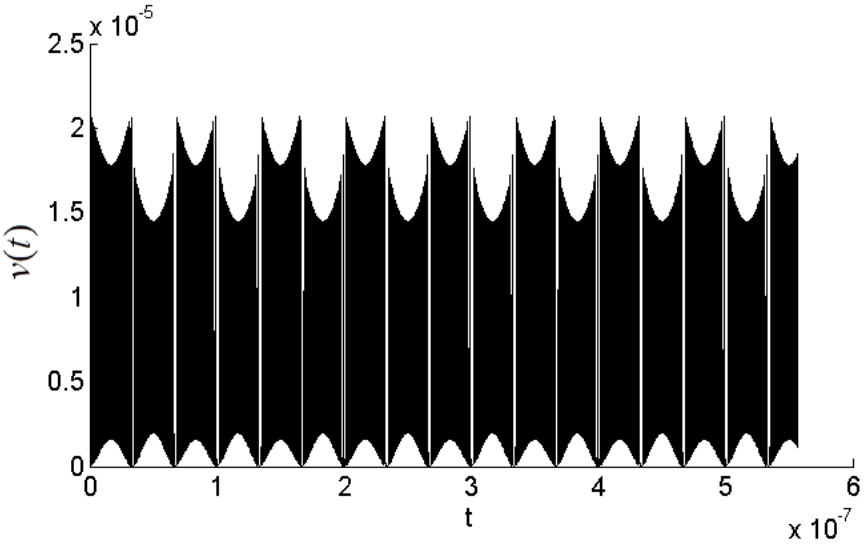

Figure 4.8: DC SQUID instantaneous voltage with f=15 MHz and $|\varphi| = 0.25\phi_0$ Wb applied magnetic flux. Frequency modulation characteristics are shown by the frequency oscillations within $v(t)$ caused by the changing applied magnetic flux amplitude. Amplitude modulation characteristics are shown by the amplitude envelop of $v(t)$ and caused by the amplitude envelop of the applied magnetic flux signal φ.

The bias offset is removed to shift the voltage samples to zero for an accurate sampling representation of the 15 MHz applied magnetic flux signal. The last data point in the fast time-averaged voltage waveform is an erroneous result of an incomplete time-average over the time interval Δt. The time interval is reduced to 5.6 nS to produce 12 voltage samples per cycle, allowing analysis of the fast time-averaged voltage waveform for an increased sample resolution, shown in Figure 4.10. The 12 sample per cycle voltage waveform contains a $2.2\mu V$ bias and is removed to shift the sample points to zero, allowing for an accurate sampling representation of the 15 MHz applied magnetic flux signal. A periodicity equal to $\frac{1}{2}$ of the applied magnetic flux signal is seen in the fast time averaged voltage waveform. The fast time averaged voltage waveform exhibits the voltage rectification response previously observed. A peak to peak voltage of $4.3\mu V$ develops, along with a null voltage region developing between each half cycle, however, the periodicity is still maintained.

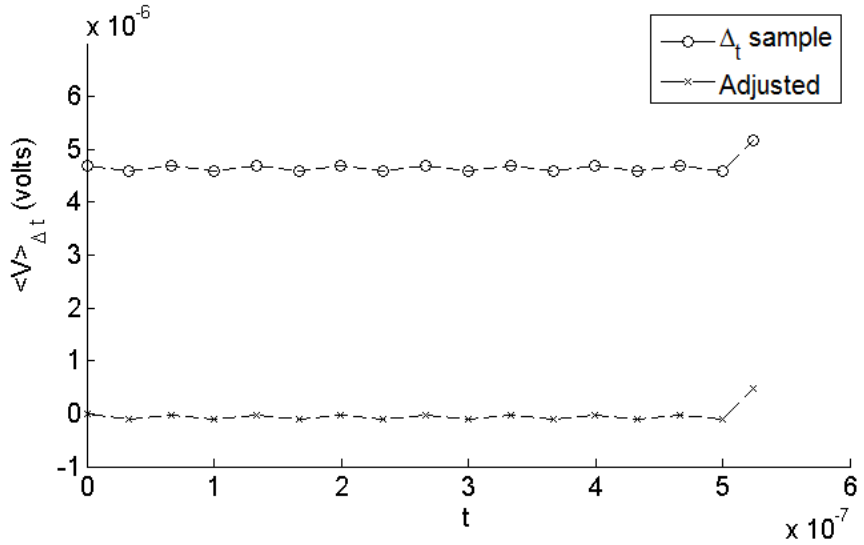

Figure 4.9: Voltage samples produced with a fast time-average of $v(t)$ for a time interval Δt = 33.3 nS, producing 12 voltage samples per cycle. A bias offset of 4.7μV is removed to shift the voltage samples to zero, allowing for an accurate sample representation of the 15 MHz magnetic flux signal $\varphi(t)$.

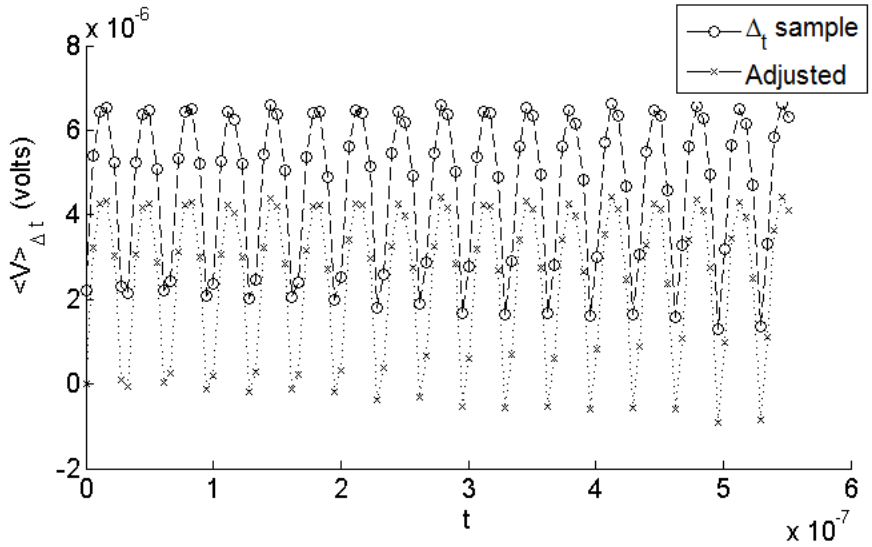

Figure 4.10: Voltage samples produced with a fast time-average of $v(t)$ for a time interval Δt = 5.6 nS, producing 12 voltage samples per cycle. A bias offset of 2.2μV is removed to shift the voltage samples to zero, allowing for an accurate sample representation of the 15 MHz magnetic flux signal $\varphi(t)$. The peak-to-peak voltage is 4.3μV.

A magnetic flux signal with $f = 30$ MHz is applied to the DC SQUID model to examine the DC SQUID voltage response. The applied magnetic flux signal is shown in Figure 4.11. The DC SQUID produces a voltage $v(t)$ for the $f = 30$ MHz applied magnetic flux signal and is shown in Figure 4.12.

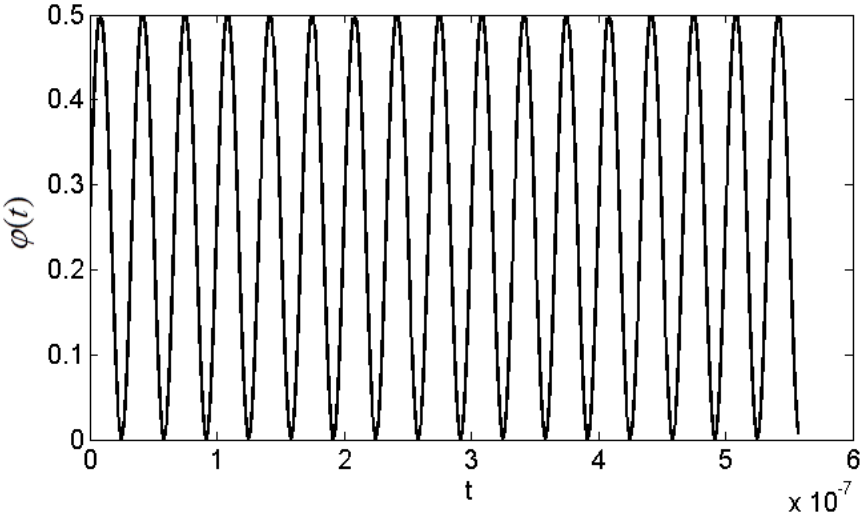

Figure 4.11: Applied magnetic flux signal with f=30 MHz and $|\varphi| = 0.25\phi_0$ Wb.

The instantaneous DC SQUID voltage $v(t)$ developing for an applied magnetic flux signal at $f = 30$ MHz exhibits the same frequency and amplitude modulation characteristics previous observed for the DC SQUID voltage response with an applied magnetic flux signal at $f = 3$ and 15 MHz.

A fast time-average is computed using $\Delta t = 16.7$ nS to produce 2 voltage samples per cycle. The fast time averaged voltage samples appear at $4.7\mu V$ with a spacing of 16.7 nS, as shown in Figure 4.9. The voltage samples appear at the time locations corresponding with a sampled $\varphi(t)$ using a $\Delta t = 16.7$ nS sampling period, indicating that fast time averaging produces voltage samples of the 30 MHz applied magnetic flux signal with a $4.7\mu V$ bias offset.

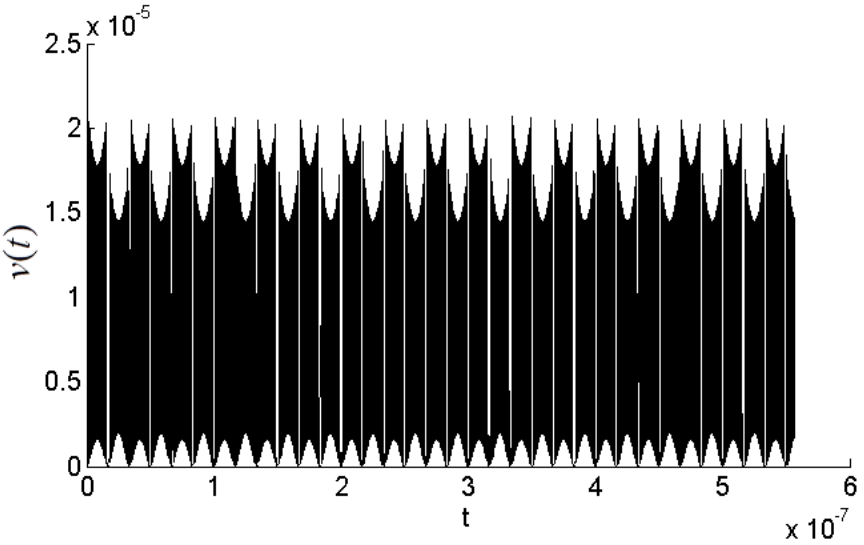

Figure 4.12: DC SQUID instantaneous voltage with f=30 MHz and $|\varphi| = 0.25\phi_0$ Wb applied magnetic flux. Frequency modulation characteristics are shown by the frequency oscillations within $v(t)$ caused by the changing applied magnetic flux amplitude. Amplitude modulation characteristics are shown by the amplitude envelop of $v(t)$ and caused by the amplitude envelop of the applied magnetic flux signal $\varphi(t)$.

The bias offset is removed to shift the voltage samples to zero for an accurate sampling representation of the 30 MHz applied magnetic flux signal. The last data point in the fast time-averaged voltage waveform is an erroneous result of an incomplete time-average over the time interval Δt. The time interval is reduced to 2.7 nS to produce 12 voltage samples per cycle, allowing analysis of fast time-averaged waveform with an increased sampling resolution, shown in Figure 4.14. The 12 sample per cycle voltage waveform contains a $2.3\mu V$ bias and is removed to shift the sample points to zero, allowing for an accurate sampling representation of the 30 MHz applied magnetic flux signal. A periodicity equal to $\frac{1}{2}$ of the applied magnetic flux signal is seen in the fast time averaged voltage waveform. The fast time averaged voltage waveform exhibits the voltage rectification response seen previously. A peak to peak voltage of $4.1\mu V$ is observed, and also a null voltage region is seen to develop between every half cycle, however, the periodicity is still maintained.

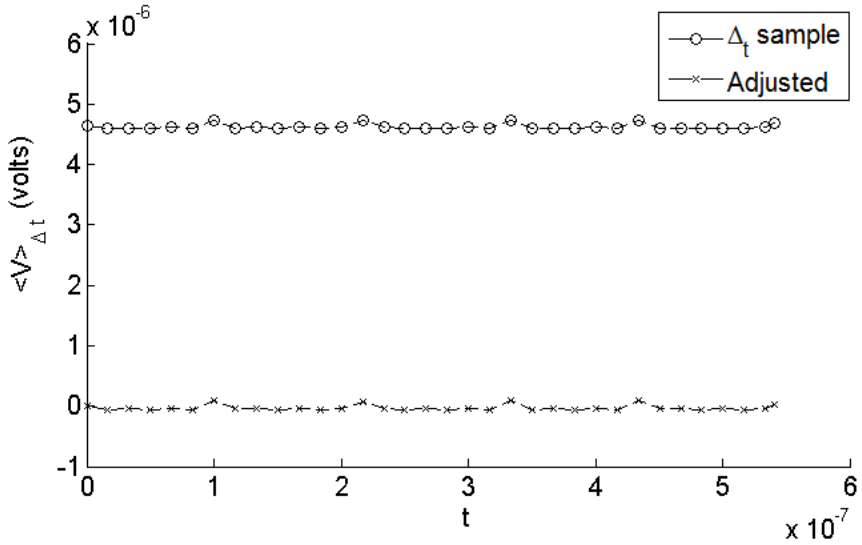

Figure 4.13: Voltage samples produced with a fast time-average of $v(t)$ for a time interval Δt = 16.7 nS, producing 2 voltage samples per cycle for a 30 MHz signal. A bias offset of 4.7μV is removed to shift the voltage samples to zero, allowing for an accurate sample representation for the 30 MHz magnetic flux signal.

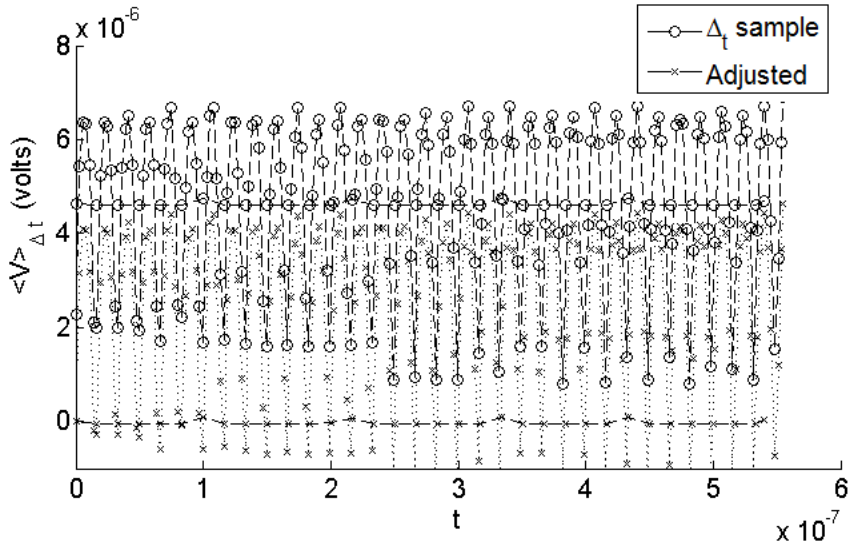

Figure 4.14: Voltage samples produced with a fast time-average of $v(t)$ for a time interval Δt = 2.7 nS, producing 12 voltage samples per cycle. A bias offset of 2.3μV is removed to shift the voltage samples to zero, allowing for an accurate sample representation of the 30 MHz magnetic flux signal. The peak-to-peak voltage is 4.1μV.

The DC SQUID voltage response over the HF band is shown in Figure 4.15. The peak to peak voltage is computed with the fast time averaged voltage waveform produced at 12 voltage samples per cycle. Frequencies from the HF band are used to compute the peak to peak voltage response of the DC SQUID. The resulting DC SQUID voltage response shows a stable trend across the HF band. A resonance not appearing within the HF band is an indication that this device has large bandwidth.

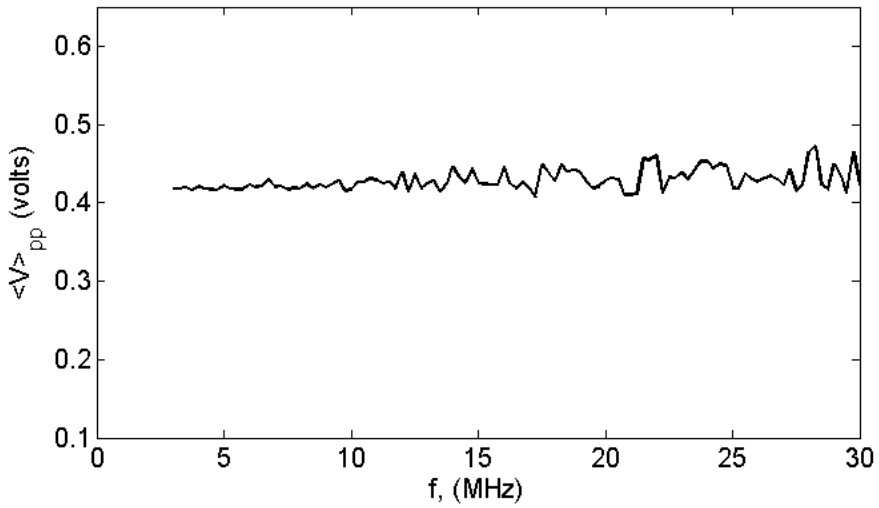

Figure 4.15: Peak to peak voltage response using the 12 voltage sample per cycle for the DC SQUID over the HF band. The peak to peak voltage remains constant over the HF band indicating the device is wide bandwidth.

4.2.2 Thermal Noise Numerical Simulation.

Thermal noise is introduced by adding an additional current source into the RCSJ circuit representation. The DC SQUID electrical parameters from Table 4.2 and Equation 3.16 are used to compute the noise current spectral density, found to be $S_I(f) = 0.76$ A/Hz. The noise current is modeled in the time domain as an AWGN random process with a noise power of 0.76 A over a bandwidth of 1 Hz. The DC SQUID voltage is computed with the random AWGN current. A time-varying magnetic flux signal with amplitude $|\varphi| = 0.25\phi_0$

and frequency $f = 3$ MHz is input into the model to produce the DC SQUID instantaneous voltage signal. The applied magnetic flux signal is shown in Figure 4.16(a). Noise is observed in the resulting instantaneous DC SQUID voltage $v(t)$ because of the additional thermal noise current, shown in Figure 4.16(b).

A fast time-average using a time interval of $\Delta t = 0.167\mu S$ produces voltage samples at $6.3\mu V$ spaced every $0.167\mu S$, representing a 2 sample per cycle sampling rate of the applied magnetic flux signal is shown in Figure 4.16(c). The $6.3\mu V$ bias offset is removed to shift the voltage samples to zero, showing that the voltage samples accurately represent the applied magnetic flux signal at the minimum Nyquist sampling rate.

A fast time-average using a time interval of $\Delta t = 27.8$nS produces voltage samples spaced every 27.8nS, representing a 12 sample per cycle sampling rate of the applied magnetic flux signal is shown in Figure 4.17. A $5.3\mu V$ bias offset voltage is removed, shifting the voltage samples to zero. Periodicity is observed and remains equal to $\frac{1}{2}$ the period of the applied magnetic flux signal. The voltage rectification response and the development of the null voltage region characteristics observed in the noise-free case still remain and are uninfluenced by the addition of thermal noise. The peak to peak voltage is $1.8\mu V$ is shown in the fast time average produced voltage waveform as shown in Figure 4.17.

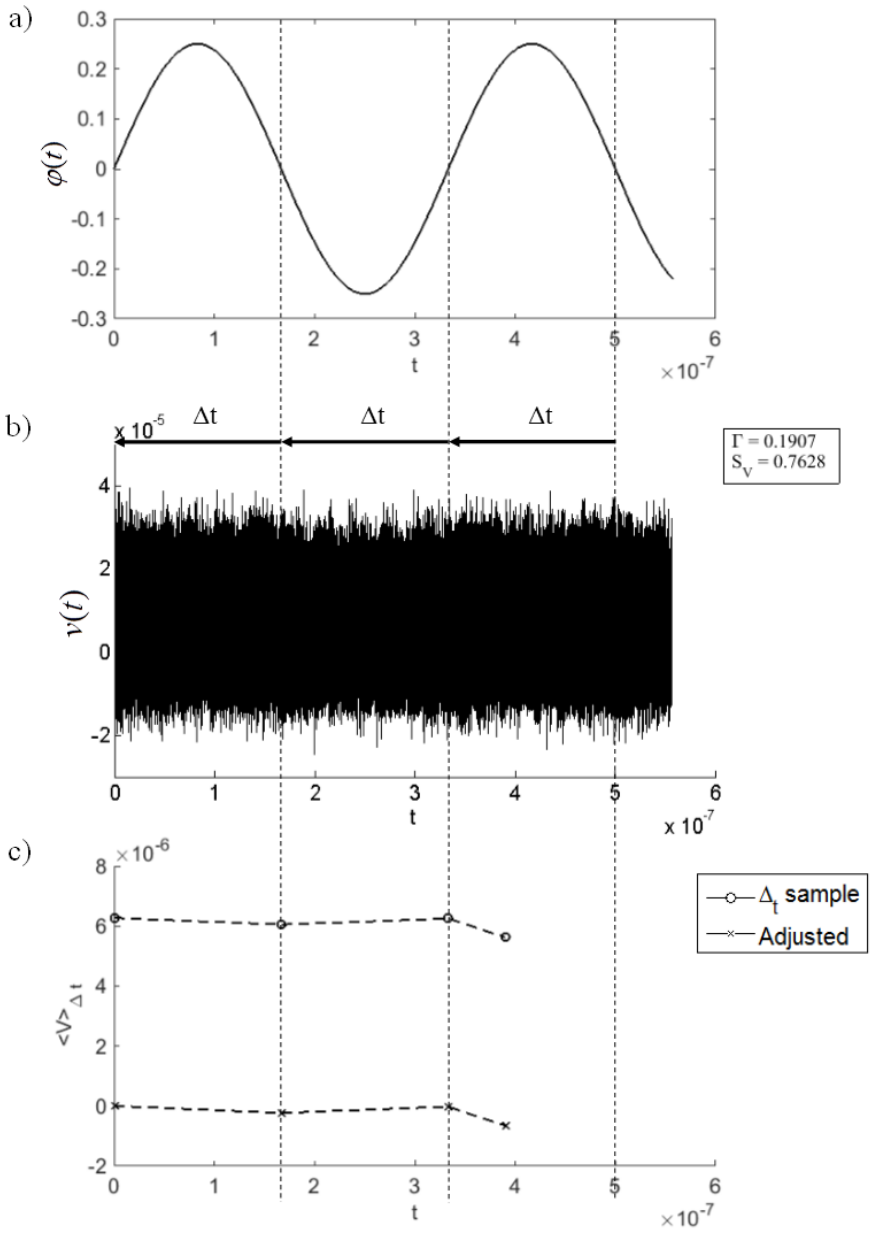

Figure 4.16: (a) Applied magnetic flux signal with $f = 3$ MHz and $|\varphi| = 0.25\phi_0$ Wb. (b) DC SQUID instantaneous voltage $v(t)$ develops in response to the applied magnetic flux signal. (c) Voltage samples with $6.3\mu V$ bias produced with a fast time-average of $v(t)$ for a time interval $\Delta t = 0.167\mu S$. $6.3\mu V$ bias is removed to shift the voltage samples to zero, allowing for an accurate sample representation for the 3 MHz applied magnetic flux signal $\varphi(t)$.

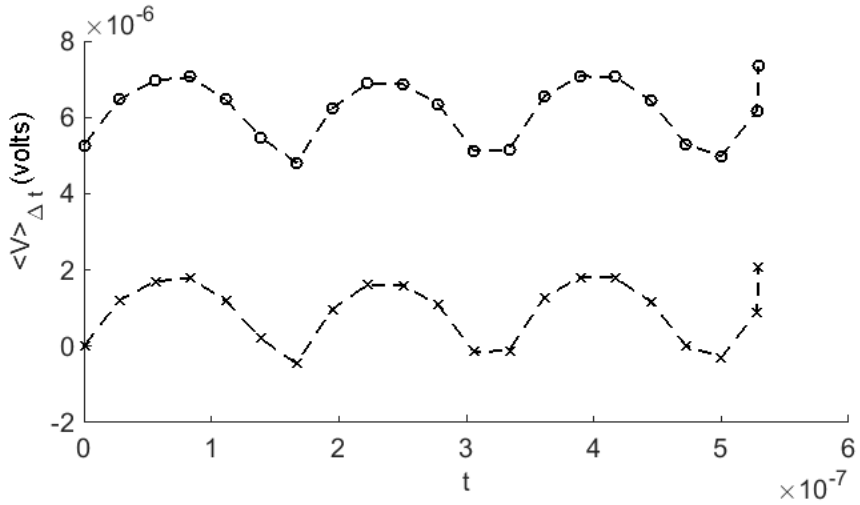

Figure 4.17: DC SQUID instantaneous voltage with f=3 MHz and $|\varphi| = 0.25\phi_0$ Wb applied magnetic flux. DC SQUID time-average is performed at 12 samples per cycle.

The remaining frequencies simulated for the HF band show the general characteristic of voltage rectification and the development of the null voltage region at the end of each cycle reconstruction. Additional simulations for selected frequency values 15 MHz and 30 MHz can be found in Appendix A. The DC SQUID voltage response with thermal noise over the HF band is shown in Figure 4.18. The peak to peak voltage is computed with fast time averaging at a time interval producing 12 voltage samples per cycle to construct the data shown in Figure 4.18. The frequencies from the HF band are used to compute the peak to peak voltage V_{pp} response of the DC SQUID. A stable peak to peak voltage trend is shown from the computed V_{pp} data. A resonance not appearing within the HF band is an indication that the DC SQUID has a large bandwidth. The peak to peak voltage response is reduced by half in comparison with the peak to peak voltage response from the noise free simulations, leading to the conclusion that the addition of the thermal noise current dramatically reduces the DC SQUID voltage response.

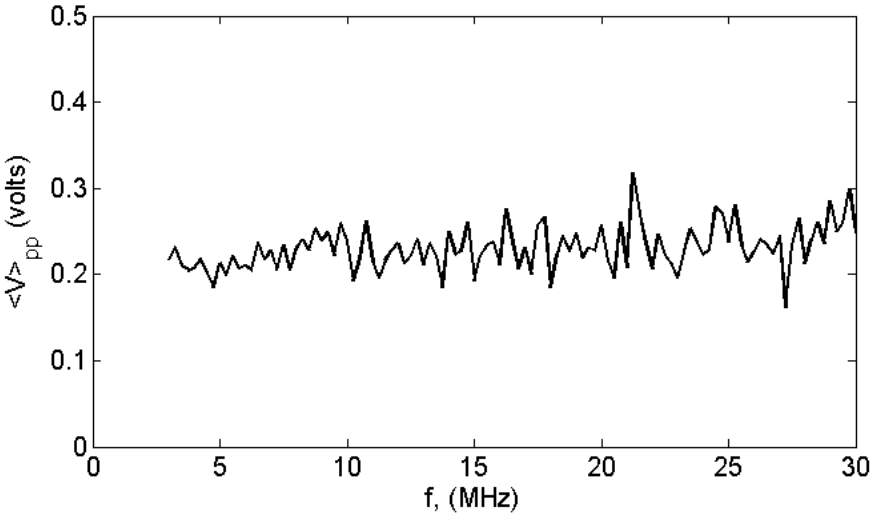

Figure 4.18: Peak to peak voltage response using the 12 voltage sample per cycle for the DC SQUID over the HF band. The peak to peak voltage remains constant over the HF band indicating the device is wide bandwidth.

4.2.3 Applied Magnetic Flux with AWGN Numerical Simulation.

The DC SQUID voltage response is examined for the introduction of 10dB of AWGN added to the applied magnetic flux signal. DC SQUID thermal noise with noise power of 0.76 A over a bandwidth of 1 Hz remains present for the simulations. A time-varying magnetic flux signal with amplitude $|\varphi| = 0.25\phi_0$ and frequency $f = 3$ MHz is input into the model to produce the DC SQUID instantaneous voltage signal $v(t)$. The applied magnetic flux signal is shown in Figure 4.19(a). The resulting instantaneous DC SQUID voltage $v(t)$ contains noise because of the thermal noise current, shown in Figure 4.19(b). The voltage amplitude in $v(t)$ did not increase with the addition of extra noise.

A fast time-average using a time interval of $\Delta t = 0.167\mu S$ produces voltage samples at $6.1\mu V$ spaced every $0.167\mu S$, representing a 2 sample per cycle sampling rate of the applied magnetic flux signal is shown in Figure 4.19(c). The $6.1\mu V$ bias offset is removed to shift the voltage samples to zero, showing that the voltage samples accurately represent the applied magnetic flux signal at the minimum Nyquist sampling rate.

A fast time-average using a time interval of $\Delta t = 27.8$nS produces voltage samples spaced every 27.8nS, representing a 12 sample per cycle sampling rate of the applied magnetic flux signal is shown in Figure 4.20. A $5\mu V$ bias offset voltage is removed, shifting the voltage samples to zero. Periodicity is observed and remains equal to $\frac{1}{2}$ the period of the applied magnetic flux signal. Voltage rectification and the null voltage region characteristics remain in the produced voltage samples. The peak to peak voltage is $2.2\mu V$ seen in the voltage samples in Figure 4.20.

The DFT quantifies the spectral content contained within a waveform and is used to perform a spectral analysis of the instantaneous DC SQUID voltage $v(t)$, shown in Figure 4.21. The majority of the spectral content is shown to be contained within the 2-4 GHz band and is unclear why this spectral content lies within this particular band. The remaining spectral energy is nearly constant and represents the noise floor. The DFT is computed with 12 voltage sample per cycle waveform, and is shown in Figure 4.22. The main spectral content is centered at 6 MHz, as expected because the waveform is seen to reduce the period by $\frac{1}{2}$, increasing the frequency by 2.

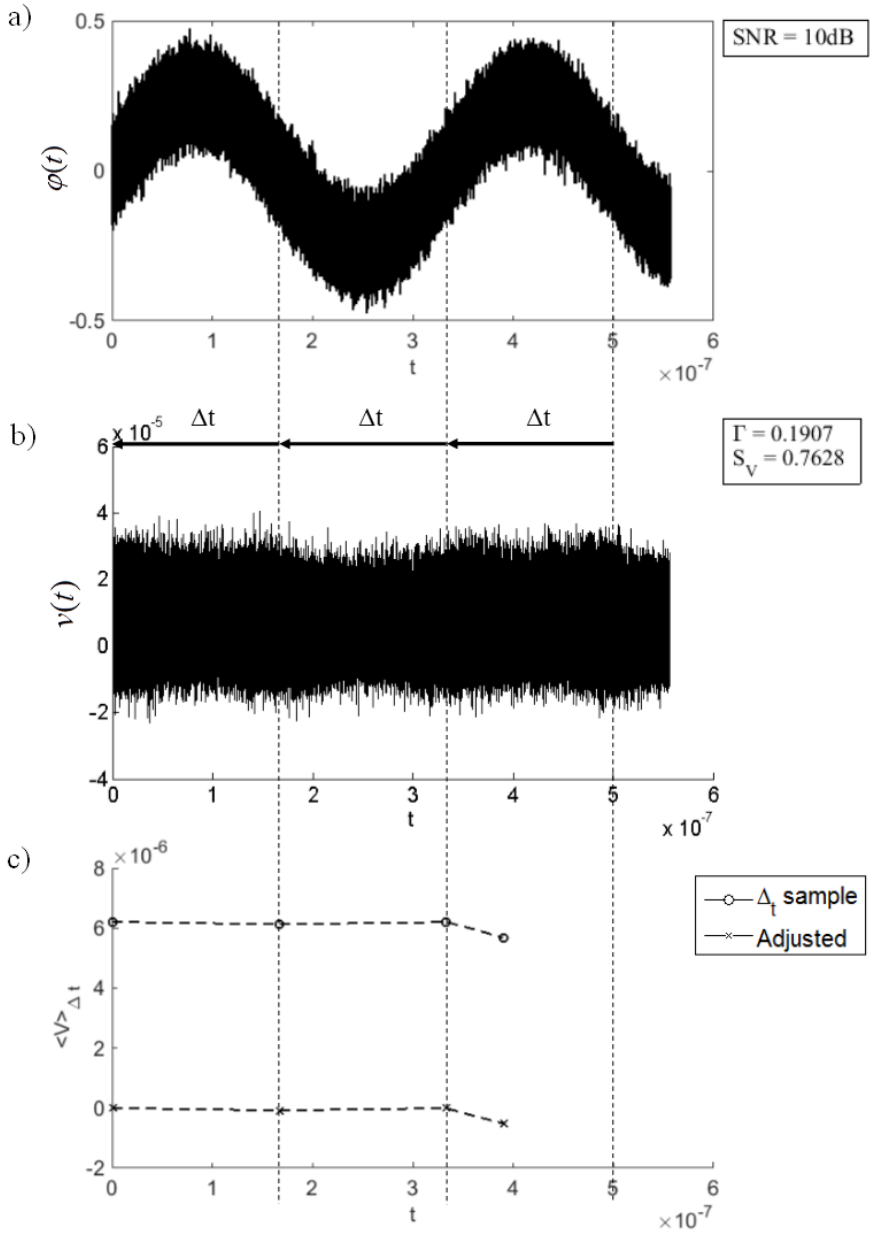

Figure 4.19: (a) Applied magnetic flux signal with $f = 3$ MHz. $|\varphi| = 0.25\phi_0$, and 10dB additional noise. (b) DC SQUID instantaneous voltage $v(t)$ with no increase in amplitude resulting from the additional noise. (c) Voltage samples with $6.1\mu V$ bias produced with a fast time-average of $v(t)$ for a time interval $\Delta t = 0.167\mu$S. $6.1\mu V$ bias is removed to shift the voltage samples to zero, allowing for an accurate sample representation for the 3 MHz applied magnetic flux signal.

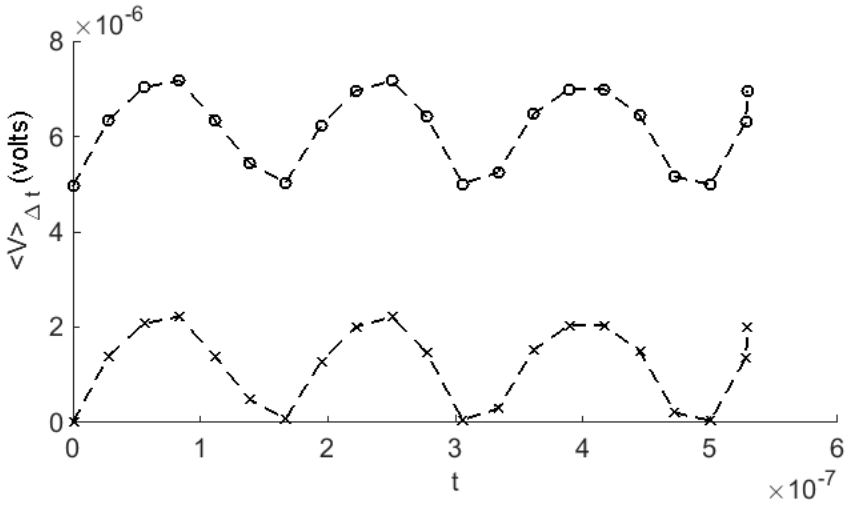

Figure 4.20: Voltage samples produced with a fast time-average of $v(t)$ for a time interval Δt = 27.8nS, producing 12 voltage samples per cycle. A bias offset of $6.1\mu V$ is removed to shift the voltage samples to zero, allow for an accurate sample representation of the 3 MHz magnetic flux signal $\varphi(t)$. The peak to peak voltage is $2.2\mu V$.

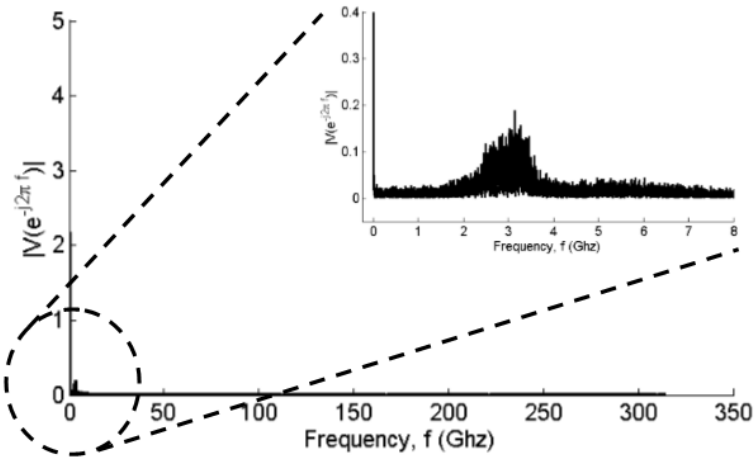

Figure 4.21: Spectral analysis for DC SQUID voltage $v(t)$ produced with thermal and additive noise is performed using the DFT, with a result showing the main spectral content for $v(t)$ lies within the 2-4 GHz band. The spectral content outside the 2-4 GHz band represents the noise floor of the DC SQUID sensor.

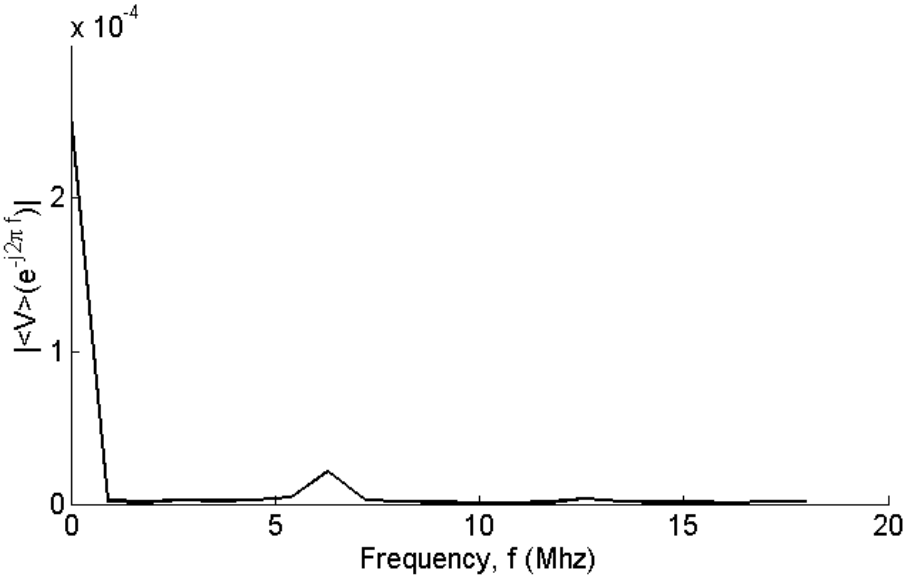

Figure 4.22: Spectral analysis using the DFT for the fast time-averaged voltage samples produced at 12 samples per cycle, with a result showing the main spectral content is centered at 6 MHz.

The remaining frequencies simulated for the HF band show the general characteristic of voltage rectification and the development of the null voltage region at the end of each cycle reconstruction. The additional AWGN does not increase the amplitude of DC SQUID voltage $v(t)$ with the developed voltage remaining very similar to the thermal noise case. A DFT of the DC SQUID voltage shows the majority of the spectral content remains within the 2-4 GHz band with no clear relationship for this particular band present. The main spectral content for the 12 voltage samples per cycle waveforms are centered at twice the frequency of the applied magnetic flux signal, because the voltage rectification causes the resulting waveform period to be reduced by $\frac{1}{2}$, thus effectively increase the frequency by 2. Additional simulation for the selected frequency values 15 MHz and 30 MHz can be found in Appendix B.

The DC SQUID voltage response with thermal noise and additional AWGN over the HF band is shown in Figure 4.23. The peak to peak voltage is computed with fast time averaging at a time interval producing 12 voltage samples per cycle to construct the data

shown in Figure 4.18. The frequencies from the HF band are used to compute the peak to peak voltage response V_{pp} of the DC SQUID. A stable peak to peak voltage trend is shown from the computed V_{pp} data. A resonance not appearing within the HF band is an indication that the DC SQUID has a large bandwidth. The peak to peak voltage response is reduced by half in comparison with the peak to peak voltage response from the noise free simulations, but remains similar to the thermal noise simulations, leading to the conclusion that the addition of excess AWGN noise does not significantly change the DC SQUID voltage response, indicating that the DC SQUID is largely immune to excess environmental noise.

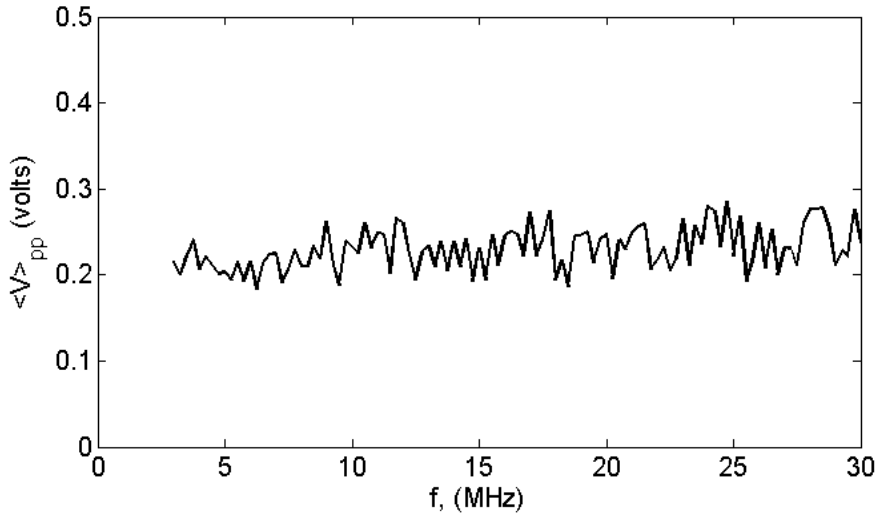

Figure 4.23: Peak to peak voltage response using the 12 voltage sample per cycle for the DC SQUID over the HF band. The peak to peak voltage remains constant over the HF band indicating the device is wide bandwidth.

A null voltage zone develops for the last time-interval of every half cycle. This null voltage develops because of the transition between positive and negative cycles of the input waveform. The DC SQUID bias current was increased to $I_{bias} = 2.1I_C$ in an attempt to eliminate the null voltage zone, since a null voltage zone is observed in the surface plot for

transfer function shown in Figure 3.18. The DC SQUID time-average voltage waveform at 12 samples per cycle with an input signal of $|\varphi| = 0.25\phi_0$ and 3 MHz frequency is shown in Figure 4.24. The null voltage zone is still present, eliminating the bias current as the possible source. The modulation parameter was shown in Chapter 3 to influence the development of the null voltage regions, as shown form Figures 3.14 and 3.18. The modulation parameter is changed from the optimum value $\beta_L = 1$ to $\beta_L = 0.5$ to observe any reduction in the development of the null voltage. The DC SQUID time-average voltage waveform at 12 samples per cycle with an input signal of $|\varphi| = 0.25\phi_0$ and 3 Mhz frequency is shown in Figure 4.25. The null voltage zone is still not reduced, indicating that the modulation parameter does not contribute to the development of this null voltage zone.

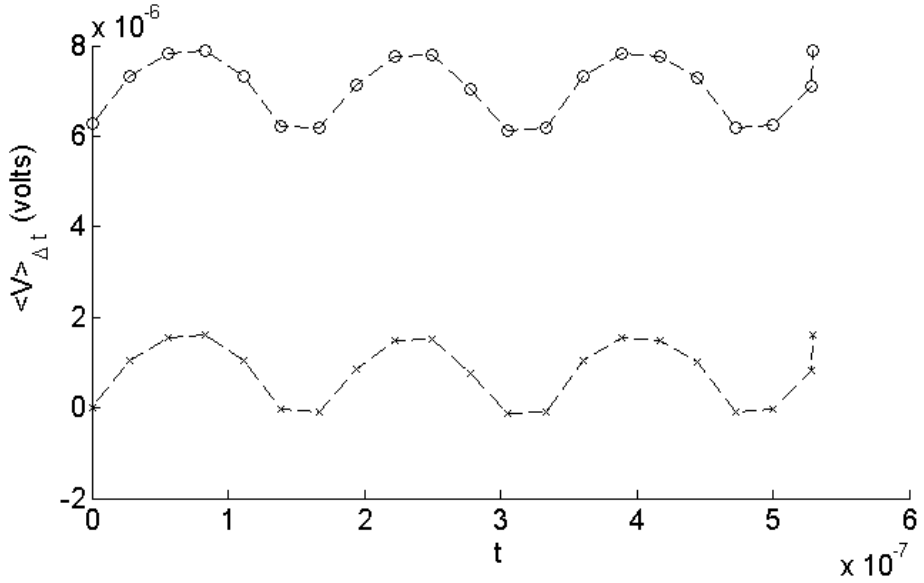

Figure 4.24: DC SQUID bias current increased to $I_{bias} = 2.1I_C$ to observe development of the null voltage zone occurring at the end of each reconstructed half cycle. Null voltage zone remains present, leading to the conclusion that the bias current does not effect null voltage development. The voltage samples are produced using a fast time-average of $v(t)$ at a time interval Δt set to produce 12 voltage samples per cycle for an applied magnetic flux signal $\varphi(t)$ with amplitude $|\varphi| = 0.25\phi_0$ Wb and $f = 3$ MHz.

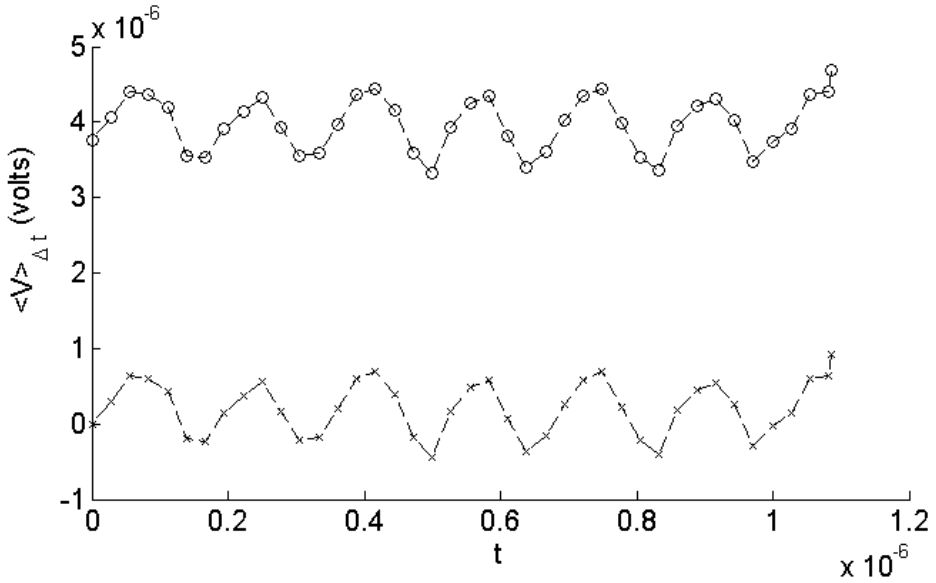

Figure 4.25: Modulation parameter β_L decreased from optimum value ($\beta_L = 1$) to $\beta_L = 0.5$ to observe development of the null voltage zone occurring at the end of each reconstructed half cycle. Null voltage zone remains present, leading to the conclusion that β_L does not effect null voltage development. The voltage samples are produced using a fast time-average of $v(t)$ at a time interval Δt set to produce 12 voltage samples per cycle for an applied magnetic flux signal $\varphi(t)$ with amplitude $|\varphi| = 0.25\phi_0$ Wb and $f = 3$ MHz.

The presence of the null voltage does not change the period of the produced time-average waveform. The addition of thermal noise was shown to reduced the peak to peak voltage value of the time-averaged waveform, and caused a slight expansion of the waveforms curvature. The addition of AWGN to the input signal did not significantly change the resulting time-averaged voltage waveform, compared to the thermal noise only case. The waveform curvature is seen to expand with additional AWGN. The time-averaged voltage values showed very little change because of the time-averaging of white Gaussian noise. AWGN is zero mean, and by performing a time average, the presence of noise is greatly reduced. Figure 4.26 shows a comparison between the noise free, thermal noise, and additional AWGN produced time-average voltage waveforms at 12 sample per cycle for 3 MHz. The top data figure presents the noise free case, the middle data figure shows the thermal noise case, and the bottom data figure shows the 10dB SNR case.

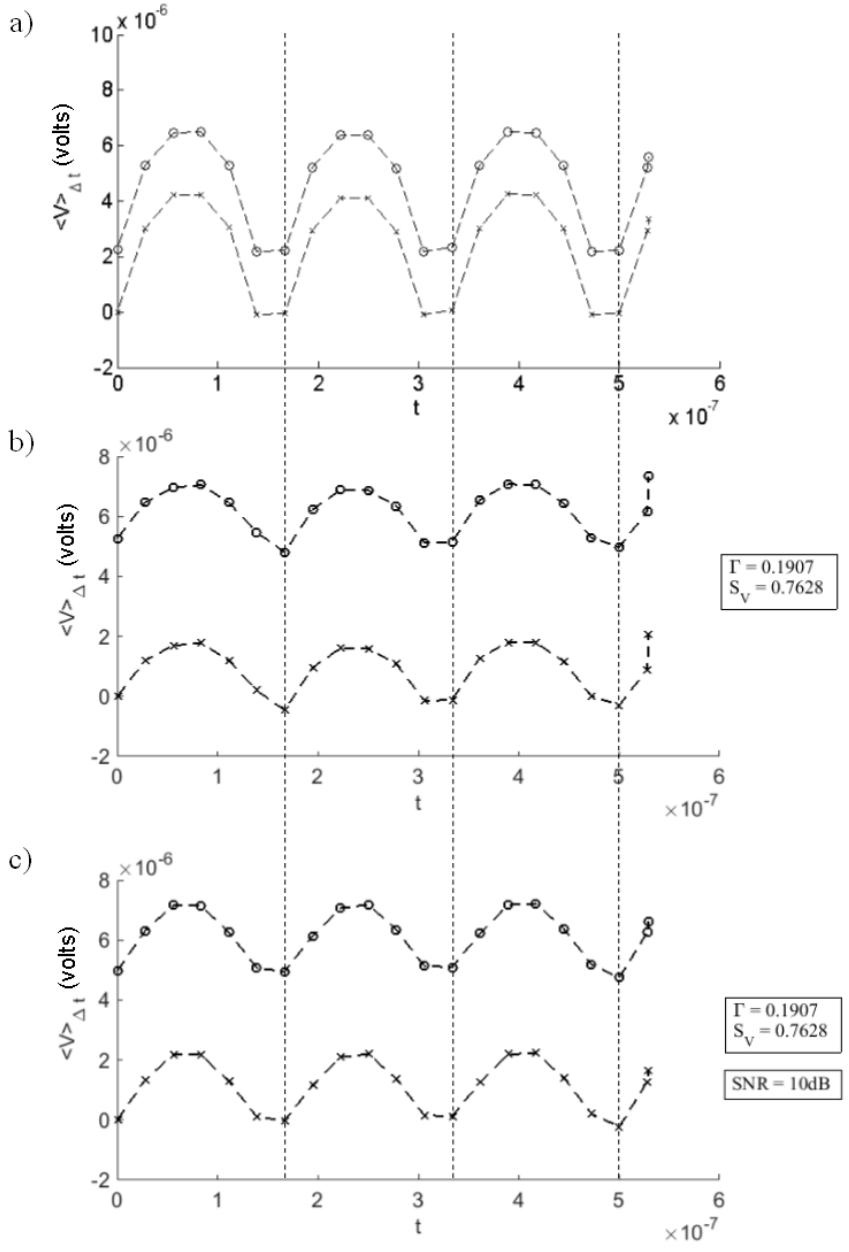

Figure 4.26: Comparison of noise-free, thermal noise, and thermal/additive signal noise fast time-average voltage waveforms using a frequency $f = 3$ MHz, and magnitude $|\varphi| = 0.25\phi_0$ Wb. Fast time-averaging time interval Δt is set to produce 12 voltage samples per cycle.

The DC SQUID's voltage response shows general trends across the three cases, over the frequencies simulated. A fast time-average over a time interval Δt can be used to

produce voltage samples of the applied magnetic flux signal. The Nyquist sampling requirement applies in that the time interval Δt used must be less than half of the period of the applied magnetic flux signal. The voltage waveforms produced using fast time-averaging contain a varying amount of voltage bias, and once removed, provides an accurate, sampled version of the applied magnetic flux signal. However, the DC SQUID and fast time averaging exhibit voltage rectification, as seen by the negative magnetic flux signal cycles appearing as positive voltage values. The voltage rectification response can be predicted by examining the DC SQUID transfer function. The transfer function shows that negative flux values produce positive voltage values as shown in Figure 3.21. Also, a null voltage develops at the end of every reconstructed half cycle. In an attempt to eliminate null voltage development, the bias current was changed, and the modulation parameter β_L was changed from the optimum value, but no elimination or reduction was observed.

4.2.4 DC SQUID Limitations.

Examination of the normalized DC SQUID model equations from Chapter 3 shows that the transfer function is periodic with respect to ϕ_0, and show positive voltage developing for negative applied static flux values. Voltage rectification shown by the DC SQUID and fast time-averaging can be explained with an examination of the transfer function. The fast oscillation frequency ω_C of the DC SQUID is much greater than the frequency of the applied magnetic flux signal, so small fast time average intervals for Δt can be used for sampling the applied magnetic flux signal. In other words, the applied magnetic flux signal over a Δt appears to be slowly varying to the DC SQUID, allowing for a time-average over Δt to be computed.

The usable flux region of the DC SQUID to shown to be 0 to $0.5\phi_0$ as seen in the transfer function from Figure 3.17. Exceeding the usable flux region will cause flux aliasing, explained by the production of a single voltage value for multiple values of applied flux. Figure 4.27 shows the result of exceeding the useable flux region. A magnetic flux

signal with magnitude $|\varphi| = 1\phi_0$ and frequency 3 MHz is applied to the DC SQUID model and the resulting 12 sample per cycle fast time-averaged waveform is shown in Figure 4.27.

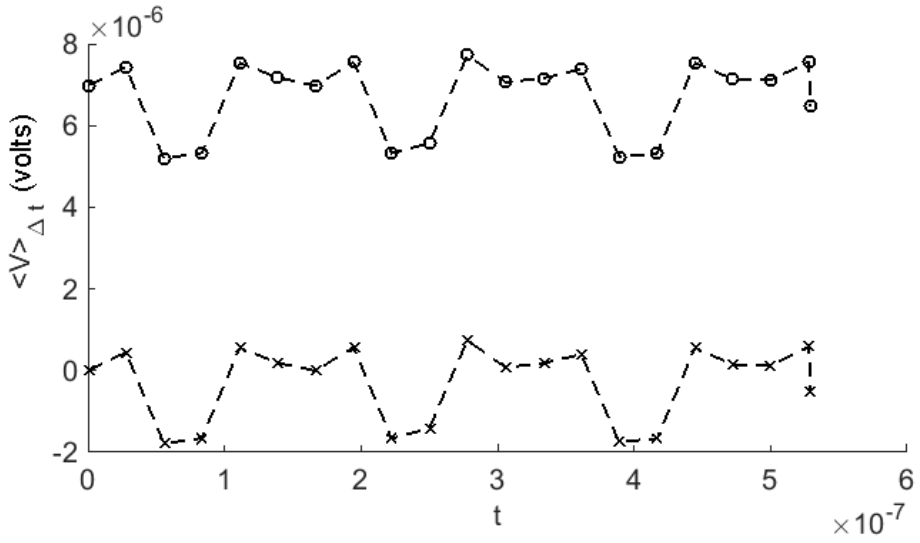

Figure 4.27: Fast time-average voltage samples for applied magnetic flux with magnitude $|\varphi| = 1\phi_0$ and $f = 3$ MHz. A time interval Δt is set to produce 12 voltage samples per cycle. Severe waveform distortion results from exceeded the usable flux range of the DC SQUID, caused by aliasing of flux values.

The fast time-averaged produced waveform shows significant aliasing, appearing as distortion, resulting from exceeding the usable flux range of the DC SQUID.

The usable flux region is shown to be curved seen in Figure 3.17, and leads to distortion, especially at the extreme boundaries 0 and $0.5\phi_0$. Distortion is demonstrated with the application of a raised sinusoidal signal with amplitude $|\varphi| = 0.25\phi_0(1 + sin(ft))$ and frequency $f = 3$ Mhz. The applied magnetic flux signal is shown in Figure 4.28, and Figure 4.29 shows the resulting 12 sample per cycle time averaged waveform.

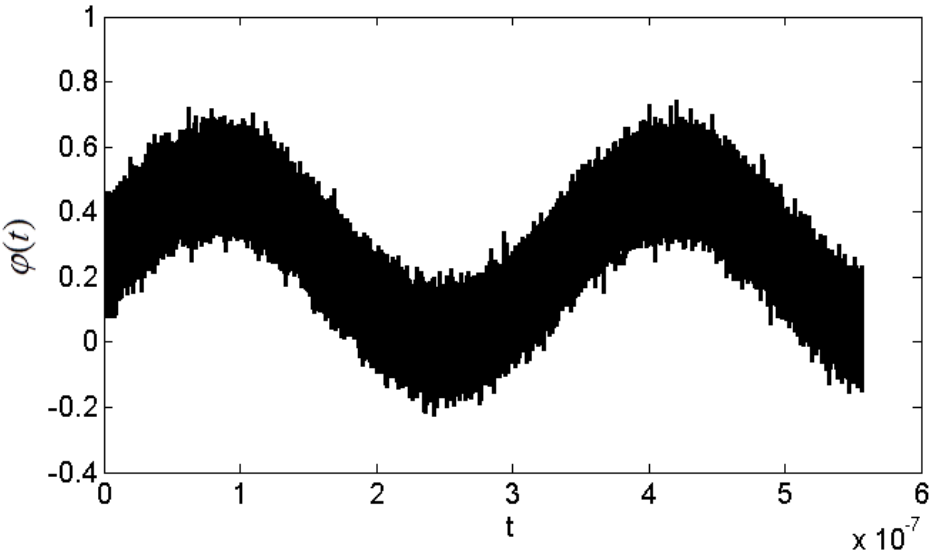

Figure 4.28: Applied raised sinusoidal magnetic flux signal $\varphi = 0.25\phi_0(1 + \sin(ft))$ and $f = 3$ MHz with 10dB of additional noise.

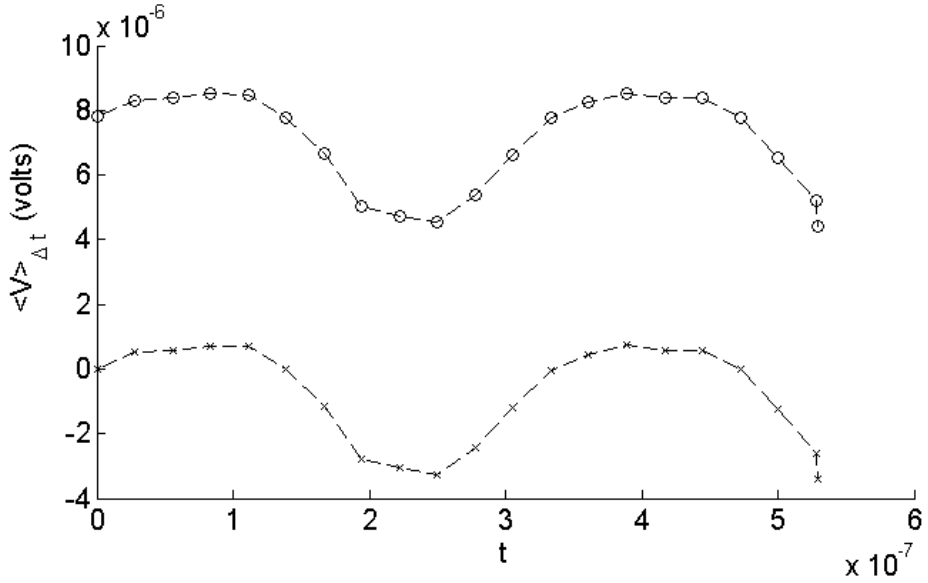

Figure 4.29: Fast time-average voltage samples produced at 12 samples per cycle for a raised sinusoidal applied magnetic flux signal. The applied raised sinusoid exercises the maximum limits of the usable flux range, demonstrating resulting distortion because a curvature seen in the voltage transfer function from Figure 3.17 over the usable flux range.

The fast time-average waveform shows that the upper and lower portions of the sinusoidal signal are distorted because of the slightly curved voltage transfer function.

4.2.5 Application to Direction of Arrival Estimation.

A periodic waveform is produced by the DC SQUID and fast time-averaging, but more importantly, the results show that the phase of the magnetic flux signal is preserved. The preservation of phase is important because this allows the detection of phase differences produced along the face of antenna array. If the phase of the incident signal is not preserved, phase weighting cannot be applied to the voltage signals produced by the individual antenna elements. The DC SQUID sensors can be arranged into an array to produce voltage signals compatible with spatial filtering techniques used for AOA estimation.

4.3 High Frequency Reception

The DC SQUID receives HF energy as shown by circuit model using a time-varying applied magnetic flux signal with frequency f. An output voltage develops in response to the applied magnetic flux signal. A fast time-average is computed over time intervals of Δt to produce voltage samples representing the applied magnetic flux signal. Thermal noise reduces the peak voltage produced by the fast time-averaging. This section presents the HF reception characteristics for the DC SQUID. HF sensitivity is analyzed using the Friis transmission equation and optical responsitivity is used to perfom a comparison with the BDOT sensor. HF EM propagation is considered to be in a free space.

4.3.1 Received Power Sensitivity.

The Friis transmission equation computes the HF reception characteristics between two antennas, relating the power density received to the power transmitted and is given by [10], assuming an isotropic radiation pattern,

$$S = \sqrt{\frac{P_t}{4\pi R^2}} \tag{4.7}$$

where S is the power density (W/m^2) at a range R (m) and P_t is the transmission power (W).

A magnetic flux signal $\varphi = 0.25\phi_0 \sin(ft)$ is shown to have been captured with a single DC SQUID and will be used for range computation. The smallest detectable magnetic flux signal that the DC SQUID can capture contains power equivalent to the noise voltage power, but was not simulated for this research effort. The magnetic flux intensity B is computed using the captured magnetic flux signal φ. The expression for the magnetic flux B passing through a loop is given by,

$$\varphi = |B||A| \cos(\theta) \tag{4.8}$$

where φ is the magnetic flux (Wb), B is the magnitude of the magnetic flux intensity (Wb/m^2), $|A|$ is the surface area of the superconducting loop (m^2), and θ is the angle between B and loop area normal vector. The maximal case $\theta = 0$ is assumed for this computation.

The magnetic flux intensity B is found by dividing the magnetic flux φ by the loop area of the DC SQUID ring, $|B| = \frac{|\varphi|}{|A|}$, but first the DC SQUID loop area must be found.

The DC SQUID loop area is found using the self-inductance equation for a loop, given by [27],

$$L = \frac{\mu_0 N^2 A}{h} \tag{4.9}$$

where L is the inductance (H), μ_0 is the permeability of free space (H/m), N is the number of wire turns, A is the loop area (m^2), and h is the total height of the wire turns (m). Solving for loop area A produces,

$$A = \frac{Lh}{\mu_0 N^2} \tag{4.10}$$

An 1 nH inductance was used for the DC SQUID design, and assuming a loop height of $1\mu m$ and a one-turn loop, the loop area is found to be $A = 0.8nm^2$. The magnetic flux intensity B is now found to be $B = 1.3\mu Wb/m^2$.

The received power density S (W/m^2) relates to magnetic flux intensity B (Wb/m^2) as [9],

$$|S| = \frac{|B|^2}{\mu_0^2}\eta_0 \tag{4.11}$$

where μ_0 is the permeability of free space (H/m) and η_0 is the intrinsic impedance of free space (Ω). Detection range is found by solving for range R with the Friis transmission equation and given as,

$$R_{detect} = \sqrt{\frac{P_t}{4\pi S}} \tag{4.12}$$

where R_{detect} is the detection range, P_t is the transmission power (W), and S is the received power density (W/m^2). A single DC SQUID with an inductance of 1nH provides a detection range of 0.9 meters for a transmission power of 1000 W. This range is not acceptable for an airborne HF DF system, however SQUIDs are typically configured into an array, significantly improving HF sensitivity. Figure 4.30 shows that increasing the loop area allows smaller values of power density to be captured, leading to increased detection ranges as shown in Figure 4.31. Acceptable detection ranges can be achieved by increasing the loop area of the DC SQUID shown in Figure 4.31.

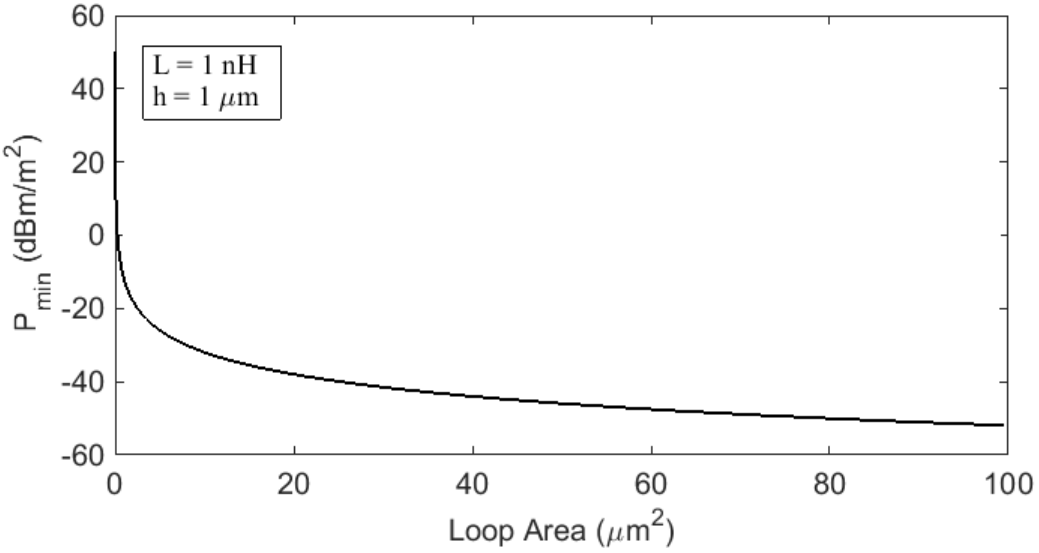

Figure 4.30: DC SQUID HF detection range for a DC SQUID with inductance L=1nH and loop height $h = 1\mu$m for a transmitted power of 1kW. Increasing the DC SQUID loop area allows for reception of small power density values.

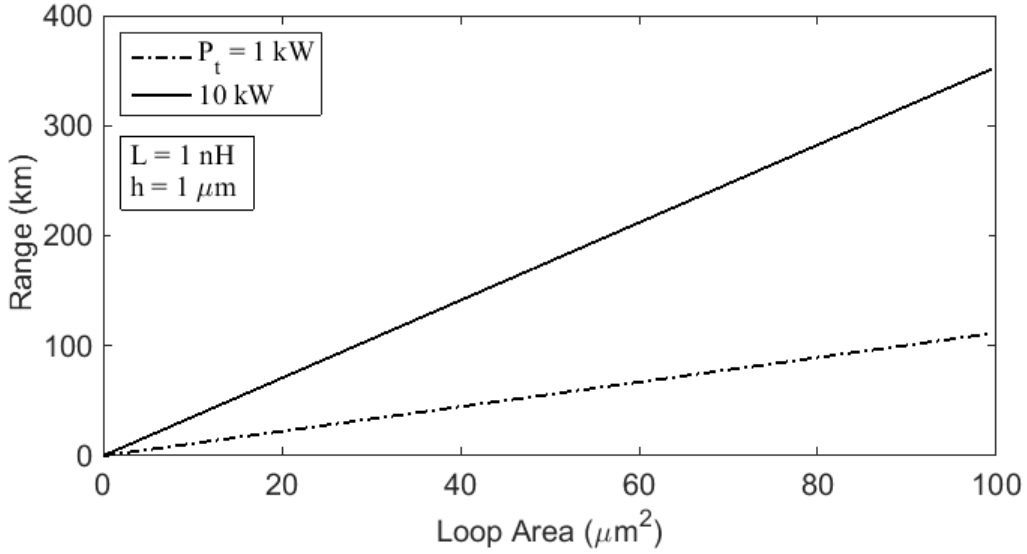

Figure 4.31: HF detection range for a DC SQUID with inductance L=1nH, loop height h=1μm for a transmitted power of 1kW and 10kW. Detection range increases as the loop area is increased, however DC SQUID inductance must be maintained because increasing inductance reduces the energy resolution and voltage response of the DC SQUID.

DC SQUID inductance is proportionally related to loop area, so increasing loop area will increase inductance. DC SQUIDs are designed to minimize inductance, as outlined in Figure 4.1, so that the energy resolution and voltage response are maximized, however there are techniques to avoid increasing inductance. A series array containing DC SQUIDs can be used to increase the capture area without increasing individual DC SQUID inductance [16]. A series array of M DC SQUIDs have been shown to increase the voltage output by M, with a noise increase of only $\sqrt{M}$ [38]. The capture area of individual DC SQUIDs can utilize a flux focusing design [16], by using wide traces for loop construction to force the magnetic flux into the loop, since magnetic flux does not penetrate far into superconductor materials. The flux arriving on the trace is forced inside the loop, therefore increasing the capture area of the loop. The loop capture area can also be increased by using coupled DC SQUIDs [16]. The coupled DC SQUID uses a large loop that is inductively coupled with the DC SQUID loop to increase the capture area.

4.3.2 Sensor Responsitivity.

Responsitivity is a metric used for the characterization of optical detectors [14]. Responsitivity of a detector is given by the general relationship [14],

$$\Re = \frac{\text{output signal}}{\text{input power}} \tag{4.13}$$

with units for responsitivity $\Re$ given by the units for the relationship. Most commonly, the unit for responsitivity is volts per watt [14]. Generally, responsitivity $\Re$ is a function of wavelength for the incident radiation and can be defined as [14],

$$\Re(f) = \frac{V_{RMS}(f)}{P_{REC}(f)} \tag{4.14}$$

where $\Re(f)$ is the responsitivity (V/W), V_{RMS} is the root mean square of the voltage response (V), and P_{REC} is the power received (W). Equation 4.14 is used to compute the responsitivity for the DC SQUID and the BDOT sensor. RMS voltage for the DC SQUID is computed using the 12 sample per cycle waveform at each frequency in the HF band. The

received power for the DC SQUID is computed by multiplying Equation 4.11 with the DC SQUID loop area. RMS voltage for the BDOT sensor is taken from the research conducted by Captain Hardin for the characterization of the BDOT sensor. Capt Hardin computed the power received by the BDOT sensor, and is included in Captain Hardin's dataset. The responsitivity for the DC SQUID and the BDOT sensor are shown in Figure 4.32. The responsitivity of the DC SQUID sensor is shown to be approximately 30,000 times greater than that of the BDOT sensor, providing a better HF detection capability for its size.

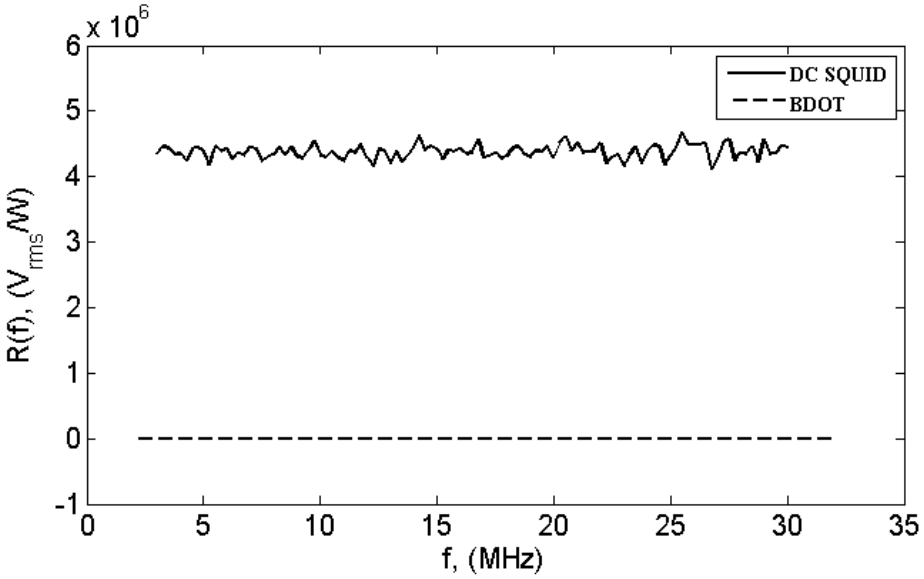

Figure 4.32: Comparison between the BDOT sensor and the DC SQUID sensor responsitivity. DC SQUID sensor shows a responsitivity of 30,000x greater than the BDOT sensor.

V. Conclusion and Future Work

CHAPTER V presents a summary of superconducting quantum interference device research for application to high frequency direction finding.

5.1 SQUIDs and Time-Varying Magnetic Flux Detection

Several design configurations for the SQUID sensors are available but the DC SQUID is the most sensitive detector of magnetic flux. In addition to flux sensitivity, the ultra-low thermal noise properties of the DC SQUID provide optimum conditions for the detection of HF magnetic flux. The RCSJ circuit representation is used to model the DC SQUID electrical operating characteristics with a coupled pair of second order ordinary differential equations and a link equation for the junction phase difference δ_1 and δ_2. A negligible junction capacitance assumption reduces the model equations to a two-dimensional set of first order ODEs with the link equation remaining unaffected. The two-dimensional first order ODEs are numerically solved with the RKF-45 ODE solver to produce a solution for the DC SQUID instantaneous voltage.

The DC SQUID electrical operating characteristic is examined by varying the applied static magnetic flux and bias current to produce the flux to voltage transfer function. The voltage transfer function is seen to be periodic with a period of one flux quantum ϕ_0, with the maximum voltage developing at $0.5\phi_0$. The useable magnetic flux range for the DC SQUID is 0 to $0.5\phi_0$ since the transfer function is periodic with respect to the flux quantum, so intervals of ϕ_0 will produce the same voltage solution.

The condition that produces the largest voltage response in the transfer function is with a bias current equal twice the critical current. A bias current of twice the critical current and the selection of a resistance value are used to maximizing the flux to voltage transfer function for DC SQUID HF examination. DC SQUID thermal noise is introduced using an

additional current source in the RCSJ circuit representation. The addition of thermal noise rounds out the sharp voltage transitions seen for the DC SQUID voltage transfer function and I-V characteristic. Implementation of the RKF-45 ODE solver is verified by recreating data figures from DC SQUID research material, with computed results nearly identical to the data figures in sources [16, 40].

5.2 SQUID High Frequency Reception

DC SQUID instantaneous voltage is computed with an applied time-varying magnetic flux signal of frequency f. The magnitude of the flux signal is simulated using $|\varphi| = 0.25$ and chosen to be within the usable flux range of the DC SQUID. Time-varying applied flux signal frequencies are chosen to span the HF band. A fast time-average is computed using the DC SQUID instantaneous voltage over the time interval Δt to produce the final voltage waveform. Fast time averaging produces a voltage waveform resembling a rectified input signal with half the period of the applied flux signal with a null voltage developing for the end of each cycle reconstruction. This null voltage remains with increasing the bias current and changing the modulation parameter β_L. The periodicity of the fast time averaged waveform allows for conventional spatial filtering techniques to be when used in an antenna array.

5.3 Future Work

The DC SQUID produces voltage waveforms that are periodic, preserving phase, indicating compatibility with AOA estimation techniques, but there are several issues needing to be solved before a usable antenna element is produced. First, the DC SQUID contains a narrow usable magnetic flux range of 0 to $0.5\phi_0$. In addition, the flux range is curved, as shown in the DC SQUID transfer function Figure 3.18. The flux range is easily exceeded, cause flux aliasing to occur. The usable magnetic flux range must be expanded to over several thousand flux quanta ϕ_0 to capture large flux valued signals. The

useful range should have no curvature with a constant slope to be able to provide minimal signal distortion. The SQUIF and BI-SQUID sensors are two devices that expand and provide constant slope transfer functions, however these devices may also exhibit voltage rectification based some of the transfer functions seen for these devices during the course of research. Second, the DC SQUID produces small voltages. The voltage output can be increased by arranging the SQUID sensors into an array to increase the voltage signal, or by using an amplifier to increase the voltage, however this will introduce a greater amount of noise than by using SQUID arrays. SQUID can also be used for ultra low noise amplification and could also be used for this purpose to provide a self contained detection and amplification system [31]. Fourth, the DC SQUID radiation patterns remain unknown. The current EM solvers cannot simulate flux quantization, the Josephson effect, and have only begun to model superconducting phenomena such as the current density within a superconductor.

5.4 Conclusions

The DC SQUID is shown to produce a voltage waveform representative of the applied time-varying magnetic flux signal. The reception range of a single uncoupled DC SQUID is poor, however, DC SQUIDs are often arranged into an array to increase voltage levels and to increase the total flux capture area. HF reception range is significantly increased by increasing the flux capture area, and satisfactory HF reception can be achieved with a capture area as small as . In addition to SQUID arrays, the flux capture area is increased using flux focusing techniques and inductively coupled SQUIDs. The HF reception using SQUID technology is viable for achieving the desired HF reception characteristics of an airborne HF DF system.

Appendix A: Additional Noise-free DC SQUID High Frequency Simulations

Appendix A contains the remaining data figures for the noise-free case with an applied flux signal $\varphi(t)$, the DC SQUID voltage response $v(t)$ for the time-varying applied flux with magnitude $|\varphi| = 0.25\phi_0$ Wb and frequency $f = 15$ and 30 MHz, and the fast time-average computation that produces 12 voltage samples per cycle.

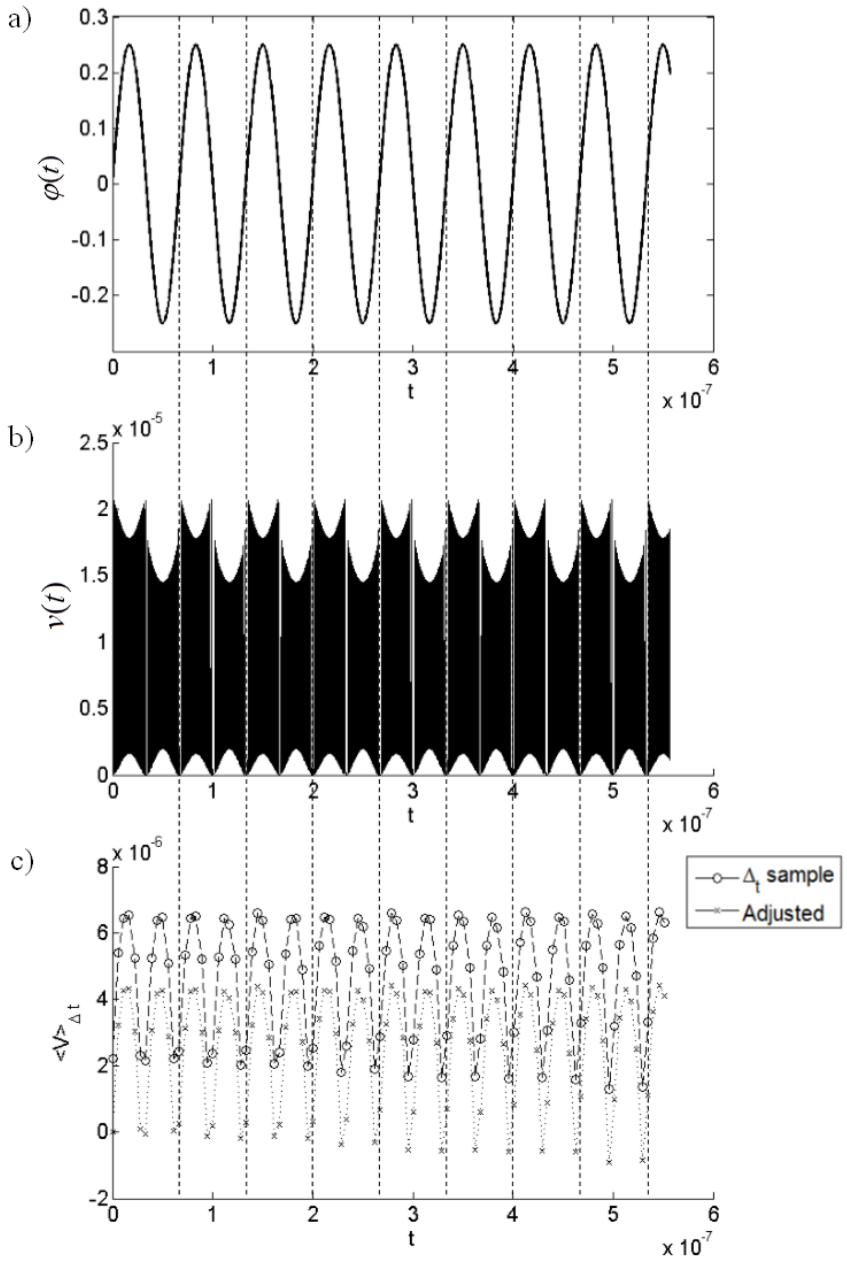

Figure A.1: (a) Applied magnetic flux signal $\varphi(t)$ with $f = 5$ MHz and $|\varphi| = 0.25\phi_0$ Wb. (b) Noise-free DC SQUID instantaneous voltage $v(t)$ develops in response to the applied magnetic flux signal. (c) Voltage samples produced by fast time-averaging $v(t)$ for a time interval Δt set to produce 12 voltage samples per cycle. Voltage bias is removed to shift the voltage samples to zero, allowing for an accurate sample representation for the 15 MHz applied magnetic flux signal $\varphi(t)$.

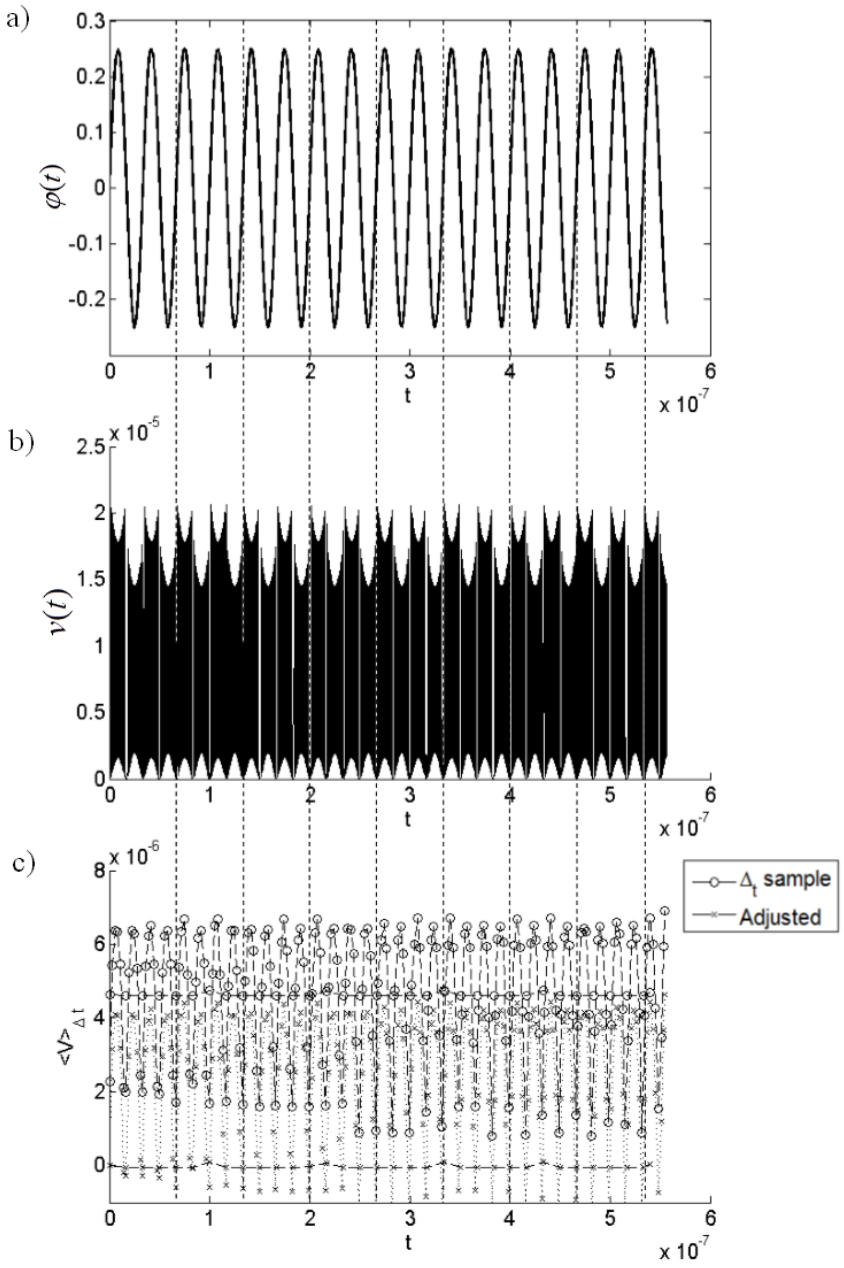

Figure A.2: (a) Applied magnetic flux signal $\varphi(t)$ with $f = 30$ MHz and $|\varphi| = 0.25\phi_0$ Wb. (b) Noise-free DC SQUID instantaneous voltage $v(t)$ develops in response to the applied magnetic flux signal. (c) Voltage samples produced by fast time-averaging $v(t)$ for a time interval Δt set to produce 12 voltage samples per cycle. Voltage bias is removed to shift the voltage samples to zero, allowing for an accurate sample representation for the 30 MHz applied magnetic flux signal $\varphi(t)$.

Appendix B: Additional Noise DC SQUID High Frequency Simulations

Appendix B contains the remaining data figures for the thermal noise case with an applied flux signal $\varphi(t)$, the DC SQUID voltage response $v(t)$ with thermal noise for the time-varying applied flux with magnitude $|\varphi| = 0.25\phi_0$ Wb and frequency set $f = 15$ and 30 MHz, and the fast time-average computation that produces 12 voltage samples per cycle.

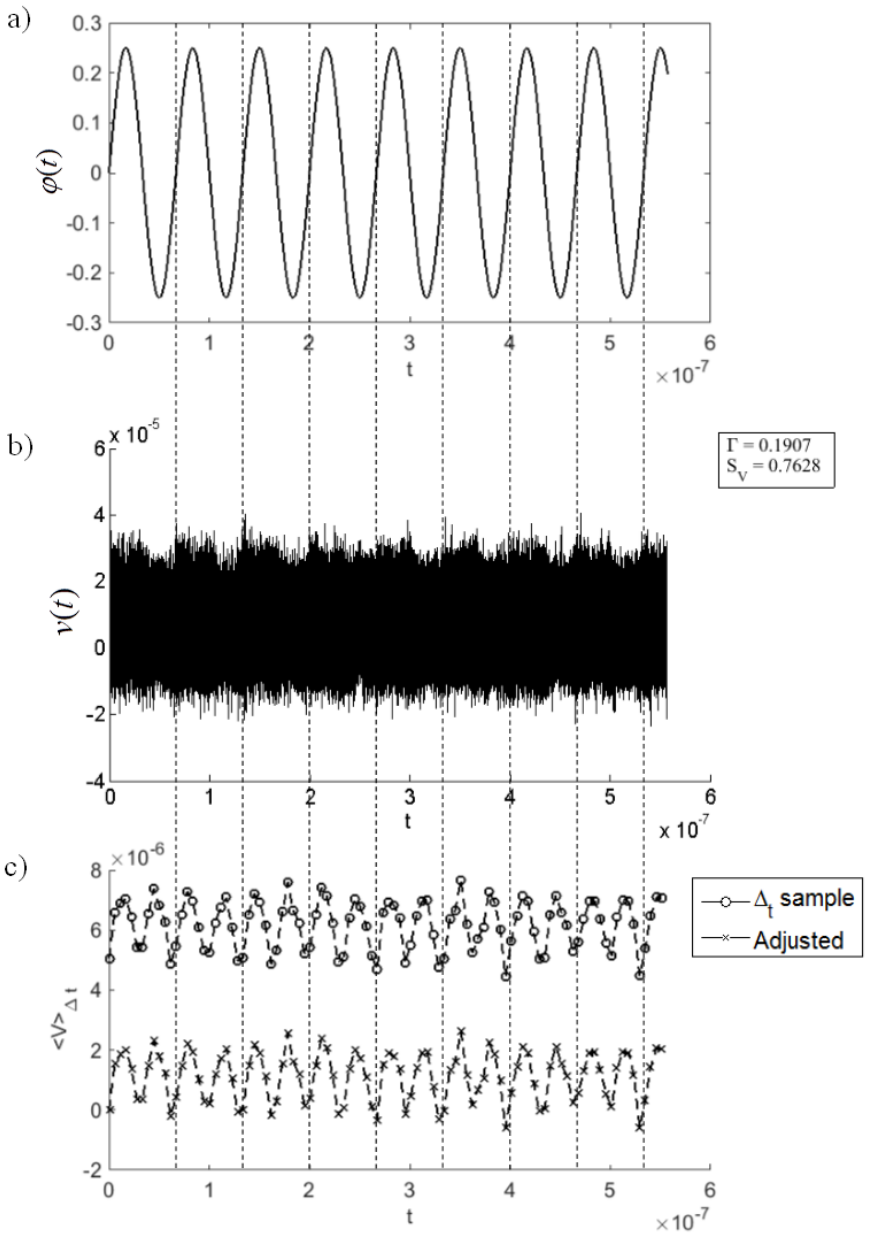

Figure B.1: (a) Applied magnetic flux signal $\varphi(t)$ with $f = 15$ MHz and $|\varphi| = 0.25\phi_0$ Wb. (b) DC SQUID instantaneous voltage $v(t)$ develops in response to the applied magnetic flux signal including thermal noise. (c) Voltage samples produced by fast time-averaging $v(t)$ for a time interval Δt set to produce 12 voltage samples per cycle. Voltage bias is removed to shift the voltage samples to zero, allowing for an accurate sample representation for the 15 MHz applied magnetic flux signal $\varphi(t)$.

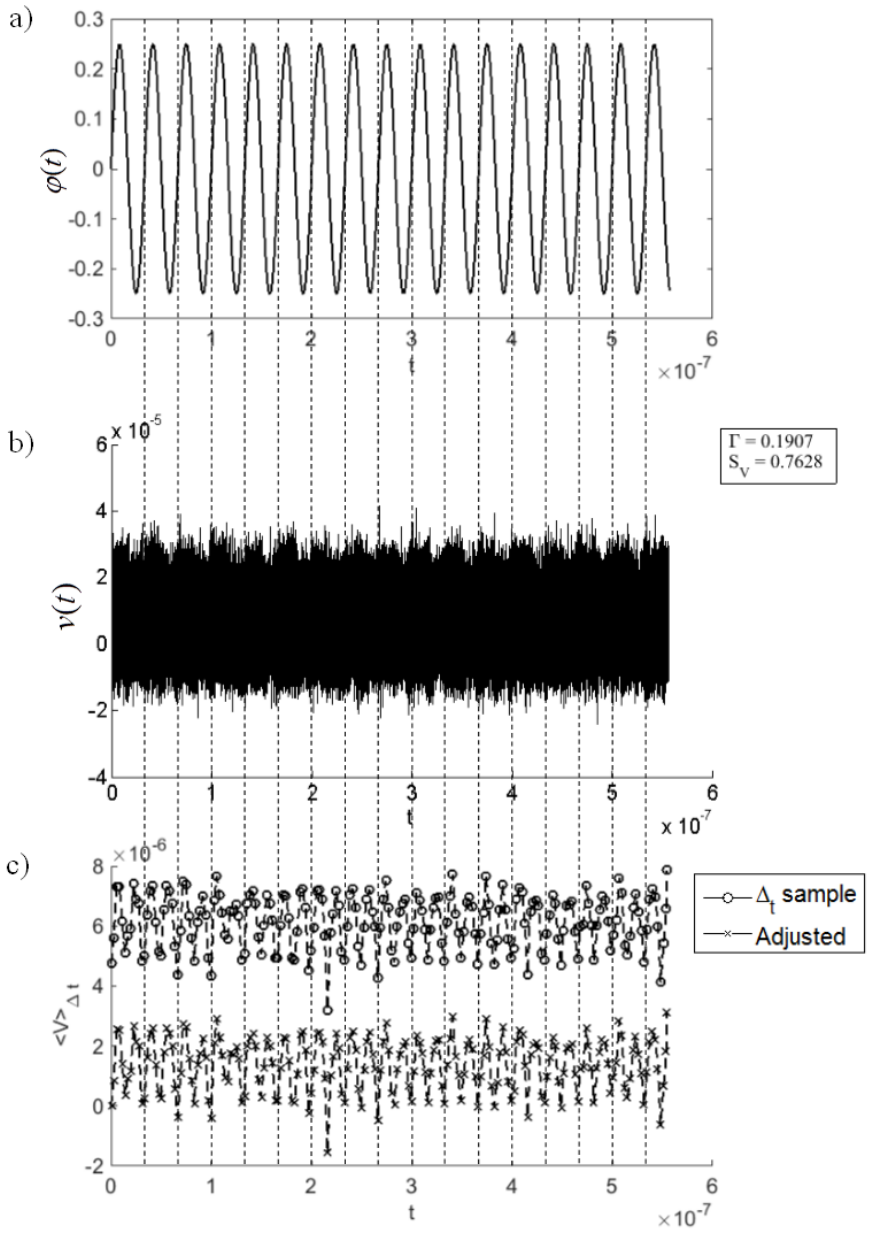

Figure B.2: (a) Applied magnetic flux signal $\varphi(t)$ with $f = 30$ MHz and $|\varphi| = 0.25\phi_0$ Wb. (b) DC SQUID instantaneous voltage $v(t)$ develops in response to the applied magnetic flux signal including thermal noise. (c) Voltage samples produced by fast time-averaging $v(t)$ for a time interval Δt set to produce 12 voltage samples per cycle. Voltage bias is removed to shift the voltage samples to zero, allowing for an accurate sample representation for the 30 MHz applied magnetic flux signal $\varphi(t)$.

Appendix C: Additional Noise DC SQUID High Frequency Simulations

Appendix C contains data figures showing the applied flux signal $\varphi(t)$, the DC SQUID voltage response $v(t)$ for the time-varying applied flux with magnitude $|\varphi| = 0.25\phi_0$ Wb and frequency set $f = 5, 7, 9, 11, 13, 15, 17, 19, 21, 23, 25, 27, 29$ and 30 MHz, and the fast time-average computation that produces 12 voltage samples per cycle.

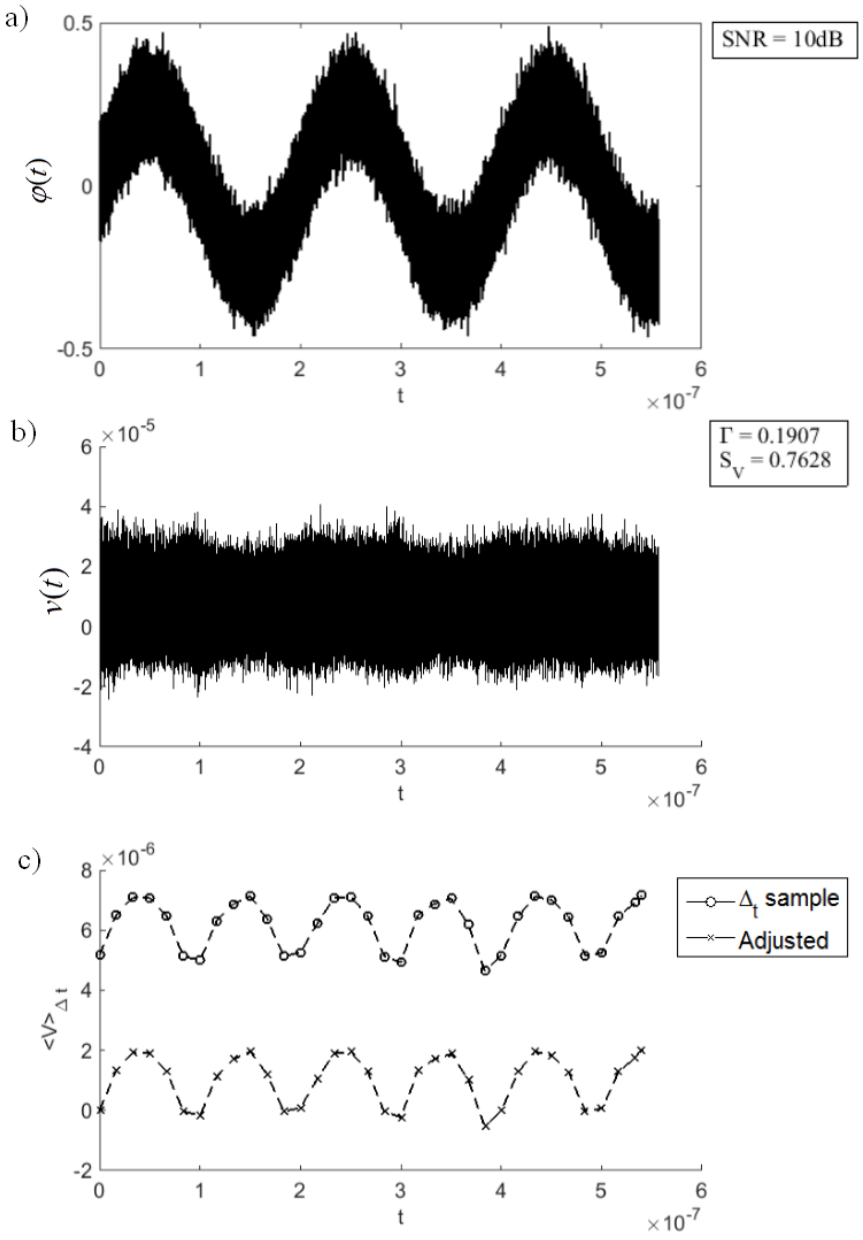

Figure C.1: (a) Applied magnetic flux signal $\varphi(t)$ with $f = 5$ MHz and $|\varphi| = 0.25\phi_0$ Wb with 10dB additional noise. (b) DC SQUID instantaneous voltage $v(t)$ develops in response to the applied magnetic flux signal including thermal noise. (c) Voltage samples produced by fast time-averaging $v(t)$ for a time interval Δt set to produce 12 voltage samples per cycle. Voltage bias is removed to shift the voltage samples to zero, allowing for an accurate sample representation for the 5 MHz applied magnetic flux signal $\varphi(t)$.

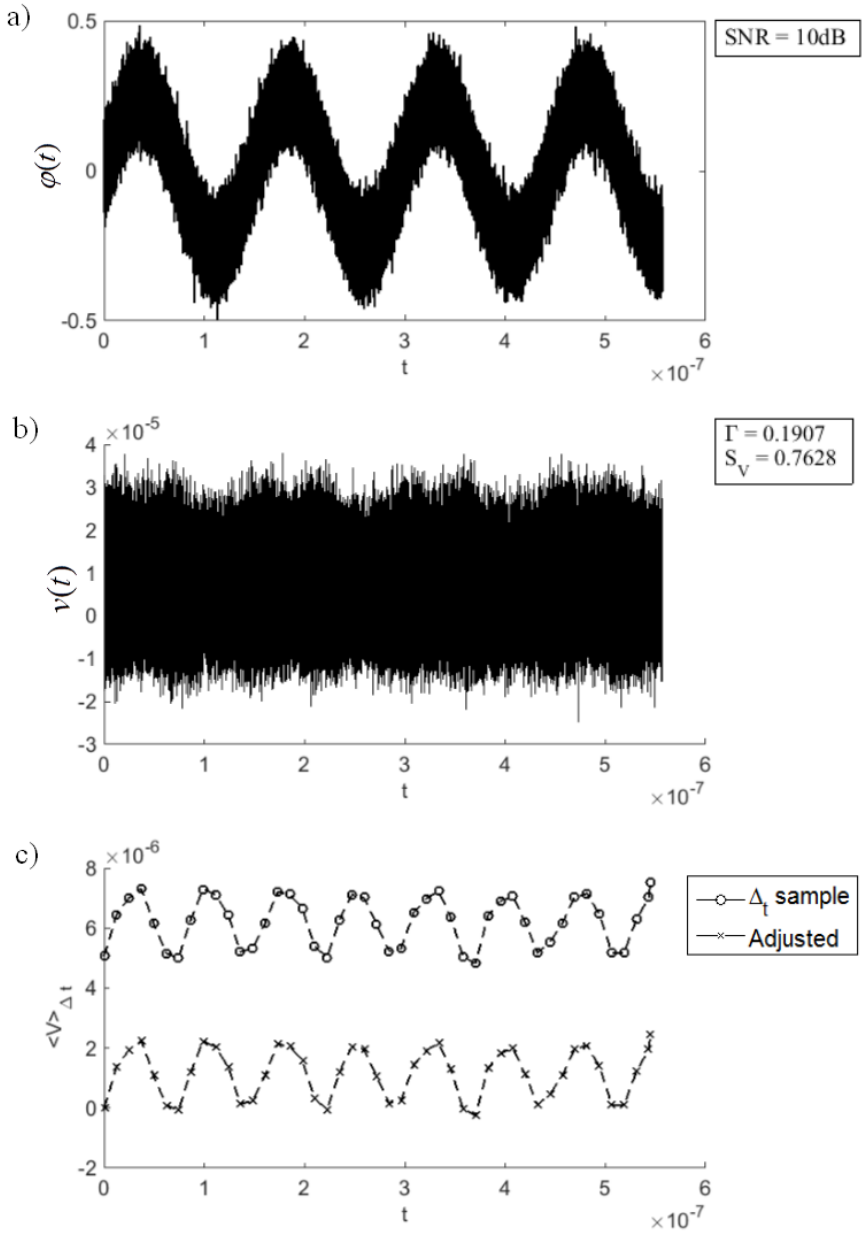

Figure C.2: (a) Applied magnetic flux signal $\varphi(t)$ with $f = 7$ MHz and $|\varphi| = 0.25\phi_0$ Wb with 10dB additional noise. (b) DC SQUID instantaneous voltage $v(t)$ develops in response to the applied magnetic flux signal including thermal noise. (c) Voltage samples produced by fast time-averaging $v(t)$ for a time interval Δt set to produce 12 voltage samples per cycle. Voltage bias is removed to shift the voltage samples to zero, allowing for an accurate sample representation for the 7 MHz applied magnetic flux signal $\varphi(t)$.

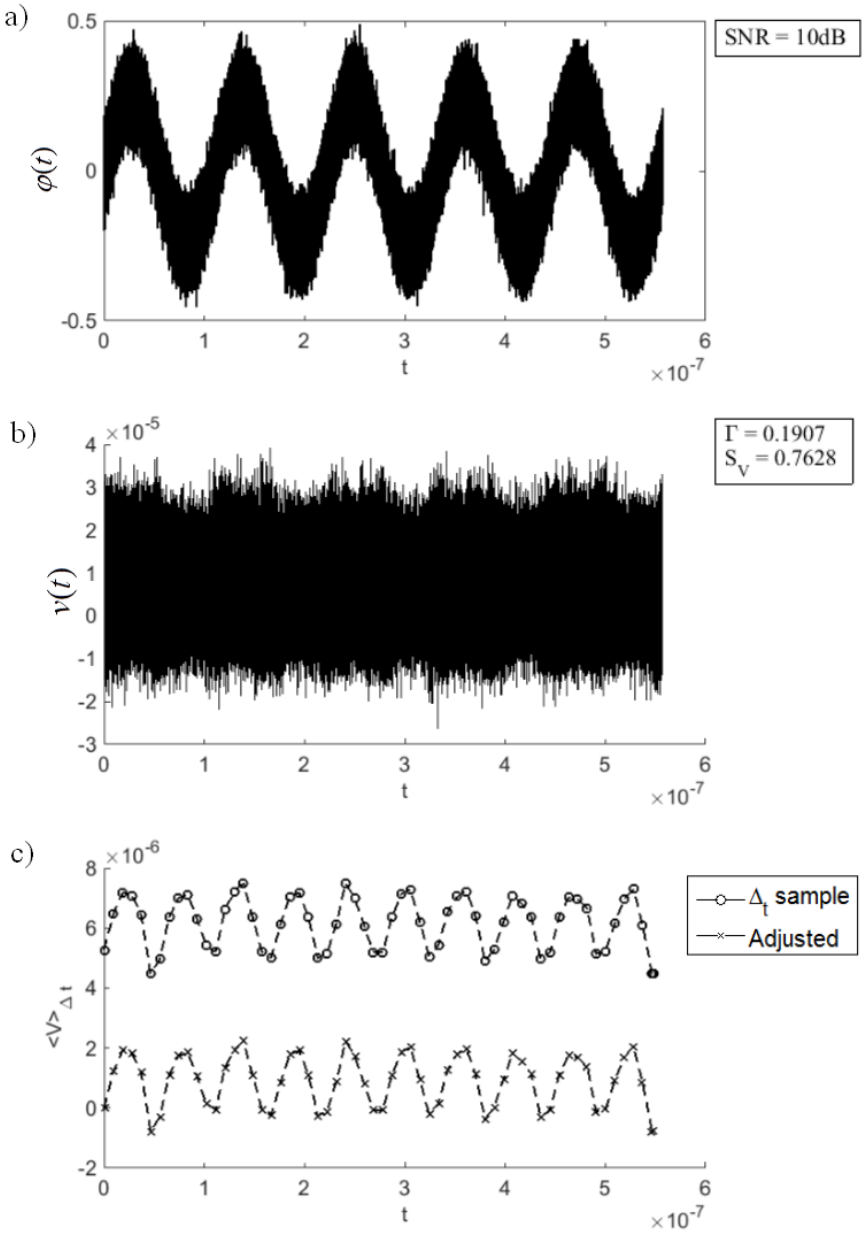

Figure C.3: (a) Applied magnetic flux signal $\varphi(t)$ with $f = 9$ MHz and $|\varphi| = 0.25\phi_0$ Wb with 10dB additional noise. (b) DC SQUID instantaneous voltage $v(t)$ develops in response to the applied magnetic flux signal including thermal noise. (c) Voltage samples produced by fast time-averaging $v(t)$ for a time interval Δt set to produce 12 voltage samples per cycle. Voltage bias is removed to shift the voltage samples to zero, allowing for an accurate sample representation for the 9 MHz applied magnetic flux signal $\varphi(t)$.

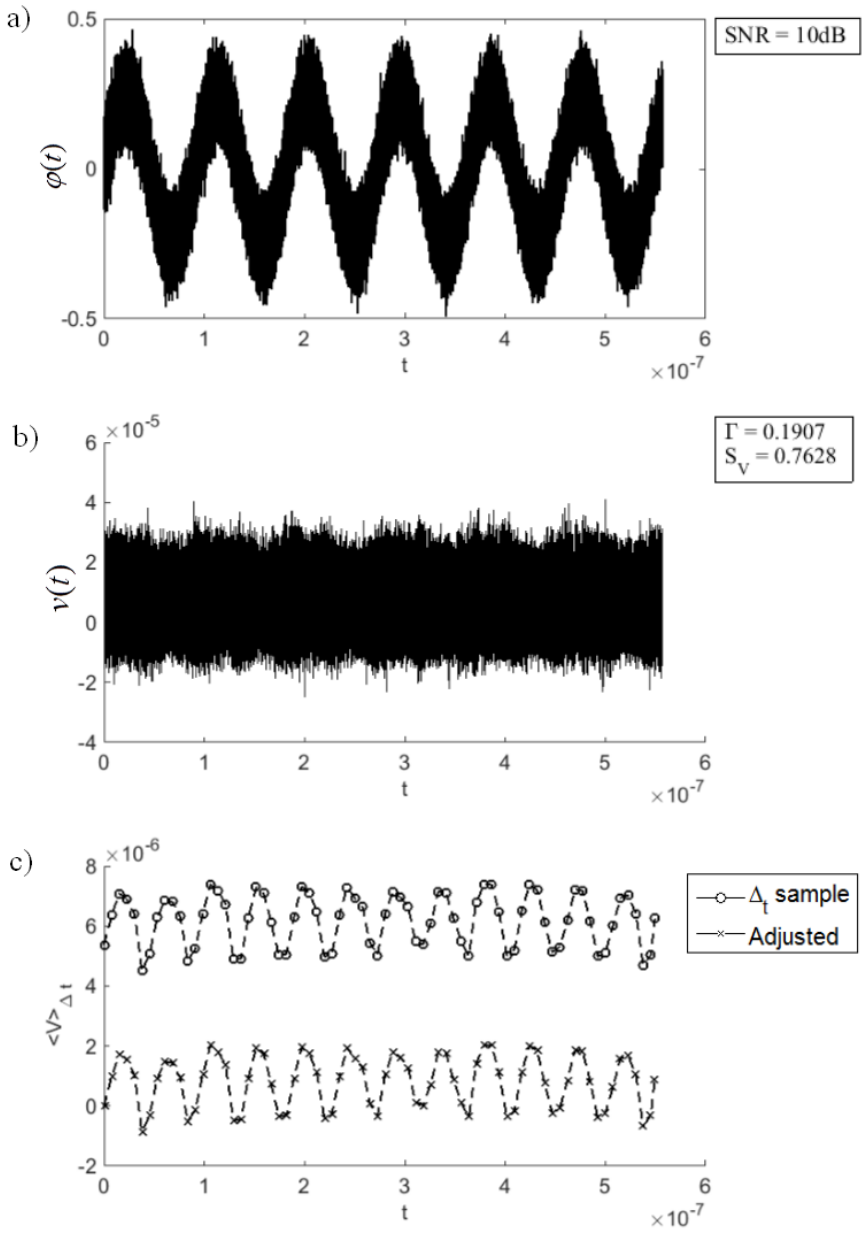

Figure C.4: (a) Applied magnetic flux signal $\varphi(t)$ with $f = 11$ MHz and $|\varphi| = 0.25\phi_0$ Wb with 10dB additional noise. (b) DC SQUID instantaneous voltage $v(t)$ develops in response to the applied magnetic flux signal including thermal noise. (c) Voltage samples produced by fast time-averaging $v(t)$ for a time interval Δt set to produce 12 voltage samples per cycle. Voltage bias is removed to shift the voltage samples to zero, allowing for an accurate sample representation for the 11 MHz applied magnetic flux signal $\varphi(t)$.

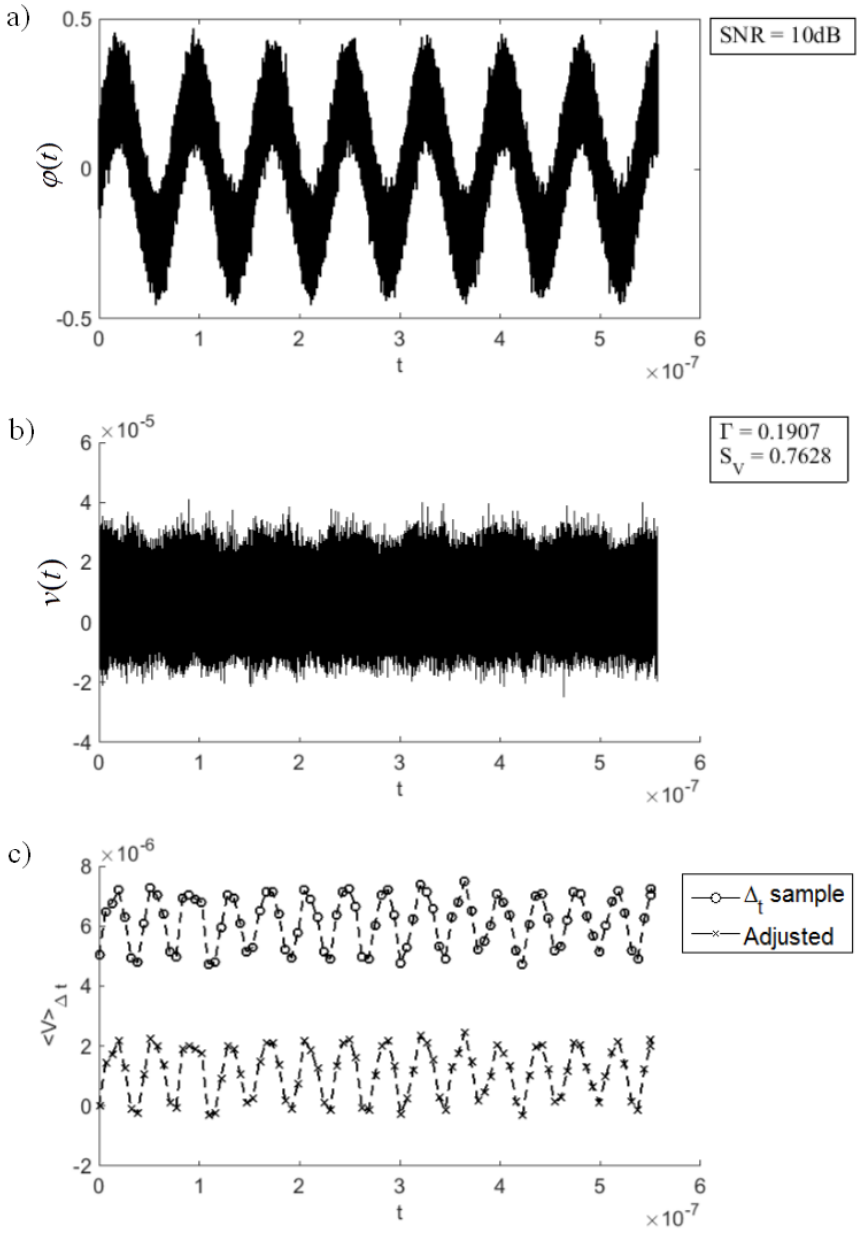

Figure C.5: (a) Applied magnetic flux signal $\varphi(t)$ with $f = 13$ MHz and $|\varphi| = 0.25\phi_0$ Wb with 10dB additional noise. (b) DC SQUID instantaneous voltage $v(t)$ develops in response to the applied magnetic flux signal including thermal noise. (c) Voltage samples produced by fast time-averaging $v(t)$ for a time interval Δt set to produce 12 voltage samples per cycle. Voltage bias is removed to shift the voltage samples to zero, allowing for an accurate sample representation for the 13 MHz applied magnetic flux signal $\varphi(t)$.

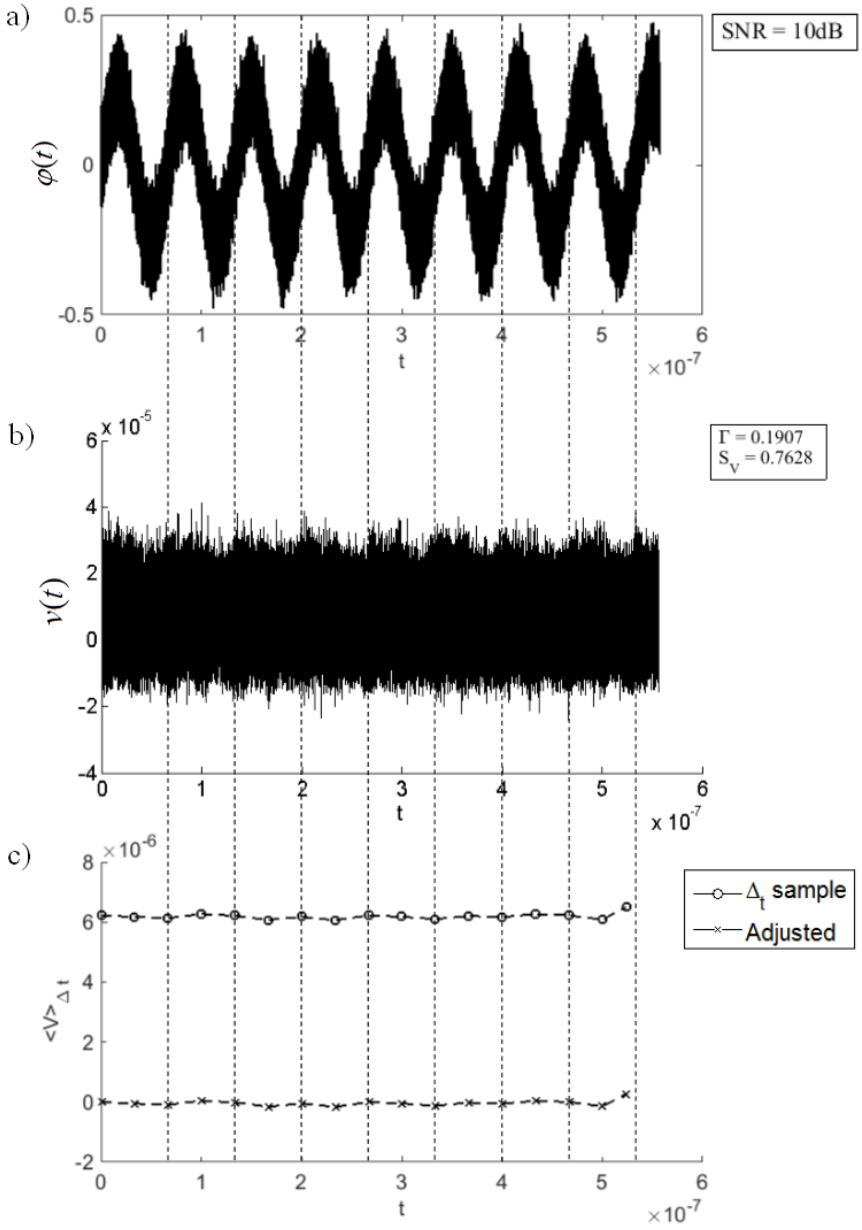

Figure C.6: (a) Applied magnetic flux signal $\varphi(t)$ with $f = 15$ MHz and $|\varphi| = 0.25\phi_0$ Wb with 10dB additional noise. (b) DC SQUID instantaneous voltage $v(t)$ develops in response to the applied magnetic flux signal including thermal noise. (c) Voltage samples produced by fast time-averaging $v(t)$ for a time interval Δt set to produce 12 voltage samples per cycle. Voltage bias is removed to shift the voltage samples to zero, allowing for an accurate sample representation for the 15 MHz applied magnetic flux signal $\varphi(t)$.

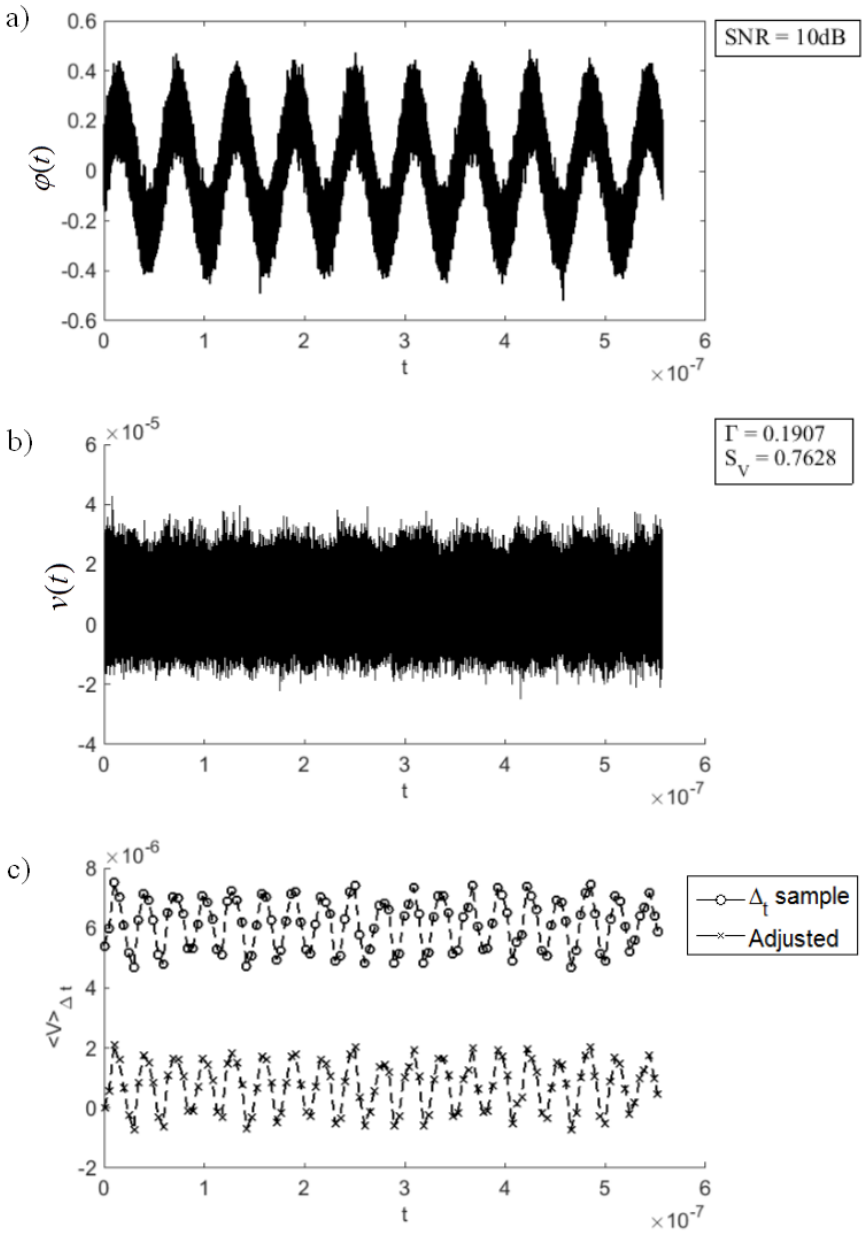

Figure C.7: (a) Applied magnetic flux signal $\varphi(t)$ with $f = 17$ MHz and $|\varphi| = 0.25\phi_0$ Wb with 10dB additional noise. (b) DC SQUID instantaneous voltage $v(t)$ develops in response to the applied magnetic flux signal including thermal noise. (c) Voltage samples produced by fast time-averaging $v(t)$ for a time interval Δt set to produce 12 voltage samples per cycle. Voltage bias is removed to shift the voltage samples to zero, allowing for an accurate sample representation for the 17 MHz applied magnetic flux signal $\varphi(t)$.

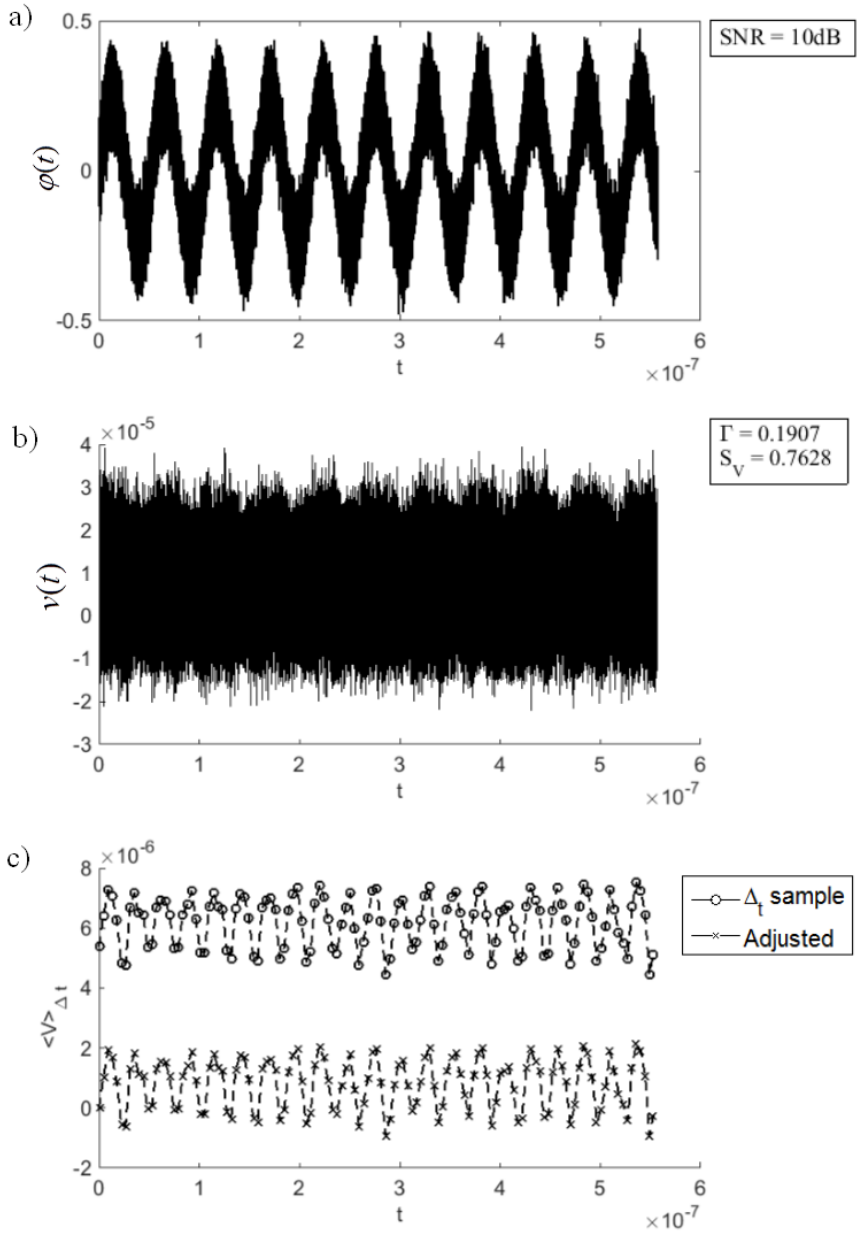

Figure C.8: (a) Applied magnetic flux signal $\varphi(t)$ with $f = 19$ MHz and $|\varphi| = 0.25\phi_0$ Wb with 10dB additional noise. (b) DC SQUID instantaneous voltage $v(t)$ develops in response to the applied magnetic flux signal including thermal noise. (c) Voltage samples produced by fast time-averaging $v(t)$ for a time interval Δt set to produce 12 voltage samples per cycle. Voltage bias is removed to shift the voltage samples to zero, allowing for an accurate sample representation for the 19 MHz applied magnetic flux signal $\varphi(t)$.

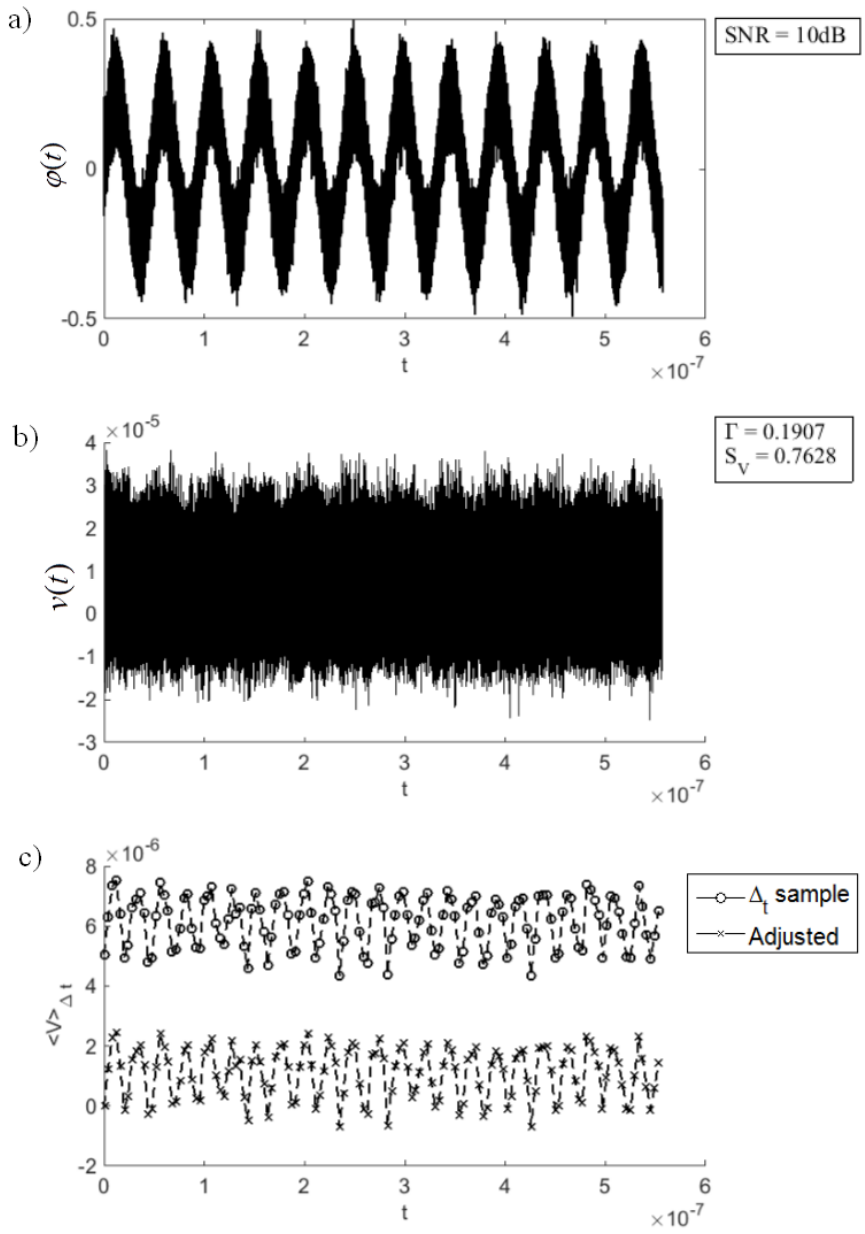

Figure C.9: (a) Applied magnetic flux signal $\varphi(t)$ with $f = 21$ MHz and $|\varphi| = 0.25\phi_0$ Wb with 10dB additional noise. (b) DC SQUID instantaneous voltage $v(t)$ develops in response to the applied magnetic flux signal including thermal noise. (c) Voltage samples produced by fast time-averaging $v(t)$ for a time interval Δt set to produce 12 voltage samples per cycle. Voltage bias is removed to shift the voltage samples to zero, allowing for an accurate sample representation for the 21 MHz applied magnetic flux signal $\varphi(t)$.

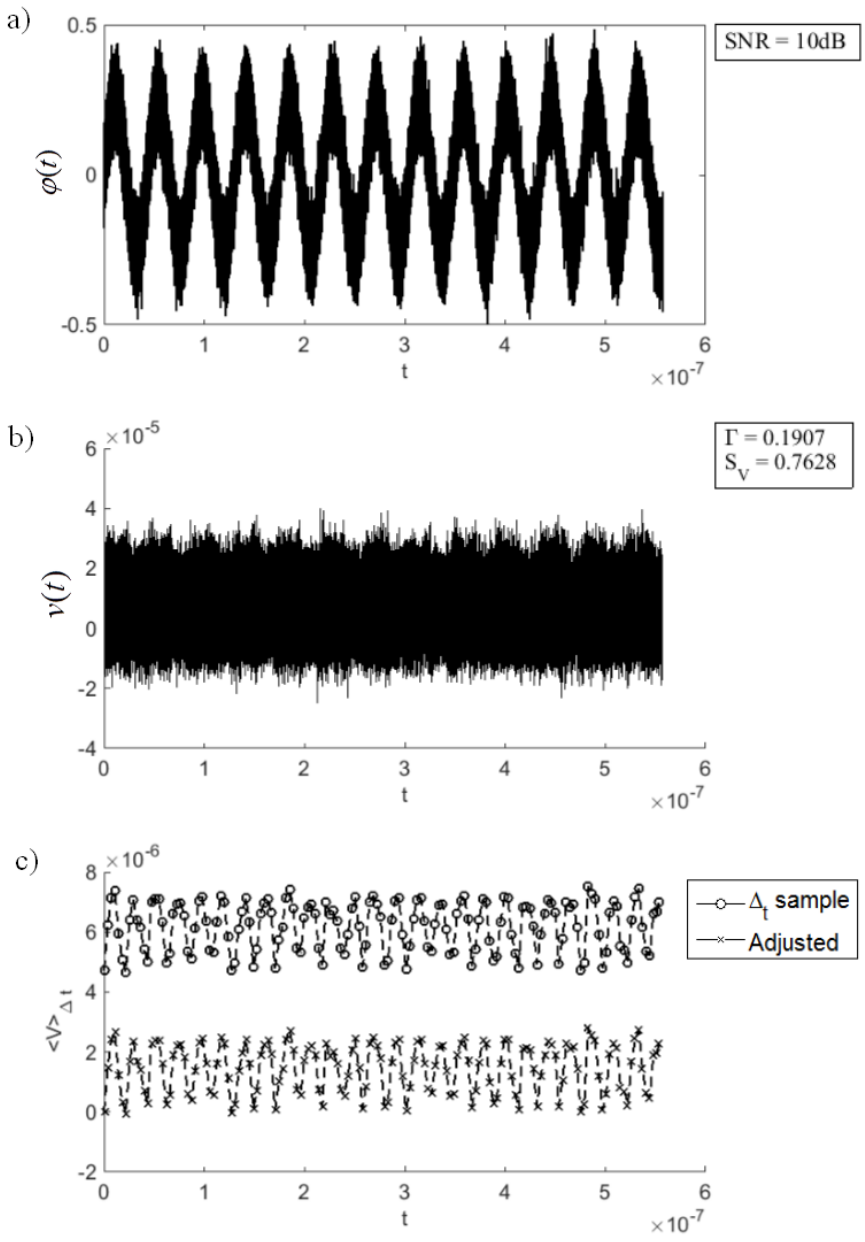

Figure C.10: (a) Applied magnetic flux signal $\varphi(t)$ with $f = 23$ MHz and $|\varphi| = 0.25\phi_0$ Wb with 10dB additional noise. (b) DC SQUID instantaneous voltage $v(t)$ develops in response to the applied magnetic flux signal including thermal noise. (c) Voltage samples produced by fast time-averaging $v(t)$ for a time interval Δt set to produce 12 voltage samples per cycle. Voltage bias is removed to shift the voltage samples to zero, allowing for an accurate sample representation for the 23 MHz applied magnetic flux signal $\varphi(t)$.

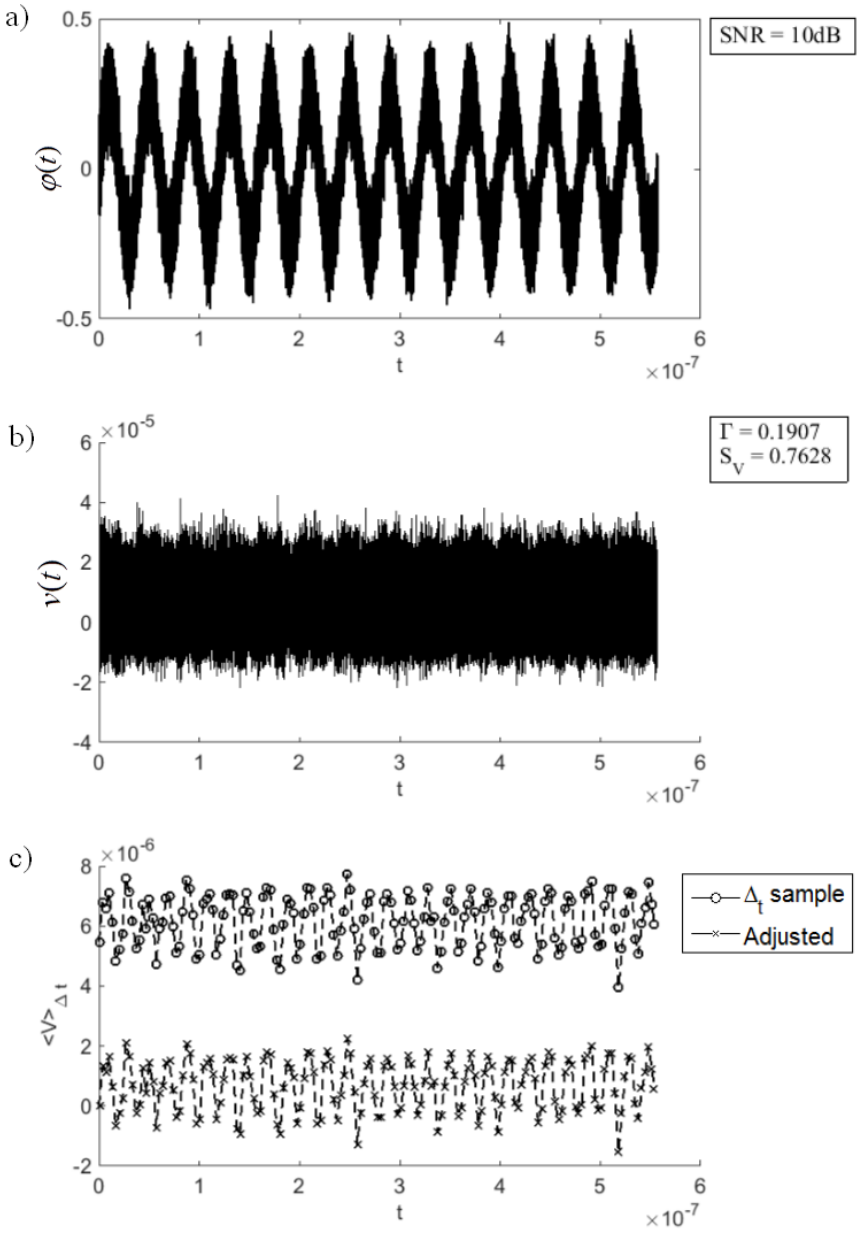

Figure C.11: (a) Applied magnetic flux signal $\varphi(t)$ with $f = 25$ MHz and $|\varphi| = 0.25\phi_0$ Wb with 10dB additional noise. (b) DC SQUID instantaneous voltage $v(t)$ develops in response to the applied magnetic flux signal including thermal noise. (c) Voltage samples produced by fast time-averaging $v(t)$ for a time interval Δt set to produce 12 voltage samples per cycle. Voltage bias is removed to shift the voltage samples to zero, allowing for an accurate sample representation for the 25 MHz applied magnetic flux signal $\varphi(t)$.

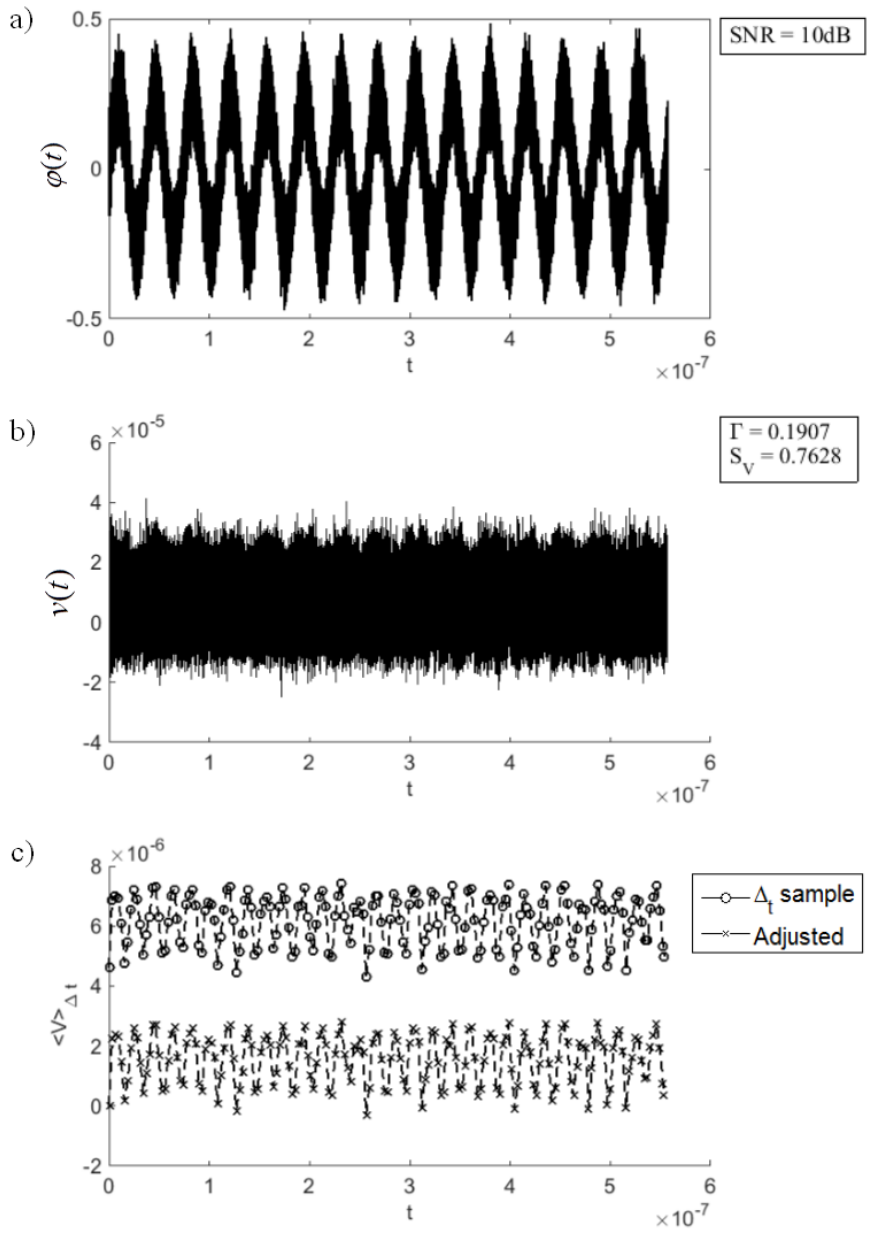

Figure C.12: (a) Applied magnetic flux signal $\varphi(t)$ with $f = 27$ MHz and $|\varphi| = 0.25\phi_0$ Wb with 10dB additional noise. (b) DC SQUID instantaneous voltage $v(t)$ develops in response to the applied magnetic flux signal including thermal noise. (c) Voltage samples produced by fast time-averaging $v(t)$ for a time interval Δt set to produce 12 voltage samples per cycle. Voltage bias is removed to shift the voltage samples to zero, allowing for an accurate sample representation for the 27 MHz applied magnetic flux signal $\varphi(t)$.

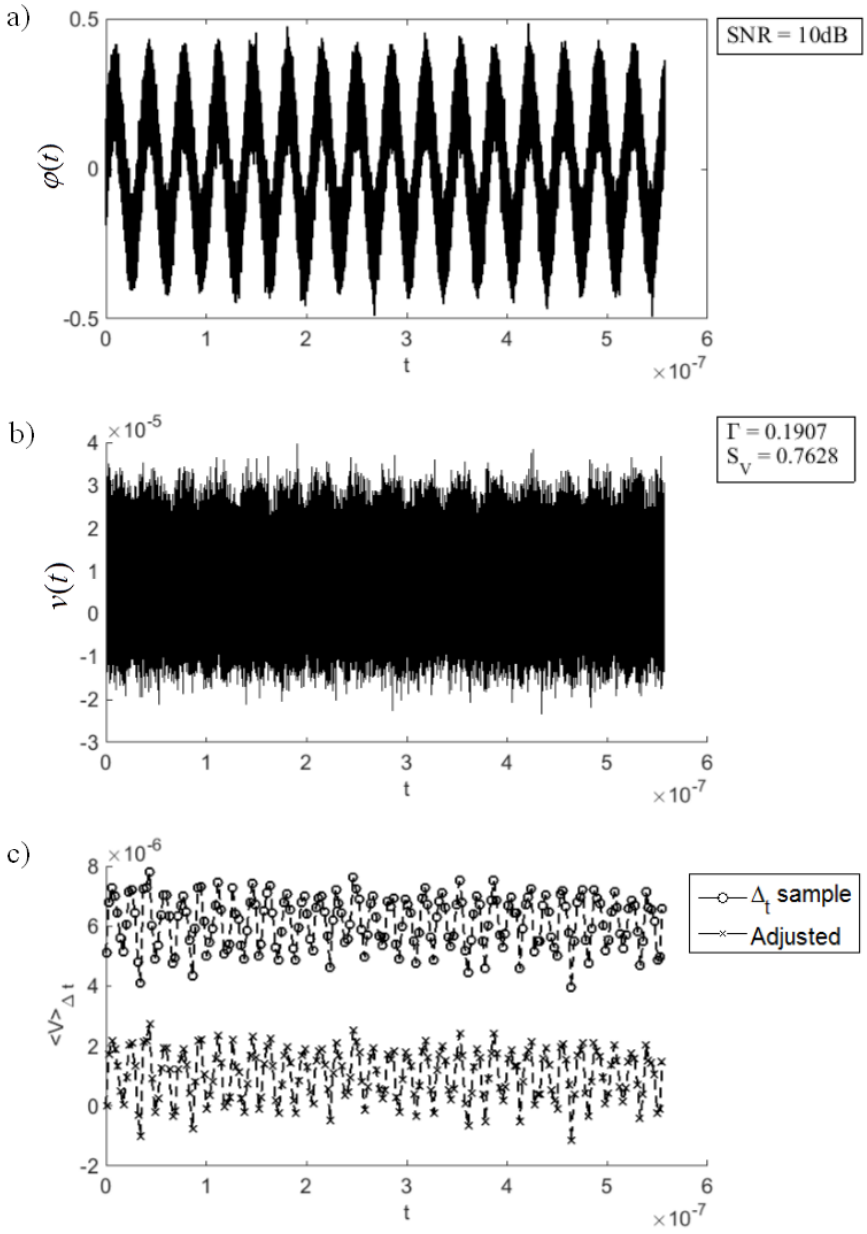

Figure C.13: (a) Applied magnetic flux signal $\varphi(t)$ with $f = 29$ MHz and $|\varphi| = 0.25\phi_0$ Wb with 10dB additional noise. (b) DC SQUID instantaneous voltage $v(t)$ develops in response to the applied magnetic flux signal including thermal noise. (c) Voltage samples produced by fast time-averaging $v(t)$ for a time interval Δt set to produce 12 voltage samples per cycle. Voltage bias is removed to shift the voltage samples to zero, allowing for an accurate sample representation for the 29 MHz applied magnetic flux signal $\varphi(t)$.

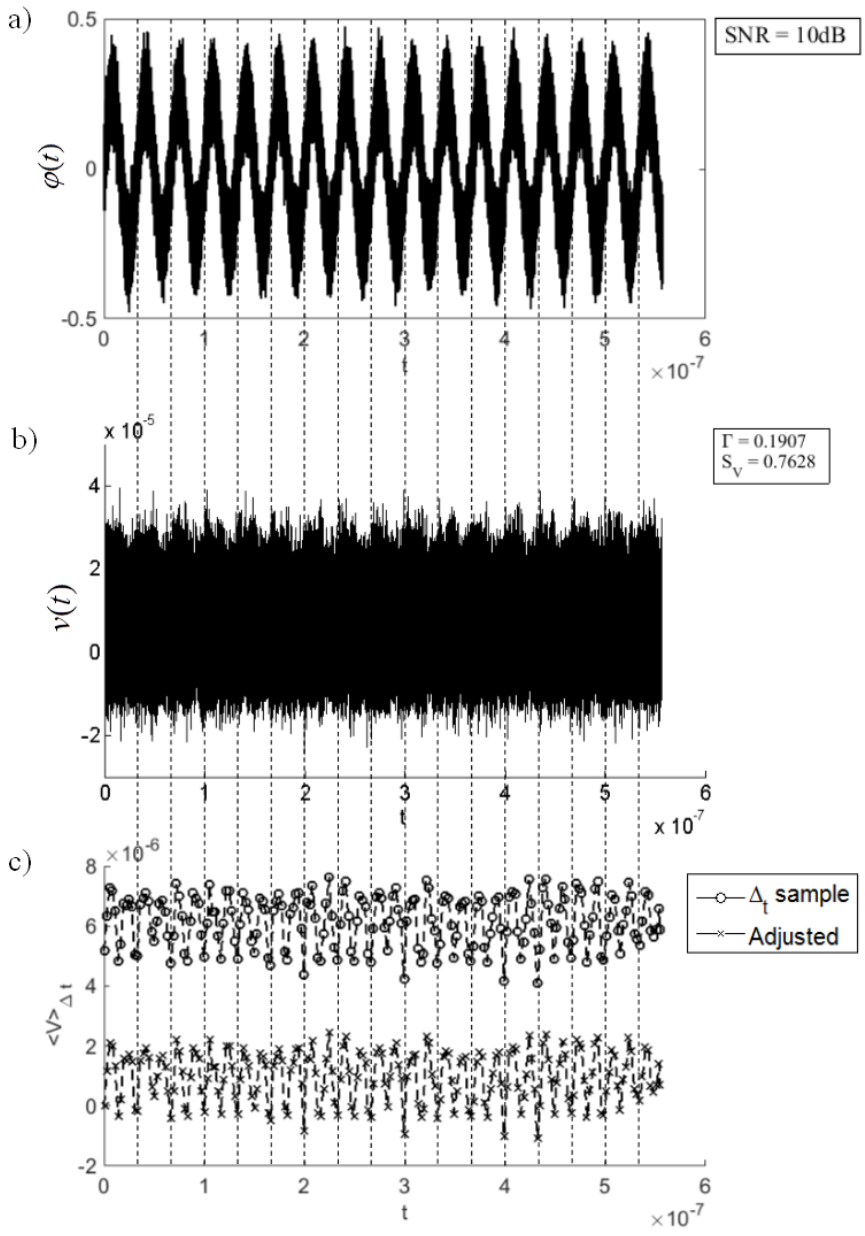

Figure C.14: (a) Applied magnetic flux signal $\varphi(t)$ with $f = 30$ MHz and $|\varphi| = 0.25\phi_0$ Wb with 10dB additional noise. (b) DC SQUID instantaneous voltage $v(t)$ develops in response to the applied magnetic flux signal including thermal noise. (c) Voltage samples produced by fast time-averaging $v(t)$ for a time interval Δt set to produce 12 voltage samples per cycle. Voltage bias is removed to shift the voltage samples to zero, allowing for an accurate sample representation for the 30 MHz applied magnetic flux signal $\varphi(t)$.

Bibliography

[1] "RC-135 V/W Rivet Joint". http://www.af.mil/AboutUs/FactSheets/Display/tabid/224/Article/104608/rc-135vw-rivet-joint.aspx. Accessed: 2014-09-30.

[2] "IEEE Standard Letter Designations for Radar-Frequency Bands". *IEEE Std 521-1984*, 1984.

[3] "Nomenclature of the Frequency and Wavelength Bands used in Telecommunications". *Recommendation ITU-R V.431-7*, 1–3, 2000.

[4] "United States Frequency Allocations". *U.S. Department of Commerce*, August 2011.

[5] "Radio Regulations". *International Telecommunications Union*, 2012.

[6] "FCC Online Table of Frequency Allocations". *Federal Communications Commission Office of Engineering and Technology Policy and Rules Division*, July 2014.

[7] Akers, G. A. *Low band direction finding using an ensemble of structurally integrated antennas*. Master's thesis, Air Force Institute of Technology, March 2000.

[8] Anderson, P. W. and J. M. Rowell. "Probable Observation of the Josephson Superconducting Tunneling Effect". *Phys. Rev. Lett.*, 10:230–232, Mar 1963.

[9] Archer, David. *High Frequency Magnetic Field Direction Finding using MGL-S8A B-DOT Sensors*. Master's thesis, Air Force Institute of Technology, March 2013.

[10] Balanis, Constantine A. *Antenna Theory: Analysis and Design*. John Wiley & Sons, Inc, Hoboken, NJ, third edition, 2005.

[11] Balanis, Constantine A. *Advanced Engineering Electromagnetics*. John Wiley & Sons, Inc, Hoboken, NJ, second edition, 2012.

[12] Blundell, Stephen J. *Superconductivity: A Very Short Introduction*. Oxford University Press, Oxford, United Kingdom, 2009.

[13] Blundell, Stephen J. *Magnetism: A Very Short Introduction*. Oxford University Press, Oxford, United Kingdom, 2012.

[14] Boyd, Robert W. *Radiometry and the Detection of Optical Radiation*. John Wiley & Sons, New York, NY, 1983.

[15] Clarke, John. "Principles and applications of SQUIDs". *Proceedings of the IEEE*, 77(8):1208–1223, Aug 1989.

[16] Clarke, John and Alex Braginski. *The SQUID Handbook Vol. I Fundamentals and Technology of SQUIDs and SQUID systems*. Wiley-VCH, Germany, 2004.

[17] Clarke, John and Alex Braginski. *The SQUID Handbook Vol. II Applications of SQUIDs and SQUID Systems*. Wiley-VCH, Germany, 2004.

[18] Corbin, Clair. *High Frequency Direction Finding using Structurally Integrated Antennas on a Large Airborne Platform*. Master's thesis, Air Force Institute of Technology, March 2011.

[19] Dixon, D. B. *Low-band emitter direction finding and location on UAV-sized platforms*. Master's thesis, Air Force Institute of Technology, March 2001.

[20] E. Johnson, Jr. G. Earle S. Cook, R. Desourdis and J. Ostergaard. *Advanced High-Frequency Radio Communications*. Artech House, Inc., Norwood, MA, 1997.

[21] Griffiths, David J. *Introduction to Quantum Mechanics*. Pearson Education, Inc, Upper Saddle River, NJ, second edition, 2005.

[22] Hansen, R. C. *Electrically Small, Superdirective, and Superconducting Antennas*. John Wiley & Sons, Inc, Hoboken, NJ, 2005.

[23] Hardin, Ryan. *Magnetic Field Generation and B-DOT Sensor Characterization in the High Frequency Band*. Master's thesis, Air Force Institute of Technology, March 2012.

[24] Harrington, Roger F. and J.R. Mautz. "Theory of characteristic modes for conducting bodies". *Antennas and Propagation, IEEE Transactions on*, 19(5):622–628, Sep 1971.

[25] Jaklevic, R. C., John Lambe, A. H. Silver, and J. E. Mercereau. "Quantum interference effects in Josephson tunneling". *Phys. Rev. Lett.*, 12:159–160, Feb 1964.

[26] Josephson, B.D. "Possible new effects in superconductive tunnelling". *Physics Letters*, 1(7):251 – 253, 1962.

[27] K. Lonngren, R. Jost, S. Savov. *Fundamentals of Electromagnetics with MATLAB*. Scitech Publishing, Upper Saddle River, NJ, second edition, 2007.

[28] Kleiner, Reinhold, Dieter Koelle, F. Ludwig, and John Clarke. "Superconducting quantum interference devices: State of the art and applications". *Proceedings of the IEEE*, 92(10):1534–1548, Oct 2004.

[29] Likharev, Konstantin K. *Dynamics of Josephson Junctions and Circuits*. Gordon and Breach Science Publishers, New York, NY, 1986.

[30] M. Richards, J. Scheer and W. Holm. *Principles of Modern Radar: Basic Principles*. SciTech Publishing, Edison, NJ, 201.

[31] Mck, Michael and Robert McDermott. "Radio-frequency amplifiers based on dc SQUIDs". *Superconductor Science and Technology*, 23(9):093001, 2010.

[32] Miller, S. and D. Childers. *Probability and Random Processes*. Academic Press, Waltham, MA, second edition, 2012.

[33] Oppenländer, J., Ch. Häussler, and N. Schopohl. "Non-Φ_0-periodic macroscopic quantum interference in one-dimensional parallel Josephson junction arrays with unconventional grating structure". *Phys. Rev. B*, 63:024511, Dec 2000.

[34] Roediger, P., S.A. Cybart, and R.C. Dynes. "Fabrication of 1rrays of nano-superconducting quantum interference devices using a double-angle processing approach". *Applied Superconductivity, IEEE Transactions on*, 23(3):1100604–1100604, June 2013.

[35] Ryhnen, Tapani, Heikki Sepp, Risto Ilmoniemi, and Jukka Knuutila. "SQUID magnetometers for low-frequency applications". *Journal of Low Temperature Physics*, 76(5-6):287–386, 1989.

[36] Skolnik, Merrill. *Introduction to Radar Systems*. McGraw-Hill, New York, NY, third edition, 2001.

[37] Stanoyevitch, Alexander. *Introduction to Numerical Ordinary and Partial Differential Equations Using MATLAB*. John Wiley & Sons, Inc, Hoboken, NJ, 2005.

[38] Stawiasz, K.G. and M.B. Ketchen. "Noise measurements of series SQUID arrays". *Applied Superconductivity, IEEE Transactions on*, 3(1):1808–1811, March 1993.

[39] Stewart, W. C. "Current voltage characteristics of Josephson junctions". *Applied Physics Letters*, 12(8):277–280, 1968.

[40] Tesche, ClaudiaD. and John Clarke. "dc SQUID: noise and optimization". *Journal of Low Temperature Physics*, 29(3-4):301–331, 1977.

[41] V K Kornev, N V Klenov, I I Soloviev and O A Mukhanov. "Bi-SQUID: a novel linearization method for dc SQUID voltage response". *Superconductor Science and Technology*, 22(11):114011, 2009.

[42] Van, Berrie J. Yan P. Brewer M. Van T, T. and D. Latypow. *Direction Finding Approaches for High Frequency Applications*. Technical report, November 2009.

REPORT DOCUMENTATION PAGE

Form Approved
OMB No. 0704–0188

1. REPORT DATE *(DD–MM–YYYY)*	2. REPORT TYPE	3. DATES COVERED *(From — To)*
26–03–2015	Master's Thesis	Oct 2013–Mar 2015

4. TITLE AND SUBTITLE

Superconducting Quantum Interference Devices for the Detection of Magnetic Flux and Application to Airborne High Frequency Direction Finding

5a. CONTRACT NUMBER

5b. GRANT NUMBER

5c. PROGRAM ELEMENT NUMBER

6. AUTHOR(S)

Abeita, Travis, Captain, USAF

5d. PROJECT NUMBER

N/A

5e. TASK NUMBER

5f. WORK UNIT NUMBER

7. PERFORMING ORGANIZATION NAME(S) AND ADDRESS(ES)

Air Force Institute of Technology
Graduate School of Engineering and Management (AFIT/EN)
2950 Hobson Way
WPAFB, OH 45433-7765

8. PERFORMING ORGANIZATION REPORT NUMBER

AFIT-ENG-MS-15-M-052

9. SPONSORING / MONITORING AGENCY NAME(S) AND ADDRESS(ES)

Air Force Research Laboratory, Radio Frequency Systems Branch
Attn: Dr. Charles Cerny, AFRL/RYMR
2241 Avionics Cir, Area B Bldg 620
Wright-Patterson AFB, OH 45433
(937) 528-8248 (DSN: 798-8248) charles.cerny@wpafb.af.mil

10. SPONSOR/MONITOR'S ACRONYM(S)

AFRL/RYMR

11. SPONSOR/MONITOR'S REPORT NUMBER(S)

12. DISTRIBUTION / AVAILABILITY STATEMENT

DISTRIBUTION STATEMENT A:
APPROVED FOR PUBLIC RELEASE; DISTRIBUTION UNLIMITED

13. SUPPLEMENTARY NOTES

14. ABSTRACT

Electrically small antennas trade reception performance for physical size reduction. The SQUID maximizes the reception performance; still achieving a physically small size leading to satisfying the demanding antenna requirements of an airborne high frequency direction finding antenna system. High frequency electromagnetic reception for a direct current (DC) superconducting quantum interference device (SQUID) is simulated using the resistor-capacitor-shunted-junction (RCSJ) electronic circuit model, producing a set of two-dimensional ordinary differential equations to describe the electrical operating characteristics for the DC SQUID. A time-varying magnetic flux, consisting of frequencies from the HF band, is applied to characterize the voltage response of the DC SQUID. An instantaneous voltage develops across the DC SQUID, although a fast time-average must be computed to produce usable voltage samples. These voltage samples are shown to be representative samples of the applied time-varying signal containing a voltage bias. The waveform produced from these voltage samples is periodic, while preserving the phase of the incident signal. The HF reception characteristics of a single DC SQUID is shown, including an examination for expanding the loop area, simulating a DC SQUID array. Additionally, the DC SQUID is compared to the MGL-S8A BDOT sensor using by optical responsitivity.

15. SUBJECT TERMS

superconducting quantum interference device, SQUID, superconducting antenna, electrically small, direction finding

16. SECURITY CLASSIFICATION OF:			17. LIMITATION OF ABSTRACT	18. NUMBER OF PAGES	19a. NAME OF RESPONSIBLE PERSON
a. REPORT	b. ABSTRACT	c. THIS PAGE			Lt Col Jeremy Stringer (ENG)
U	U	U	UU	138	19b. TELEPHONE NUMBER *(include area code)* (937) 255-3636 x4684 jeremy.stringer@afit.edu